SEARCH FOR QUARK COMPOSITENESS AT $\sqrt{s} = 14$ TeV AT THE LARGE HADRON COLLIDER

THESIS SUBMITTED TO THE UNIVERSITY OF DELHI

FOR THE DEGREE OF

DOCTOR OF PHILOSOPHY

BY

SUSHIL SINGH CHAUHAN

DEPARTMENT OF PHYSICS & ASTROPHYSICS
UNIVERSITY OF DELHI
DELHI 110 007
INDIA

September, 2009

Declaration

It is certified that the work presented in this thesis entitled "**Search for Quark Compositeness at $\sqrt{s} = 14$ TeV at the Large Hadron Collider**" has been carried out at the Department of Physics & Astrophysics of the University of Delhi under the supervision of Prof. Brajesh Chandra Choudhary and Prof. Raghuvir Singh. This thesis deals with search strategy for composite quarks in two different final states at the CMS experiment at Large Hadron Collider at European Organization for Nuclear Research (CERN), Geneva, Switzerland.

This work has been done by the candidate himself and to the best of his knowledge, no part of this work has earlier been submitted for any degree or diploma of this or any other university.

(SUSHIL SINGH CHAUHAN)

Candidate

(Prof. Brajesh Chandra Choudhary)

Supervisor

(Prof. Raghuvir Singh)

Co-Supervisor

Head of the Department

Department of Physics & Astrophysics

University of Delhi

Delhi 110 007

Dedicated To
My Parents

ACKNOWLEDGEMENTS

First and foremost, I express my heartfelt thanks to my thesis advisor and mentor Prof. Brajesh C. Choudhary for his relentless care, undying support, and excellent guidance during the last five precious years of my career. It is indeed a privilege and pleasure to work with him. His systematic approach for physics analysis and excellent command over detector physics has made things easier for me. Apart from physics, I learned from him the importance of being organized and systematic, and having a professional attitude in research. Surely it will be with me in my career as well as in my life.

I would like to take this opportunity to specially thank my co-supervisor Prof. Raghuvir Singh for his encouragement and prompt help during my Ph.D. His constant care and support at the right time made it possible for me to reach my goals.

I express my deepest regards to Prof. Debajoyti Choudhury for his constant support and trust in my abilities. His important contribution to this research work is presented in this thesis. Discussing physics topics with him always made the concepts clear to me and made me less ignorant about my work. I am really looking forward to work with him in future too.

I express my sincere thanks to Dr. Satyaki Bhattacharya for his constant support during my Ph.D, and his contribution to this research work. His deep insight of physics and desire to search for new ideas will always be a source of encouragement. His down-to-earth approach and immense patience has always been a source of inspiration for me.

I am thankful to Prof. R. K. Shivpuri for my first introduction to high energy physics. His faith and encouragement in me to join the exciting field of high energy physics during my M.Sc days led me to this work. I will always remember his advice about research on my first day as a research scholar in this university.

I am also thankful to Maria Spiropulu (California Institute of Technology) and Albert De Roeck (CERN) for showing their interest in this work, their encouragement and support in making it possible for this work to appear as CMS documents.

I am obliged to Prof. D. S. Kulshreshtha (Head, Department of Physics & Astrophysics) for providing all the necessary facilities in the department.

Many thanks to my senior colleagues in the EHEP group at Delhi University consisting of Ashutosh Bhardwaj, Kirti Ranjan, Namrata Bhardwaj, Sudeep Chatterji, Ajay Srivastava, Ashish Kumar, Manoj Kumar Jha, and Md. Naimuddin. This work would not have been accomplished without having open and friendly working environment in

the lab. I would like to specially thank Kirti Ranjan and Ashish Kumar for their valuable suggestions in the time of need. It has been a pleasure to discuss with them on many diverse issues including physics during the tea breaks. I am also thankful to my old friend Ashok who has recently joined our group, for his company in the last year of my Ph.D. I would also like to thank my colleagues Shilpee Arora, Pooja Gupta, Abhinav Dubey, Sudha Ahuja, Sandhya Jain, Shilpi Jain, Pooja Saxena, Arun Saini, Ruchika Nayyar, and Bajarang Sutar for the various discussions and queries on physics problems. It enhanced my knowledge. I really enjoyed their company in lab during my Ph.D.

I express my deep gratitude to Mr. P. C. Gupta and Mr. G. D. Sharma for their continuous encouragement and support. I am also thankful to Yunus, Ravikant and Rakesh for their continuous assistance.

I would like to thank my friends Ranjit, Manish, Sukanto, Partha, Sunil, Sanil, Dharmender, Jaswant, Gopesh, Harish, and Ajay for their help, support, and encouragement. I consider myself lucky to have such caring friends.

I would like to thank the Department of Science and Technology(DST), and Council of Scientific and Industrial Research(CSIR), Govt. of India for the financial support during my Ph.D.

Finally, I want to express my deepest gratitude and appreciation to my parents and family members. They have supported me physically, mentally, and financially. Their affection and unflinching belief and confidence in my decisions have always helped me understand life in a better way.

SUSHIL SINGH CHAUHAN

LIST OF PUBLICATIONS

1. "*Quark excitations through the prism of direct photon plus jet at the LHC*", Satyaki Bhattacharya, **Sushil Singh Chauhan**, Brajesh Chandra Choudhary, Debajyoti Choudhury.
   Physical Review D80, 015014 (2009).

2. "*Search for excited quarks in $q\bar{q} \to \gamma\gamma$ at the CERN LHC*", Satyaki Bhattacharya, **Sushil S. Chauhan**, Brajesh C. Choudhary, Debajyoti Choudhury.
   Physical Review D76, 115017 (2007).

CMS Analysis/Internal Notes

1. "*First Look at Photon+NJet(s) at CMS*", Sudha Ahuja, **Sushil Singh Chauhan**, Brajesh C. Choudhary.
   CMS Analysis Note-2009/117.

2. "*Quark Excitations Through the Prism of Direct Photon Plus Jet at the LHC*", Satyaki Bhattacharya, **Sushil Singh Chauhan**, Brajesh C. Choudhary, Debajyoti Choudhury.
   CMS Analysis Note-2009/009.

3. "*Search For Excited Quarks in $q\bar{q} \to \gamma\gamma$ at the LHC*", Satyaki Bhattacharya, **Sushil S. Chauhan**, Brajesh C. Choudhary, Debajyoti Choudhury.
   CMS Internal Note-2007/039.

Conference Papers/Poster Presentations

1. "*γ + jet Final State as a Probe of q^* at the LHC*", Satyaki Bhattacharya, **Sushil S. Chauhan**, Brajesh C. Choudhary and Debajoyti Choudhury.
   Poster presented at **XXIV International Symposium on Lepton and Photon Interaction at High Energies(LP09)** held in Hamburg, Germany, 17-22 August, 2009.

2. "*Search for Excited Quarks at the LHC*", Satyaki Bhattacharya, **Sushil Singh Chauhan**, Brajesh C. Choudhary and Debajoyti Choudhury.
   To be published in the proceedings of **18th DAE-BRNS High Energy Physics Symposium 2008**, held at Banaras Hindu University, Varanasi, India, 14-18 December, 2008.

3. "*Search for Excited Quark in γ + Jet Final State at the LHC*", Satyaki Bhattacharya, **Sushil S. Chauhan**, Brajesh C. Choudhary and Debajoyti Choudhury. Poster presented in **Particle and Nuclei International Conference(PANIC-2008)** held in Eilat, Israel, 9-14 November, 2008.

4. "*Search for Quark Compositeness in $q\bar{q} \rightarrow \gamma\gamma$ Channel at LHC*", Satyaki Bhattacharya, **Sushil S. Chauhan**, Brajesh C. Choudhary and Debajoyti Choudhury. Poster presented at **XXIII International Symposium on Lepton and Photon Interaction at High Energies(LP07)** held in Daegu, Korea, 13-18 August, 2007.
   Awarded prize for **BEST POSTER** in Experimental High Energy Physics category.

5. "*Projection of the annealing behaviour of irradiated Si sensors in the LHC environment*", S.Chatterji, Kirti Ranjan, Ashutosh Bhardwaj, Namrata, Ajay K. Srivastava, Ashish Kumar, Manoj Kumar Jha, Brajesh C. Choudhary, Pooja Gupta, **Sushil Singh Chauhan** and R. K. Shivpuri.
   Nuclear Science Symposium Conference, IEEE, Vol 2,(2004) 739-743 and poster presented in **IEEE Nuclear Science Symposium and Medical Imaging Conference** held in Rome, Italy in 2004.

Abstract

Within the Standard Model(SM) of particle physics, quarks and leptons are understood to be the fundamental particles. Their existence and various properties have been verified experimentally. Further search for substructure of quarks or study of quark compositeness is one of the important physics motivations of the LHC. Many different models of excited quarks($\Lambda < \sqrt{\hat{s}}$) and quarks substructure study via contact interactions($\Lambda >> \sqrt{\hat{s}}$) has been put forward but till now none of the experiments have found any such evidence. Various past and present experiments have put different lower bound on compositeness scale(Λ) and mass M_{q^*} of the composite/excited quarks. We have studied one such model in detail where the magnetic transition of the excited quarks is considered with ordinary quarks. We have evaluated the search potential of these states in $\gamma + jet$ and $\gamma\gamma$ final states at the LHC center of mass energy of $\sqrt{s}$ =14 TeV. The simulation was done at the generator level and we have used Compact Muon Solenoid(CMS) experimental setup for photon and jet candidate reconstruction. The track and calorimetric activities were used for isolation purpose to reduce SM backgrounds. The analysis shows that for a choice of $\Lambda = M_{q*}$ =2 TeV, an excited state q^* in $\gamma + jet$ mode can be discovered with 200 pb^{-1} of data, while a 5 TeV state can be confirmed with ∼140 fb^{-1} of integrated luminosity. Restricting the event selection to central pseudorapidity region with $|\eta^{\gamma,jet}|$ ≤1.5, a 3 TeV mass state can be discovered with less than 2 fb^{-1} of data. In $\gamma\gamma$ search mode, considering the diphoton invariant mass in 450 GeV to 1.5 TeV range, we estimated the achievable 99% CL exclusion contours in $\Lambda - M_{q^*}$ plane for 30, 50, 100 and 200 fb^{-1} of data. For a q^* mass state of 0.5 TeV, $\Lambda \leq 2.95(1.55)$ TeV can be excluded with 200(30) fb^{-1} of data at 99% CL. A detailed study of systematic uncertainty has been performed and its effect on results have been estimated.

Contents

List of Figures

List of Tables

Chapter 1

Introduction & Motivation

"Whatever nature has in store for mankind, unpleasant as it may be, men must accept, for ignorance is never better than knowledge"

Enrico Fermi.

1.1 Introduction

High energy physics is the study of the smallest elements of the universe, the subatomic particles that live within the atomic nuclei and those which come into brief existence in high energy collisions. The main goal is to understand the nature of these particles and their interactions. In last few decades, high energy physics has proven to be an efficient way in such scientific pursuits. In high energy physics experiments, the very basic idea is to steer together two accelerated beams of particles traveling in opposite directions and study the properties of the remnant particles that are produced in the collision.

1.2 A Brief History of Particle Physics

One might say that modern particle physics began in 1897, when J.J. Thompson discovered electron, that confirmed the idea of atomic substructure. Throughout the next

several decades chemists and physicists worked to understand the structure of the atom. The classical physics of Newton and Maxwell did not describe the emerging world inside the atom. The work of Max Planck, Neils Bohr, Werner Heisenberg, Erwin Schrodinger and others heralded the birth of quantum mechanics, a new set of physical laws to describe the behavior of particles at the microscopic scale [1].

In 1909, Ernest Rutherford's student reported some unexpected results from an experiment assigned by Rutherford. Later in 1911 Rutherford gave the concept of nucleus by analyzing the data of Geiger and Marsden on the scattering of $\alpha-$ particles against a very thin foil of gold. The data was explained by the assumption that the atom contains a nucleus of positively charge dense core and negatively charge cloud of electrons around it. Later with the discovery of Proton(1920) and Neutron(1932) [2], it was confirmed that ordinary matter is made of up of three particles, namely protons, neutrons and electrons.

During the same period, two of the most important breakthrough in science occurred: Relativity theory and Quantum theory. These two new theories together laid the foundation of Modern particle physics and Quantum field theory. In 1905 Albert Einstein's photoelectric theory proposed the existence of a particle, the "photon", as the quanta of electromagnetic field. In 1923 Arthur Holly Compton proved the existence of photon and its particle characteristics by his famous Compton scattering experiment. Subsequently Louis de Broglie extended particle-wave duality of matter. Erwin Schrodinger and Werner Heisenberg developed a new way of describing particles and physical observable using wave functions and operators.

In 1927, Paul Dirac combined the theory of Relativity and Quantum Mechanics into a theory called Quantum Field Theory (QFT) [3] and described the behavior of free electron. From the solution of the Dirac equation, arose the concept of anti-matter. In his attempt to explain the solution, Dirac predicted that for each particle there must exist an oppositely charged particle with the same mass. Later in 1933 Carl Anderson

discovered the anti-particle anti-electron (positron) and confirmed the prediction of Paul Dirac. This discovery was the seed for the "radiative effects" (annihilation of particle and anti-particle).

In 1933-34 Enrico Fermi put forth a theory of beta decay that introduced *weak interaction*. Fermi's theory of four fermion gave a mathematical proof of the existence of Pauli's 'neutron' dubbed neutrino (or the little neutral one as called by Fermi) and explained the continuous spectrum of electrons in the beta decay [4]. This is the first theory to make explicit use of neutrino.

With the discovery of proton and neutron the next immediate question was how does the nucleus remain in a bound state in a small region ($1fm = 10^{-15}m$) against the repulsive force between positively charged protons? The concept of "strong force" was postulated to overcome the electric repulsion among the protons in the nucleus. In 1933-34 Hideki Yukawa combined relativity and quantum theory to describe nuclear interaction between nucleons [5] by exchange of a new particle called meson and later on known as "pions". Yukawa concluded that the mass of these mesons should be $\sim$300 times the electron mass. In 1937 a particle with mass $\sim$200 times of electron mass was discovered in cosmic ray experiment and thought to be Yukawas's pion but later it was confirmed to be a muon(μ). The term "lepton" was introduced to describe the object that does not interact strongly and is light weight. The long awaited search for pion fructified in 1947 with its discovery by Cecil Powell of Bristol in cosmic ray experiment. By this time the particles were broadly categorized in three groups viz. *baryons, letpons, and mesons*. Further to this Murray Gall Men organized hadrons(mesons and baryons) into his famous *"Eightfold way"* which predicted the existence of Ω^- with a strangeness quantum number of -3.

With the pioneering work of Feynman, Schwinger, and Tomonaga, who developed quantum electrodynamics (QED) [6, 7, 8, 9], the era of modern particle physics started. The QED explained the electromagnetic phenomena at a basic level in terms of exchange

of photons. The predictions given by the QED theory were found to be true with remarkable precision.

The decade of 1940's and 50's were full of many interesting discoveries in particle physics which solved many known problems of that time but also tempted physicists to look at particle physics in new perspective. In 1947 a "strange" particle, K^+ caught much attention due to its slow decay pattern. New observables and new conservation laws were revealed. With progress in particle accelerator techniques, in subsequent years more and more new particles (so called hadrons and mesons) were found.

While the experimenters were searching for Ω^- meson and other particles, Gell-Mann was confidently exploring the meaning of SU(3) hadron symmetry. A more subtle possibility was that threefold symmetry was built into the structure of hadrons. Gell-Mann began to entertain the idea that neutrons and protons, and all other baryons are made up of three elementary particles which come in three types, or *flavors* namely *up*(u), *down*(d), and *strange*(s). He first called these elementary particles "quarks" [10]. Gell-Mann's theory builds a proton with two u quarks and one d quark or uud in short. In Gell-Mann's theory the mesons have fundamentally different structures compared to baryons. They always contain a quark and an anti-quark while baryons are made up of three quarks. Similarly the predicted Ω^- was made up of three s quarks, each contributing a strangeness of -1. Infact the discovery of Ω^- was confirmed in 1964 at Brookhaven National Laboratory(BNL) and from its subsequent decays its mass was measured to be 1683$\pm$12 MeV, very close to 1684 MeV predicted by Gell-Mann. This was a major success for the static quark model.

By this time the list of elementary particles known to the physicists comprised of u, d, and s quarks along with e^-, ν_e, μ^- and ν_μ and the photon; three quarks, four leptons and a boson. This apparent asymmetry between the number of leptons and quarks led Glashow and Bjorken to suggest, in 1964, that there might be a fourth quark to event up the numbers and they named it "charm quark". Later Glashow, IIiopoulos

and Maiani used the idea to provide an explanation for the non-occurrence of the decay $K_0 \rightarrow \mu^+ + \mu^-$. In 1974 two teams of experimentalists announced independent discovery of a new and unexpected type of meson [11, 12]. One group named it J and the other Ψ and now the particle is known as J/Ψ. An explanation already existed for this new particle and it was the lowest mass state of $c\bar{c}$. During 1975-1976 more such particles were discovered and existence of charm quark was firmly established. A new lepton *tau* (τ) was discovered in 1975 that once again created the unevenness between number of quarks and leptons. Just after two years, Leon Lederman announced the discovery of *Upslion*(Υ) which established the existence of another but more heavier *bottom*(b) quark [13]. The Υ meson was the bound state of $b\bar{b}$. Besides discovery of different quarks, by this time a new theoretical framework called Quantum Chromodynamics(QCD) was being developed to explain the interaction between the quarks.

After establishing the existence of new particle called τ lepton, M. Perl *et al.* performed a deeper study of the properties of the anomalous events they observed [14]. They concluded that if the events are to be explained by a single hypothesis, they must arise from the decay of a pair of new particles each of which decays to a charged lepton and two neutrinos. Due to the indirect and convincing evidence of tau-neutrino, scientists started searching for another quark to maintain the equal number of quarks and leptons. In 1995 Fermilab announced the discovery of *Top* quark [15, 16]. The *Top* quark was found after eighteen years of wait.

Throughout the 1970s and later, physicist tried to put various interactions into a single theory to explain the observed particles and their behavior. Glashow, Salam and Weinberg got success in unifying the electromagnetism and weak interaction together into Electroweak theory [17, 18] and predicted the existence of $W^{\pm}$ and Z^0 bosons which were later discovered by the UA1 and UA2 experiments at CERN[19, 20].

From the precise determination of the mass and width of the Z boson, the number of light neutrinos with standard coupling to the Z can be derived. Assuming that the width

is purely due to escaping neutrinos, the experiments at LEP (Large Electron Positron Collider) obtained $N_\nu = 2.984 \pm 0.008$ [21].

All these discoveries and our present understanding of fundamental constituents of matter and their interactions has led to the well tested theory of the Standard Model. Whenever a prediction for an experimental observable has been made by the Standard Model, excellent agreement with experiments have been found.

1.3 The Standard Model

A number of theoretical insights along with experimental discoveries in the last century have significantly advanced our understanding of elementary particles in nature and their interactions. The Standard Model (SM) combines Quantum Chromodynamics(QCD) and electroweak theory to describe the properties of elementary particles and interactions amongst them. For last several decades the SM has been thoroughly tested in different experiments. Almost all the results obtained so far agree with very high precision with the predictions of the SM. A more detailed description of the SM can be found in [22, 23]

1.3.1 Known Fundamental Particles

Fundamental particles can be separated into fermions, which are spin-1/2 particles and obey Fermi-Dirac statistics, and bosons, which are integral spin particles and obey Bose-Einstein statistics. The fundamental fermions are further divided into leptons and quarks.

Leptons: The leptons(l) are: electron(e), muon(μ), tau(τ) and their corresponding neutrinos ν_e, ν_μ, ν_τ. Three of the leptons e, μ, and τ carry a unit charge while neutrinos are chargeless. The e, μ, and τ interacts via electromagnetic and weak interaction while

neutrinos interact only through weak interaction. Earlier it was thought that neutrinos do not have any mass but recent experimental results have confirmed that indeed they carry a very small mass which accounts for the phenomena of neutrino oscillation [24, 25, 26, 27]. Because each lepton has its anti-particle there are a total of 12 leptons in the SM.

Quarks: The six quarks are: down(d), up(u), strange(s), charm(c), bottom(b) and top(t). Each quark carries either a fractional charge of $-\frac{1}{3}e$ or $+\frac{2}{3}e$. The d, s and b have $-\frac{1}{3}e$ charge while u, c and t have $+\frac{2}{3}e$ charge. The quarks interact via strong interaction as well as electromagnetic and weak interactions. Since quarks are fermions(spin $\frac{1}{2}$) and should obey Pauli's exclusion principle hence another quantum number "color charge" was assigned to each quark. It was formulated that each quark comes in three colors, red, blue and green. The strong interaction binds quarks to form what is known as mesons and baryons for e.g. proton(uud) and neutron(udd). The meson family has all it members with one quark and one anti-quark as its constituent e.g. $\pi^0(u\bar{u}), \pi^+(u\bar{d}), K^0(d\bar{s})$ and $\bar{K^0}(s\bar{d})$. Similarly the baryons are made up of three quarks and anti-baryons of three anti-quarks. Properties of mesons and baryons can be derived from quarks quantum numbers. Table 1.1 shows three generations of the family of quarks and leptons.

Generation	Leptons (spin=$\frac{1}{2}$)			Quarks (spin=$\frac{1}{2}$)		
	Flavor	Charge	Mass (MeV/c^2)	Flavor	Charge	Mass (MeV/c^2)
1	e	-1	0.511	u	$+2/3$	$1.5 - 4.5$
	ν_e	0	$< 3 \times 10^{-6}$	d	$-1/3$	$5 - 8.5$
2	μ	-1	105.7	c	$+2/3$	$(1.0 - 1.4) \times 10^3$
	ν_μ	0	< 0.19	s	$-1/3$	$80 - 155$
3	τ	-1	1777	t	$+2/3$	$(172.6 \pm 1.4) \times 10^3$
	ν_τ	0	< 18.2	b	$-1/3$	$(4.0 - 4.5) \times 10^3$

Table 1.1 Three generations of quarks and leptons, the basic constituents of the SM.

1.3.2 Fundamental Interactions and their Mediators

All the particles and anti-particles in the SM interact via three known fundamental forces: electromagnetic, weak and strong interactions. The "gravity" is the fourth and the weakest amongst all. In Table 1.2 we summarize the fundamental forces and their mediator along with their important properties. All these fundamental interactions can be described by gauge field theories, which can be regarded as the common nature of all these forces.

Force	Gauge Boson	Charge	Spin	Mass (GeV/c^2)	Range	Rel. Strength
Strong	Gluons (g)	0	1	0	$10^{-15}m$	1
EM	Photon(γ)	0	1	0	∞	1/137
Weak	$W^{\pm}$	±1	1	80.42	$10^{-18}m$	10^{-5}
	Z^0	0	1	91.19		
Gravity	Graviton (G)	0	2	0	∞	10^{-38}

Table 1.2 Fundamental forces with their mediator and some of their properties.

1.3.2.1 Electromagnetic Interaction

The first unification of fundamental forces in human history was the unification of electric and magnetic forces achieved by Maxwell in 1864 and is known as electromagnetism. The electromagnetic interaction occurs between two particles having electric charge. The quantum approach to the electromagnetic interaction is called Quantum Electrodynamics or QED [6, 7, 8, 9, 28]. QED involves the exchange or production of photons. Thus photons are the mediator of electromagnetic interaction. Now we know that QED is a $U(1)$ Abelian gauge invariant theory [29, 30]. Electromagnetic interaction is responsible for the binding force that causes negatively charged electrons to combine with positively charged nuclei to form atoms. In quantum field theory, any changing electromagnetic fields or electromagnetic waves can be described in terms of photons, the quanta of energy.

1.3.2.2 Weak Interaction

The weak force is the reason for the generation structure of the quarks and leptons. This is because it changes particles from one type to another. The weak force is felt by both quarks and leptons. The weak force has very short range (10^{-18}m) and is extremely feeble compared to strong and electromagnetic forces. Weak interaction is classified as charged or neutral, depending on whether a particle participating in a weak reaction suffers a change of electric charge of one electronic unit or not. The strong and electromagnetic interactions respect spatial inversion symmetry (they conserve parity) and are also particle-antiparticle (charge conjugation) symmetric, whereas the weak interaction violates these two symmetries.

1.3.2.3 Strong Interaction

Quantum Chromodynamics is the gauge theory associated with strong interaction and describes the interaction amongst color charged particles. The strong force is responsible for binding quarks together to form hadrons as well as binding protons and neutrons to form nuclei. Also referred to as the color interaction, the strong force binds colored quarks through the exchange of colored gluons. Both quarks and gluons carry color charge. Gluons are the gauge bosons that mediate the strong force between the quarks. Gluons have eight color states consisting of color and anti-color. They can modify a quark's color state to anti-color state. The properties of the color charge is explained by a gauge symmetry known as $SU(3)_C$. This gauge symmetry is at the core of QCD. Each quark is in the basic triplet of the $SU(3)_C$ group. The gluons are described by the adjoint representation of this group, which explains why gluons carry both color and anti-color charge at the same time.

One of the important aspects of strong interaction is asymptotic freedom which describes the behavior of quarks inside hadrons and hadron formation.

Asymptotic Freedom: Asymptotic freedom and quark confinement can be expressed in terms of the strong coupling constant (α_s), where α_s is determined by $\alpha_s = \frac{g^2}{4\pi}$. The perturbative calculation of the theory requires renormalization to remove ultraviolet divergences. The renormalization introduces the renormalization scale(μ). The dependence of α_s on renormalization scale is given by the following equations which is popularly known as the β function:

$$\mu\frac{\partial\alpha}{\partial\mu} = -\frac{\beta_0}{2\pi}\alpha_s^2 - \frac{\beta_1}{4\pi^2}\alpha_s^3 - ..... \tag{1.1}$$

where n_f is the number of quark flavor with mass less than the energy scale μ. In solving the differential equation a constant(μ_0) is introduced which is chosen to be equal to M_Z. The μ_0 is one of the constants related to QCD and must be determined from experiments. After solving the equation for α_s

$$\alpha_s(Q) = \frac{\alpha_s(\mu^2)}{1 + \frac{\alpha_s(\mu^2)}{12\pi}(11c - 2n_f)log(\frac{Q^2}{\mu^2})}, \tag{1.2}$$

where Q is the momentum transferred in the interaction and c is the number of quark colors i.e. 3.

$$\alpha_s(Q^2) = \frac{12\pi}{(11c - 2n_f)\ln(Q^2/\Lambda)} \tag{1.3}$$

where,

$$\Lambda^2 = \mu^2 exp\frac{-12\pi}{(11c - 2n_f)\alpha_s(\mu^2)} \tag{1.4}$$

The characteristic scale Λ is the chromodynamics scale and has a value of roughly 200 MeV. The above expression is presented in the leading log approximation where the expansion has been summed to all orders, retaining only terms containing the leading-order logarithm. Equation 1.3 shows that if $Q^2 \to \infty$ (distance $\to 0$), $\alpha_s \to 0$ which is also known as "asymptotic freedom" [31]. Asymptotic freedom justifies the use of perturbative calculations in the high-Q^2 regime. In other words Λ_{QCD} scale sets the

boundary between asymptotically free quarks and the quarks bounds in hadrons when $Q \backsim \Lambda_{QCD}$. From the running coupling constant we see that quarks are bound weakly at short distance and strongly at large distances(*quark confinement*). The value of α_s has been estimated experimentally by measuring the cross section of many QCD processes. Fig. 1.1 shows the latest results of α_s measurements from different experiments [32].

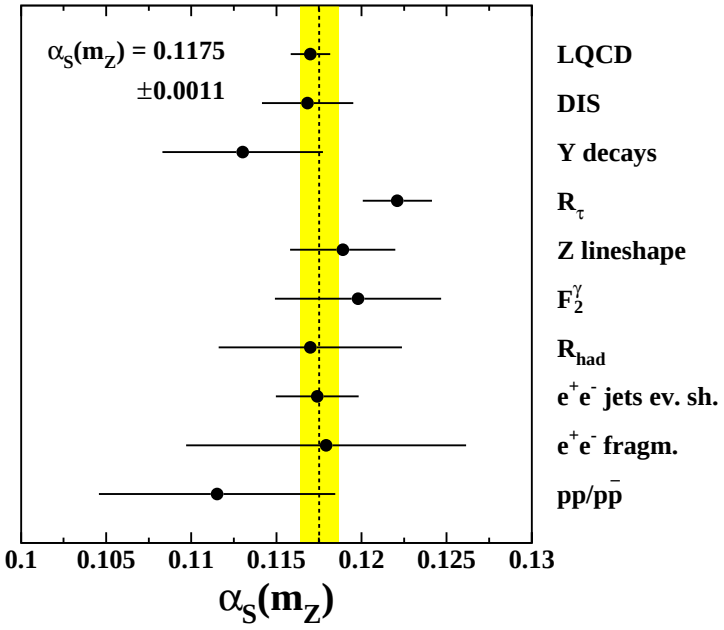

Figure 1.1 Measurement of α_s at M_Z in different experiments, using various QCD processes.

Hadronization: The renormalization QCD coupling is small only at high energies or small distances and QCD behaves as perturbative theory. At large distances it becomes strongly coupled and perturbation breaks down. In this confinement region, colored partons combines and give colorless hadrons. This process is known as hadronization. The process of hadronization has yet to be understood in a convincing way and this has led to different phenomenological models such as, *cluster* and *string* models.

1.3.3 Electroweak Unification and Higgs Mechanism

Electroweak interaction unifies the electromagnetic and weak interactions. This unification was achieved by S. Glashow, S. Weinberg and A. Salam [17, 18]. The $SU(2)_L \bigotimes U(1)_Y$ is the symmetry group associated with this theory. The $SU(2)_L$ group describes weak isospin(T) and acts only on the left-handed fermion field. The $U(1)_Y$ group describes weak hypercharge(Y). The electric charge(Q) is related to the weak isospin and weak hypercharge by $Q = T_3 + \frac{Y}{2}$ where T_3 is the third component of weak isospin. This implies that the charge is conserved in the electroweak theory. In $SU(2)_L \bigotimes U(1)_Y$ model, quarks and leptons are assigned as left handed doublets and right handed singlets. The weak interaction has a very short range and exists between any of the leptons and quarks. It is responsible for the radioactive β-decay of nuclei. The mediators of the weak force are $W^{\pm}$ and Z^0 bosons as summarized in Table 1.2. These bosons acquire their mass in the process of spontaneous electroweak symmetry breaking(EWSB) of Higgs mechanism.

Higgs Mechanism: The electroweak theory is based on $SU(2)_L \bigotimes U(1)_Y$ has massive gauge bosons which have different masses and has been confirmed experimentally. This means that it is not a perfect symmetry and there must be some underlying mechanism which results in such splitting of masses. In simple words the spontaneous symmetry breaking occurs when the Lagrangian of the system is invariant under a symmetry group, but the vacuum state(v) is not. A schematic illustration is depicted in Fig 1.2

To realize the observed masses of $W^{\pm}$ and Z^0 bosons through Higgs mechanism an extra spin-0 complex doublet, the Higgs field, is introduced by hand into the theory.

$$\Phi \equiv \begin{pmatrix} \Phi^+ \\ \Phi^0 \end{pmatrix} \tag{1.5}$$

This field is neither a matter field nor a mediator field as in case of strong and electromagnetic interactions. The Lagrangian of Higgs field is given by

$$L = (\partial_\mu \Phi)^\dagger (\partial^\mu \Phi) - \mu^2 \Phi^\dagger \Phi - \lambda (\Phi^\dagger \Phi)^2. \tag{1.6}$$

This extra field respects the local gauge invariance and interacts with the massless gauge boson $W^\pm$ and Z before EWSB. Expanding this field around its vacuum expectation value (*vev*) the field can be re-written in terms of v and H, the real field with zero *vev*, then the Higgs field becomes

$$\Phi \equiv \begin{pmatrix} \Phi^+ \\ \Phi^0 \end{pmatrix} \rightarrow \begin{pmatrix} 0 \\ \mathrm{v} + \mathrm{H} \end{pmatrix} \tag{1.7}$$

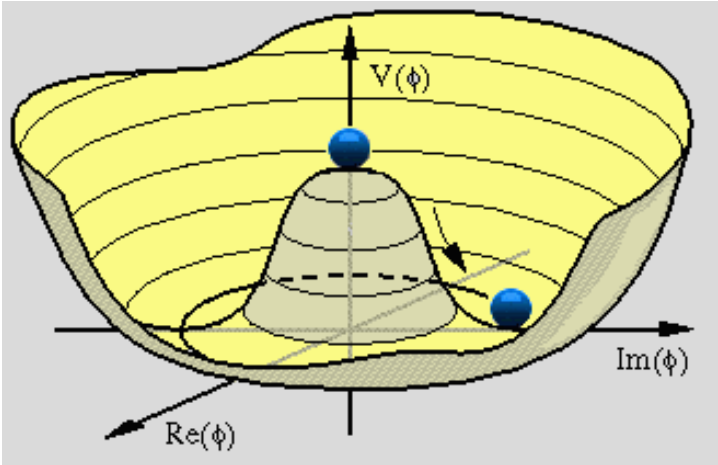

Figure 1.2 Behavior of Higgs potential in spontaneous symmetry breaking.

For $\mu^2 < 0$ the Φ acquires a non vanishing *vev* which breaks the $SU(2)_L \bigotimes U(1)_Y$ symmetry. The nature of the theory remains same but the particular solution considered for ground states loses its uniqueness. Fig 1.2 shows the new ground states where it is not unique. This symmetry breaking generates another three degrees of freedom which refers to be the zero-excitation along with the ground state of the unbroken symmetry. The extra degrees of freedom are absorbed into the mathematical structure and they provide the mass to the gauge bosons. The presence of the Higgs field generates masses

for the fermions through the introduction of *Yukawa* couplings in Higgs-fermions vertices with a strength proportional to their mass. As with every field there is a quantized state, similarly the Higgs boson is the quantized state of the Higgs field. This is one of the last missing pieces of the SM and a hunt is on for it at various collider experiments. The lower direct bound from LEP experiments has been put at M_H >114.4 GeV [33] while the indirect constraints from electroweak measurements and unitarity condition estimate a preferred range of 144.4 GeV< M_H < 185 GeV at 95% C.L. [34, 35].

1.4 Challenges to the Standard Model

The Standard Model has been tested for decades and has proven to be extremely successful. Now with increased center of mass energy and luminosity at the Tevatron and with LHC era approaching, we are on the threshold of either finding the last missing piece of the theory- the Higgs boson, or ruling out the Standard Model(and few other models) above certain energy scale. Despite the success of the Standard Model, it is rightly believed that it is not the complete or the final theory. There are various extensions and modifications to the Standard Model to achieve grand unification(GUT, the unification of the strong interaction with the EW interaction). Even without such a big ambition as the GUT in mind, there are Standard Model criticisms that are based on sound but purely conceptual considerations. Amongst them, the most famous is the hierarchy problem which states that the large barren gap between the Higgs boson mass and the Plank scale is very unnatural. Also the Standard Model does not provide a clear picture about how the vacuum condensate is produced. As a possible alternative there are theories in which the fermions can aquire mass without the Higgs bosons. Also there are models in which Higgs bosons are not fundamental particles but composed of other particles [36]. Attempts of applying the Standard Model to cosmology also raised some interesting questions that seem to be beyond the capability of the Standard Model. For

example, the baryon and lepton genesis problem in which the Standard Model seems not to be able to provide enough CP violation. The Standard Model does not provide explanations for various neutrino problems, for example, the massive neutrino is not simply produced by the Yukawa coupling of the Standard Model Higgs boson since the right handed neutrinos have no weak isospin or weak hypercharge. Thus its coupling to the Higgs boson having weak hypercharge is not allowed. This leads to the search for sterile or Marjorana neutrinos which do not belong to the SM but are good candidates for the dark matter.

1.4.1 Unification of Fundamental Forces

An important goal of theoretical physics is to achieve a further simplification in understanding of nature and to describe the presently known three basic interactions in a unified way, usually referred to as the Grand Unified Theory (GUT). The SM leaves, unexplained the reason for very different strengths of the gauge group of the strong and electroweak interaction is $SU(3) \bigotimes SU(2) \bigotimes U(1)$ [22], and particular values of the quantum numbers. The idea of Grand Unified Theory(GUT) is that $SU(3)$, $SU(2)$ and $U(1)$ are subgroups of a larger gauge symmetry groups G and that quarks and leptons belong to the same multiplet of G. This higher symmetry is supposed to be unbroken above some very large mass scale.

The GUT is the natural way to extend the SM, however, it has a major problem, the so called "*hierarchy* problem".

1.4.2 *Hierarchy* Problem

Despite the fact that the SM has been thoroughly tested at the experimental level, it is not the complete story. The SM contains many free parameters which can only be determined by the experiments, and it offers no explanation for many of the puzzling

aspects such as the origin of the free parameters of the theory. It is certainly not able to describe the physics at Plank's scale (10^{19}GeV) where the quantum gravitation effect becomes important. So one of the fundamental questions of physics is- why there are so many orders of magnitude between the Plank scale and the weak scale without any intermediate new physics. Although such puzzling queries do not affect the predictions of the SM except in the area of Higgs sector!

The SM Higgs field is a complex scaler field, Φ with a potential V defined as,

$$V = \mu^2(\Phi^\dagger\Phi) + \mid \lambda \mid (\Phi^\dagger\Phi)^2 \tag{1.8}$$

where μ is the mass of the scaler field and $\mu^2 < 0$ is required for electroweak symmetry breaking. The vacuum expectation value of the field is given by $< \Phi >= \sqrt{-\mu^2/2\lambda}$. It is known from electroweak measurements that $< \Phi > \approx$ 246 GeV. So if the SM is responsible for Higgs mechanism of EWSB then μ^2 must be of the order of -$(100GeV)^2$. Every particle which couples to the Higgs field gives correction to μ^2 value and these

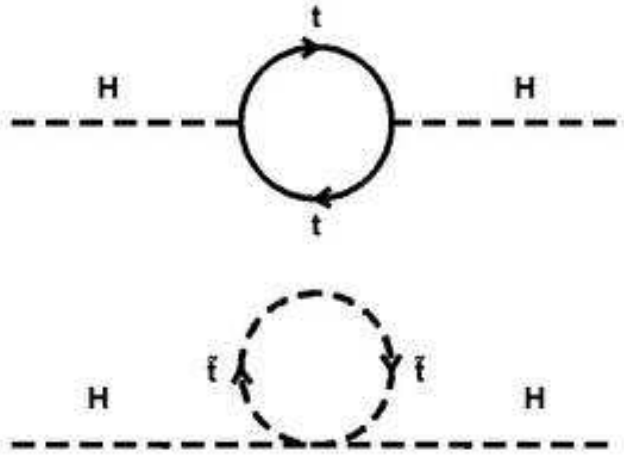

Figure 1.3 Feynman diagrams which give loop corrections to the Higgs mass.

corrections are proportional to the square of the energy scale at which the loop integral is cut-off(to remove divergences). Fig 1.3 illustrates one such scenario where top quark could give correction to the Higgs mass. This energy scale would be the new scale at which some new physics enters into the picture to prevent further corrections and this scale could be anywhere between the weak and the Plank scale. To assume that it is low enough to prevent disastrously large corrections to μ^2, but high enough to have had no measurable effect given the energy reach of today's accelerators, it has to lie in an extremely narrow region of the complete allowable scale. In absence of satisfying model, it seems a very unnatural assumption. The largest correction would be of the order of $(mass)^2$ of the heaviest particle that couples to the Higgs field. This implies that to keep μ^2 around -$(100GeV)^2$, there would have to be no other new particle that couples, directly or indirectly, to the Higgs field in a very large energy range up to and including the Plank scale of (10^{19}) GeV. But this idea is considered equally unnatural. The other possibility could be that various terms which contribute to μ^2 corrections cancel each other so that a value of -$(100GeV)^2$ can be achieved. Although there may be perfect cancellation but the very idea that the corrections are of the Plank scale, seems to be unnatural.

A satisfying theory would be the one which can, without requiring any parameter conspiracies or veto on new physics, tells how the correct size of μ^2 arises naturally. The SM is not able to give a viable justification to this problem and it is known as the "*hierarchy*" or "*naturalness*" problem.

1.5 Motivation

It has been the mankind's quest to know the most fundamental objects or entity of which the matter is made. This quest has resulted in establishing a series of discoveries

or understanding of entities which were thought to be the basic building blocks of matter and at present quarks and leptons are the last candidates in this chain.

$$Matter \rightarrow Molecules \rightarrow Atom \rightarrow Nucleons \rightarrow quarks/leptons \rightarrow \textbf{What Next} \; ??$$

This hunt for more fundamental particles of which the quarks and leptons could be composed is still on and the LHC may add to our understanding either with a possible discovery or evidence.

1.5.1 Theoretical Motivation

The SM provides a successful mean of classifying the physical processes which fill the universe. But there are many unresolved fundamental questions such as hierarchy problem, unification of forces etc. These questions need to be addressed with more fundamental physical theory from which the SM could arise naturally. One of such puzzles is "*why their exist three nearly identical generations of quarks and leptons??*" Does it suggest an underlying structure like the periodic table of elements? The compositeness of quark is one such scenario which could provide the answer. It is also possible that composite model may be able to explain parameters such as particle mass, electric charge, and color charge which the SM has failed to explain.

1.5.2 Experimental Scenario

The LHC will be a parton-parton resonance factory in a previously unexplored mass energy regime. With the planned center of mass energy and optimum luminosity we have a good chance of finding new physics at the LHC. Nature may surprise us with previously unanticipated new particles. For compositeness study one will search for generic dijet, $\gamma + jet$, $\gamma\gamma$ and other resonances, either for a particular model or in a model independent way. Not only resonances but an excess of events over the SM production can also be a signal for some new physics. It should be possible to discover these resonances with

early data at LHC if they have large enough cross section. In last two decades several experiments have tested the SM with very high precision and various measurements of known SM processes have been made. Many of these are well understood with ever greater accuracy. One of the best examples is $t\bar{t}$ production where the experimental error on mass measurement has been achieved at the level of $\sim$1% [37]. This has been possible because of the advancement in the state-of-art technology in electronics and detector development. In the next chapter we will review the early searches for quark compositeness but it is also true that no positive results have been found as yet. This itself prompts us to explore the LHC phase space for q^* search. Another encouraging fact for the present work is that the background processes for $q^* \rightarrow \gamma + jet$ and $\gamma\gamma$ are very well understood both theoretically as well as experimentally. The theoretical understanding has immensely benefited from the experimental inputs. Next-to-leading(NLO) order calculations are available for many known SM processes and they describe the data very well. For example Figs. 1.4 and 1.5 show the experimental results compared to theoretical predictions [38, 39] for isolated direct photon production, one of the background for the search of q^* presented in this thesis. Similarly direct diphoton final state has been studied in detail, due to its immense importance in search of an intermediate mass Higgs boson [40, 41].

1.6 An outline of the dissertation

This dissertation describes search for excited or composite quarks in two different final states, namely $pp \rightarrow \gamma + jet$ and $q\bar{q} \rightarrow \gamma\gamma$ via q^* at $\sqrt{s} = 14$ TeV at the LHC. The analysis employs kinematical and isolation selection criteria to observe such signals with the CMS detector. Discovery potential and achievable limits have been presented as the result. The systematic uncertainties and their possible effects on the result has been

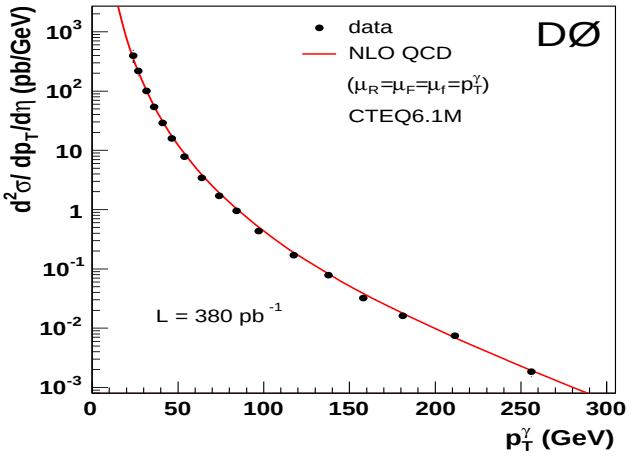

Figure 1.4 Differential cross section for isolated photon production as a function of P_T^γ at DØ. The NLO QCD calculation using JETPHOX is also shown.

estimated. The thesis is organized in **eight** chapters, a brief description of each chapter is given below.

A brief introduction of particle physics, its achievements and unsolved questions have been presented in **Chapter 1**. The motivation for the search of composite quark has been outlined briefly. It thus lays the foundation for understanding the goal behind the present work discussed in detail in later chapters.

Chapter 2: We discuss the effective Lagrangian for the theory and the contribution from new physics for different final states along with their properties. Possible signatures and their characteristics have also been discussed. A brief review of earlier phenomenological and experimental studies have been outlined.

Chapter 3: This chapter gives a brief introduction of the LHC machine design and different experiments situated on it. A detailed description of one of the detectors at the LHC, the Compact Muon Solenoid(CMS), has been presented. Various sub-detectors of the CMS, their design and performance have been discussed in detail.

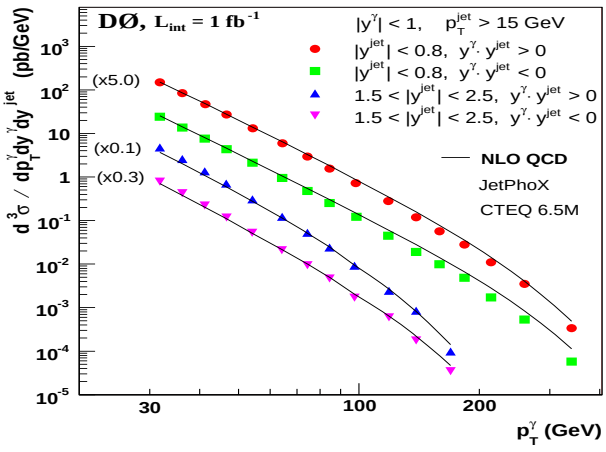

Figure 1.5 Triple differential cross-section for $p\bar{p} \rightarrow \gamma + Jet + X$ as a function of P_T^γ at DØ. Theoretical predictions for different pseudorapidity ranges are from JETPHOX package with CTEQ6.5M PDF set.

Chapter 4: In this chapter we describe the event generation of signal and background for the two analysis carried out in this thesis. As both the analysis are done in a similar manner, hence first we give a detailed description for the $\gamma + jet$ and then diphoton event generation. We also briefly discuss photon and jet candidate formation algorithms.

Chapter 5: In this chapter we separately describe the analysis of two different final states. We also outline different isolation parameters and various kinematical requirements to separate the signal from the backgrounds.

Chapter 6: In this chapter we discuss statistical methods for $\gamma + jet$ and $\gamma\gamma$ final states used for limit evaluation on compositeness scale and the mass of the excited states. A brief introduction of frequentist method has also been given in the beginning of this chapter.

Chapter 7: In this chapter we present results for both the analysis. We also discuss the major sources of systematic uncertainties. The effect of these uncertainties on the

final outcome has also been presented.

Chapter 8: In this chapter we present the summary and conclusion of the work.

Appendix-A: In appendix-A we discuss the co-ordinate system of the detector and the parton kinematics in a hadron collision.

Appendix-B: This appendix presents a simplified picture of the parton model and different stages of parton-parton collision.

Chapter 2

Physics of Compositeness

"Imagination is more important than knowledge."

- Albert Einstein

2.1 Introduction

The standard model of quarks and leptons does not predict their mass spectrum or the number of their families. This suggests that there might exist a more fundamental basis. In one such scenario, fundamental constituents called *preons* interact via a new strong gauge interaction of metacolor. Below a certain characteristics energy scale Λ, the interaction becomes strong and binds the *preons* together to form quarks, leptons and heavy bosons. The signature for this compositeness could be a significant deviation in the measured cross section(in certain final states) at large center of mass energy compared to the predictions of the Standard Model. There is, as yet, no experimental evidence of such a deviation. Null results from such experimental searches are used to set lower bounds on the energy scale Λ above which composite particles of mass q^* can be found.

2.2 A Simple Analogy

We know that the excited states of particles, atoms and molecules are common in nature, for e.g., the excited state of hydrogen atom as shown schematically in Fig. 2.1.

In similar manner if quarks have substructure, we expect them to exhibit excited states.

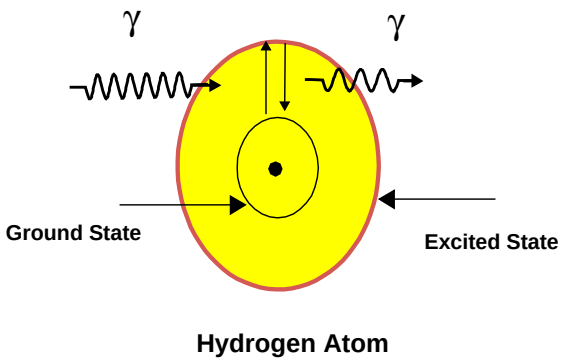

Figure 2.1 Schematic presentation of the ground and excited state of the hydrogen atom. A photon is absorbed by the ground state of the hydrogen atom to reach the excited state. An excited hydrogen atom radiates photons to reach its ground state.

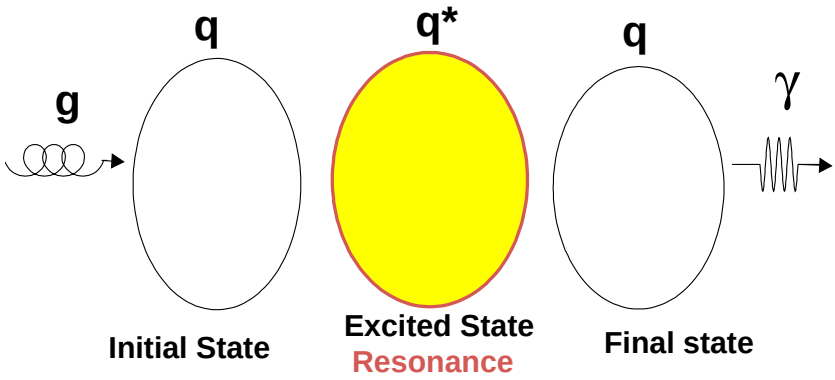

Figure 2.2 Analogy with excited atom: Excited state resonance of composite quark.

For example a gluon interaction can excite such quarks and they will radiate either a photon or gluon and come to ground state (as shown in Fig. 2.2). The cut-off scale at

which the excitation occurs can be translated roughly into the radius(r) of a composite quark e.g.

$$\hbar = \Delta x\ \Delta p \sim 2r(\Lambda/c), \text{ where } r \simeq 10^{-19} \text{ m-TeV}/\Lambda$$
$$\text{For } \Lambda = 10(1) \text{ TeV} \rightarrow r \sim 10^{-20}(10^{-19}) \text{ m}$$

2.3 Earlier Searches for Excited States

The excited state or compositeness study can be broadly categorized into two different scenarios based on the compositeness scales. If the scale of compositeness is low compared to the center of mass energy available (i.e $\Lambda < \sqrt{\hat{s}}$), narrow resonances of excited particles can be produced on shell. On the other hand if $\Lambda >> \sqrt{\hat{s}}$, compositeness will manifest as 4-fermion Contact Interactions(CI). Various experiments have tested many such models based on CI or excited state production of quarks, leptons and neutrinos and has evaluated bounds on the parameters (Λ, M_{q*}, couplings etc.) of such models. As can be readily appreciated, different production modes (and decay channels, wherever applicable) probe different aspects of the effective theory that govern the low energy interaction of these excited states. In next section we briefly summarize some of the important limits on these excited states from different experiments and expectations for the LHC experiments.

2.3.1 Limits from HERA

The **H**adron **E**lectron **R**ing **A**ccelerator(**HERA**) at DESY, Hamburg operated during 1992-2007. It consisted of two storage rings. In one ring the protons circulated in anticlockwise direction with an energy of 900 GeV while in the second ring polarized beam of electrons or positrons circulated in the opposite direction with an energy of 27.5 GeV. The HERA ring had four experiments situated on it, namely H1, ZEUS,

HERMES and HERA-B. The H1 and ZEUS were two large experiments which studied and confirmed the nature of strong force and the internal structure of the proton.

If leptons and quarks are not fundamental particles but are composite, excited states of these particles can exist. HERA, having electron and proton in the initial state, was a good place to search for such states as proton inner structure has been revealed by such collisions. One of the best way in which an excited fermion can be detected is via their decay into an ordinary fermion and a gauge boson, for e.g. $e^* \rightarrow e\gamma$. These excited fermions could be produced through t-channel exchange of a γ or Z^0 as shown in Fig. 2.3.

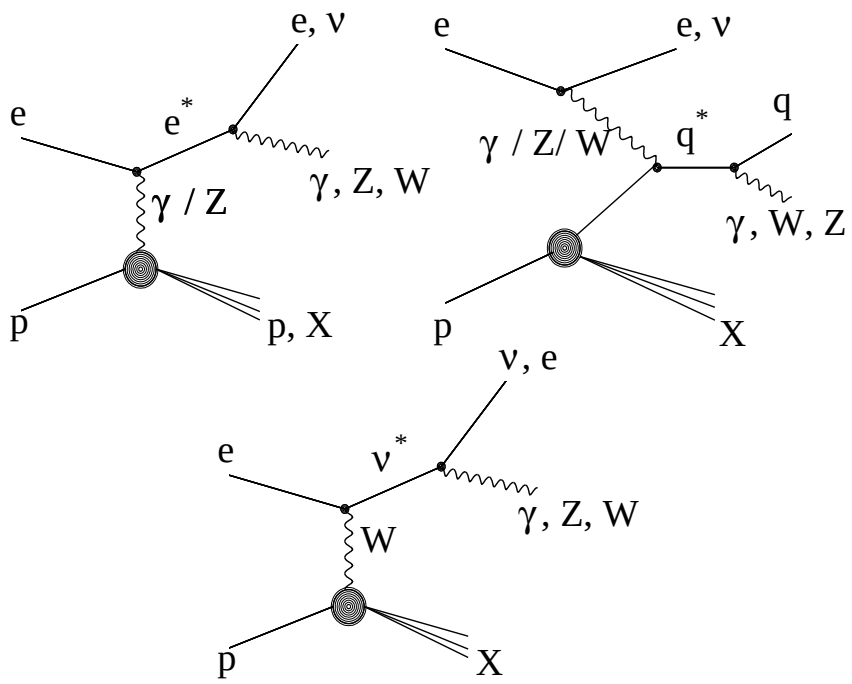

Figure 2.3 Excited fermion production in different final states in ep collision.

The ZEUS and H1 experiments searched for these excited states using $e^{\pm}p$ data at HERA [42, 43]. The H1 experiment searched for q^* and ν^* with final states of γ, $W^{\pm}$ and Z^0(see Fig. 2.3). For decay of heavy gauge bosons($W^{\pm}$ and Z^0) only hadronic modes have been considered for ν^* search. For q^* study $e^{\pm}$, $\mu^{\pm}$ and hadronic decays were analyzed.

Fig. 2.4 shows limits on q^* search in different decay modes at H1 experiment [44]. The different curves show the upper limit on f/Λ at 95% CL as a function of mass of the excited state. Here f, f_s and f' are the form factors associated with the three SM gauge groups, SU(2), SU(3) and U(1) respectively. These form factors can be interpreted effectively as associated weight factors which modifies $\Lambda \rightarrow \Lambda/f$.

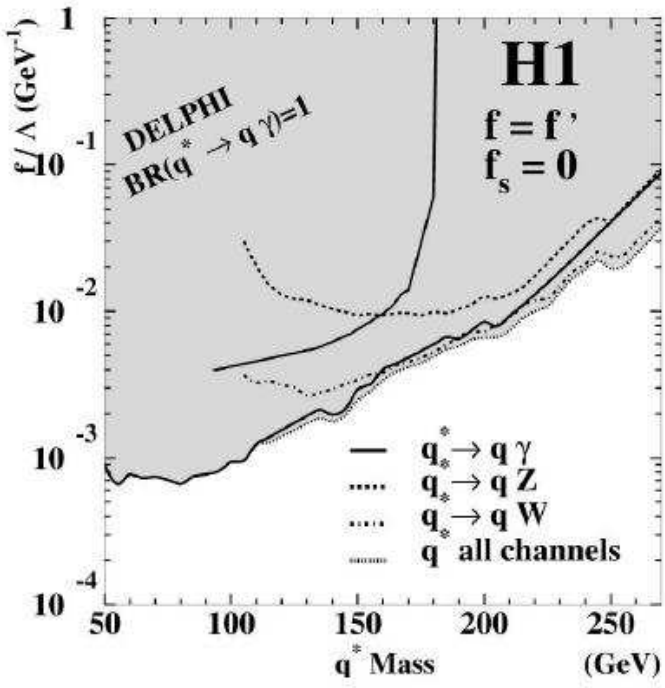

Figure 2.4 Limits on search for excited quark in H1 experiments at HERA.

For ν^* search H1 looked at the processes where an excited neutrino can be produced in a t-channel exchange of W boson in ep collision. The ν^* can decay through the following modes: $\nu^* \rightarrow \nu\gamma$, $\nu^* \rightarrow eW$ and $\nu^* \rightarrow \nu Z$. The production cross section for these processes largely depends on the value of f/Λ. The data was analyzed for two different scenario $f = +f'$ and $f = -f'$ and the results obtained [45] are shown in Fig. 2.5. With the assumption of $f/\Lambda = 1/M_{\nu^*}$, excited ν upto a mass of 213 GeV(196 GeV) are excluded for $f = -f'(f = +f')$. The most stringent limit on M_{ν^*} at LEP has

been obtained by the L3 and DELPHI experiments and the limits are compared with H1 results in Fig. 2.5 [46, 47].

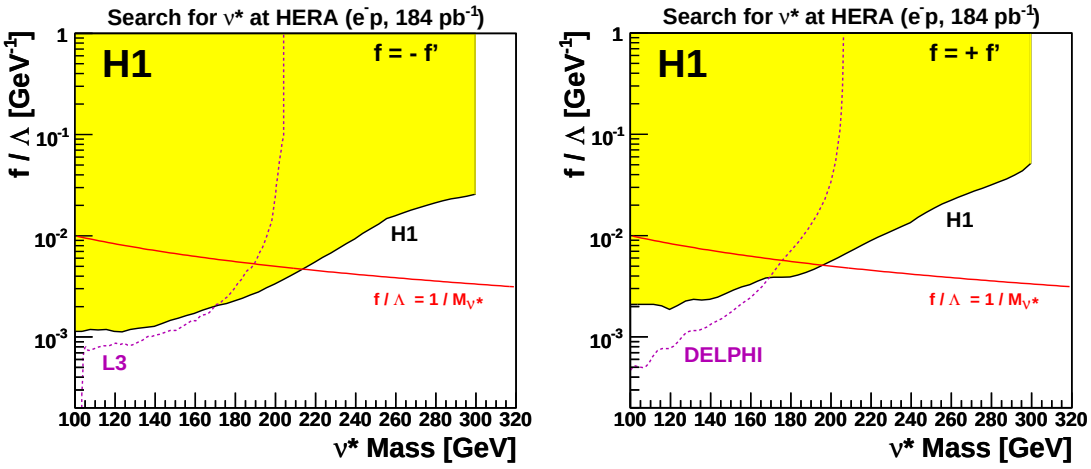

Figure 2.5 Limits on ν^* from H1 experiment at HERA. For comparison limits are also shown from L3(left) and DELPHI(right) experiments at LEP.

The H1 experiment at HERA searched for e^*(excited e) in the decay modes $e^* \to e\gamma$, $e^* \to eZ$ and $e^* \to \nu W$ with subsequent hadronic decay of W and Z [48]. At 95% CL the study excluded an e^* with a mass lower than 272 GeV. This analysis also made a similar assumption of $f/\Lambda = 1/M_{e^*}$. For e^* production(and subsequent decay) both gauge and four-fermion contact interactions were considered together at H1. Until now data from HERA experiments does not show any compelling evidence either for excited charged fermions or excited neutrinos.

2.3.1.1 Limits on the Size of Composite Particles

An alternate method used at HERA to study possible fermion substructure was to estimate the size of the composite particle. For this study it was assumed that electroweak charges of quarks and/or leptons have a finite size of radius R. The γ and Z are still assumed to be pointlike particles [49]. Thus one can introduce a *classical* form factor $F(Q^2)$ at the fermion-gauge boson vertices, which are expected to diminish the SM

cross section at high momentum transfer. These form factors were parameterized in the following form,

$$F(Q^2) = 1 - \frac{1}{6} < r^2 > Q^2 \tag{2.1}$$

$$\frac{d\sigma}{dQ^2} = \frac{d\sigma^{SM}}{dQ^2} F_e^2(Q^2) F_q^2(Q^2) \tag{2.2}$$

where $R(= \sqrt{< r^2 >})$ is taken as the measure of the particle size and r is the radius of electroweak charge distribution. For simplicity the data was analyzed for F_q requiring that $F_e = 1$, which implies that the positron has no structure and is pointlike. This is a valid assumption well established from e^+e^- and $(g-2)_e$ experiments [50]. The result puts an upper bound on the light quark radius in compositeness scenario to be $R_q < 1.7 \times 10^{-16} cm$. These results were found compatible with other estimations obtained from different experiments. For example the CDF collaboration came up with a limit of $R_q < 1.1 \times 10^{-16} cm$ [51] in Drell-Yan production.

2.3.2 Limits from LEP

The **L**arge **E**lectron **P**ositron(**LEP**) collider at CERN was commissioned in 1989 and operated until 2000. It collected data in two phases. In the first phase it operated at Z pole and in its second phase it produced W boson pair. A total of four experiments ALEPH, DELPHI, L3 and OPAL collected data at LEP. The main goals of these experiments were to search for new physics along with confirmation of electroweak symmetry breaking and precision measurement of various properties of electroweak bosons.

The electron positron annihilation at LEP constituted an excellent environment for search of excited leptons. At the LEP collider, excited leptons e^*, μ^*, τ^* and ν^* are expected to be produced in pair upto the kinematical limit of $\sqrt{s}/2$, and decay via the emission of a gauge boson(γ, Z or $W^{\pm}$) [52]. The OPAL collaboration searched for electromagnetic decays of e^*, μ^* and τ^* in the center of mass energy range of 183 -

209 GeV. These excited states are either produced in pair or in association of a SM lepton. The pair production occurs mainly through s-channel γ/Z, while t-channel also contributes to the production cross-section. The final states, which have been studied, mainly comprises of $ll\gamma$, $ll\gamma\gamma$ or $l\gamma$ where one lepton(l) remains undetected. From pair production searches the OPAL collaboration has put a lower bound of $M_{l^*} > 103.2$ GeV [53].

The DELPHI experiment mainly searched for excited electrons. From their analysis they put a lower bound of M_{e^*} >295 GeV at 95 % CL for the $e^*e\gamma$ chiral magnetic couplings [54].

The L3 experiment searched extensively for excited leptons and neutrinos. They evaluated the limits on these states through the decay of l^*l^*, $\nu^*\nu^*$ to various combination of leptons, neutrinos and Z/W boson, where Z/W decays to hadronic and leptonic modes. The L3 came up with a lower bound on mass of excited charged or neutral lepton to be 101.5 GeV [46]. From various searches at LEP experiments no evidence came in support of excited quark/lepton theory.

2.3.3 Limits from $p\bar{p}$ Collision at the Tevatron

At present the Tevatron at Fermi National Accelerator Laboratory(Fermilab) is the highest energy accelerator and collides beam of protons and anti-protons at $\sqrt{s}$ =1.96 TeV. It has two experiments that record the collision data and analyzes them.

Both the experiments the CDF and the DØ, have searched for excited quarks. These excited states are assumed to couple to the SM particles primarily through gauge couplings. Their most visible signature could be either pair production or single excited state production via quark-gluon fusion, provided the q^*qg coupling is sufficiently large. Enhanced dijet production rate with an invariant mass peak above the SM continuum is one of the prominent signals, extensively searched by both the experiments and the

DØ collaboration has excluded a mass range of 200-720 GeV [55]. Similarly, the CDF collaboration has excluded a mass range of 80-570 GeV [56, 57] for various final states. In a similar vein, the CDF collaboration has put a lower bound of $\Lambda \geq 2.81$ GeV at 95% CL using the $q\bar{q} \rightarrow e\nu$ prcoess[58] whereas the DØ collaboration ruled out $\Lambda \leq 2.0$ TeV at 95% CL from dijet mass peak searches for contact interaction scenario [59].

2.3.3.1 Current Experimental Limits on Λ and M_{q^*}

The latest experimental bound on Λ and M_{q^*} comes from the CDF and DØ experiments at Tevatron and these limits will improve as more data get analyzed.

- Limits from DØ Experiment: Recently the DØ experiment has analyzed the data for angular distribution measurements of the dijet production at $\sqrt{s}$ =1.96 TeV. The data corresponds to an integrated luminosity of 0.7 fb^{-1}. The two variables measured in dijet distributions are:

$$\chi_{dijet} = e^{(|y_1 - y_2|)} \tag{2.3}$$

$$y_{boost} = \frac{1}{2}|y_1 - y_2| \tag{2.4}$$

  where y_1 and y_2 are the rapidities of the two leading jets. These variables were measured in different dijet mass bins. In a $2 \rightarrow 2$ process the χ_{dijet} and the polar angle are directly related with the θ^*, the polar angle in the partonic center of mass frame, with the relation given in eq.(2.5). Hence the χ_{dijet} quantity directly probes the dynamics of the new interaction due to compositness.

$$\chi_{dijet} = \frac{1 + \cos\theta^*}{1 - \cos\theta^*} \tag{2.5}$$

For the limit evaluation both *Bayesian* and *Frequentist* method were employed in the analysis. From *Frequentist* method the lower limits at 95% CL were found to be 2.46(2.42)TeV for $+\lambda(-\lambda)$, where λ is the interference term between the SM and new physics. The expected limits within 1σ uncertainty were estimated to be $2.65^{+0.42}_{-0.35}(2.65^{+0.45}_{-0.39})$ TeV. Details of the analysis and method can be found in ref [60].

- Limits from CDF Experiment: The CDF collaboration has also searched for the composite quarks in two jet final state. The Lagrangian of the model considered in this analysis affects the SM QCD cross section by enhancing the cross section in the perpendicular direction of the dijet center of mass frame. The Lagrangian considered is of the from:

$$L = \pm \left(g^2/2\Lambda^2(\bar{q}_L\gamma_\mu q_L)(\bar{q}_L\gamma^\mu q_L) \right) \tag{2.6}$$

where the effect of new physics is sensitive to $(\hat{s}/\Lambda^2)^2$. CDF has used angular distribution as mentioned in eq.(2.3) for the probe of compositeness. The angular distribution was measured in four different dijet mass bins. It was required that the two leading jets must have E_T >100 GeV. The signal for such interaction would be enhancement of production rate in $1 < \chi_{dijet} < 10$ region for few order of TeV of Λ. Using Feldman and Cousins approach a limit of Λ >2.4 TeV at 95%CL [61] was obtained. In this case systematic uncertainties are found to dominate the obtained limits.

Since the Tevatron is expected to operate for the next couple of years, more stringent limits with reduced systematics are expected on compositeness scale and these will be complementary to the LHC results in the early phase of operation.

2.4 Sensitivity at the LHC

Although the Large Hadron Collider(LHC) is not yet operational, great efforts have been put by its two main experiments, ATLAS and CMS to evaluate the discovery potential with the early data set. Among the possible discoveries, searching for more fundamental building blocks of matter or quark compositeness is one of the scenario studied in great detail with complete detector simulation and systematic effects. We present some brief insights into these studies.

At the LHC both the ATLAS and the CMS collaboration have estimated the sensitivity for q^* search in the dijet production mode. To cancel many systematics, CMS has used the *dijet ratio* method for contact interaction as well as excited state study in the dijet final state [62]. The *dijet ratio* is defined as the ratio of number of events in the $|\eta| < 0.7$ to those in $0.7 < \eta < 1.3$. The main advantage of the *ratio* method is cancelation of many systematics (e.g., from luminosity error) which could be important in analysis of early data. Fig. 2.6 shows the comparison of SM QCD dijet production ratio with q^* resonance and contact interaction case (figure is from [62]). With full detector simulation CMS collaboration has estimated that at $\sqrt{s} = 14$ TeV, $\Lambda = 6.2$ TeV can be excluded at 95% CL with a luminosity of 100 pb^{-1}, and a 5σ sensitivity could be reached for Λ =8 TeV for 1 fb^{-1} of data [63]. The CMS experiment has also done a detailed study to probe contact interaction in Drell-Yan channel with dimuon final state. With the use of *double ratio* method to reduce systematic uncertainty, it has been shown that it would be possible to probe a scale of 15-20 TeV (including systematic effects) with an integrated luminosity of $\sim$10 fb^{-1}. A more detailed methodology of *double ratio* analysis has been presented in [64].

The ATLAS collaboration has shown that using dijet angular distribution the contact interaction(CI) effect can be probed upto Λ =10 TeV at $\sqrt{s} = 14$ TeV with an integrated luminosity of 700 pb^{-1}. The analysis uses the same variable for angular correlation as

mentioned in eq.(2.3). It was found that CI affects the large χ region and based on the analysis a cut of χ =2.7 was chosen as shown in Fig. 2.7. ATLAS has also studied other final states for search of excited quarks which includes $\gamma + jet$ resonances. The analysis estimates that excited quarks could be discovered with 5σ significance upto $M_{q^*} = 6.5$ TeV for standard coupling strengths i.e. $f = f' = f_s$=1 [65].

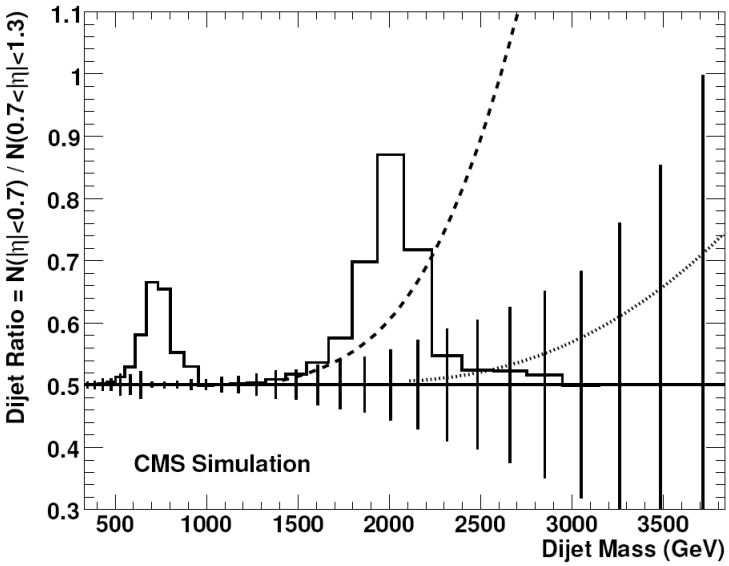

Figure 2.6 The dijet ratio for SM QCD production(horizontal line). The vertical bars indicated the statistical uncertainty. The QCD+Contact interaction signal is shown as dashed and dotted line for $\Lambda^+ = 5$ TeV and 10 TeV respectively. The distribution for QCD+resonance are plotted as solid black line for M_{q^*} =0.7 TeV and 2 TeV respectively.

Recently the possibility of top quark compositeness at LHC has been explored as enhanced rate of $pp \rightarrow t\bar{t}t\bar{t}$ production over the known SM production. The search strategy is to look for two same sign leptons and two hard jets, a signature which could reduce a large amount of combinatorial backgrounds. The deviation was estimated with variable H_T, defined as the scaler sum of P_T of all jets, leptons and missing E_T. In a conservative approach it has been estimated that a 5σ excess can be observed for a new state of mass upto 2 TeV [66].

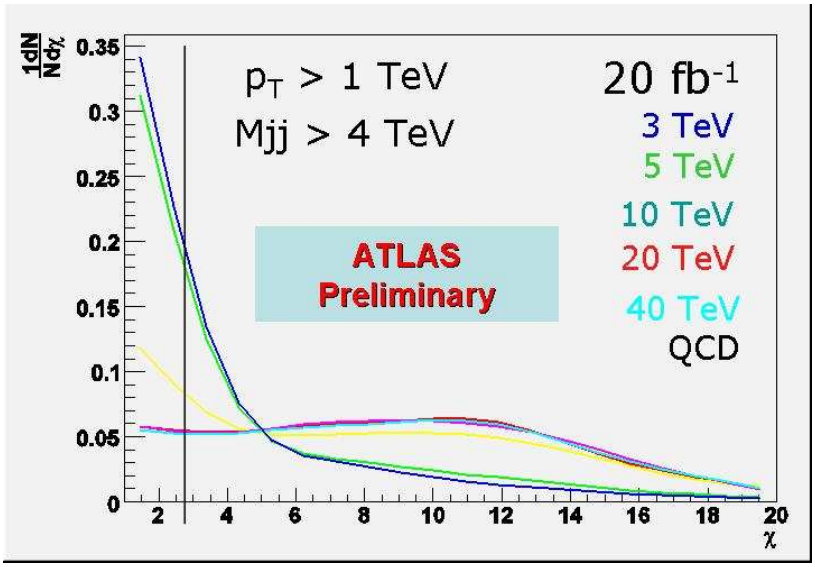

Figure 2.7 The shape of dijet angular distribution for SM QCD and for different compositeness scales in contact interactions scenario.

Besides detector simulation various phenomenological studies have also been done for excited state production. One such phenomenological study of flavor independent contact interactions analyzed the diphoton final state. The lower bound for compositeness scale $\Lambda_{\pm}$ has been estimated to be $\Lambda_{\pm} \geq 2.88$ TeV at 95% CL for 100 fb^{-1} of data [67]. These limits are based on the excess of events observed due to new physics over the SM background in the diphoton invariant mass spectrum.

2.5 Model Setup

With our interest lying not in the production of the excited states, but rather in their contribution to the photon plus single jet, and diphoton rates, and their kinematical distributions at a hadronic collider, we limit ourselves to examining only the relevant part of the *Lagrangian*, namely the magnetic transition between the SM states and the

excited states. In general, the Lagrangian is often parameterized by

$$\mathcal{L}_{int} = \frac{1}{2\,\Lambda}\bar{q^*_R}\,\sigma^{\mu\nu}\left[\sum_i g_i\; b_i\; T^a_i\; G^a_{i\,\mu\nu}\right] q_L + h.c., \tag{2.7}$$

where the index i runs over the three SM gauge groups, viz. $SU(3)$, $SU(2)$ and $U(1)$ and g_i, $G^a_{i\,\mu\nu}$ and T^a_i are the corresponding gauge couplings, field strength tensors and generators respectively. The dimensionless constants b_i are, *a priori*, unknown and are assumed to be of order unity. With these determining both the production rates and the branching into various modes, clearly, the phenomenology would depend considerably on their (relative) sizes. In the present work, we shall make the simplifying assumption that the excited states do not interact at all to the weak gauge bosons, but do so with the gluons and the photon. At first glance, this might seem incompatible with a $SU(2)\otimes U(1)$ invariant structure. However, complicated embedding could be the answer. More than this, since the assumption would not change the results qualitatively, it, at least, has the merit of reducing the number of possible couplings and hence simplifying the analysis. Note though that the coupling with $W^\pm$ can trivially be omitted by assuming that $b_2 = 0$ in eq.(2.7). This, though, would still leave a non-zero coupling with the Z. Similarly, postulating a different relation between b_1 and b_2 could eliminate the coupling with the Z while retaining that to the $W^\pm$. While complicated embedding could be the answer to eliminating all couplings with both $W^\pm$ and Z, in general this would involve the introduction of more states with masses of the order of or smaller than Λ. Note, though, that either of the choices above (or even any other $|b_2| \lesssim |b_1|$) would not materially influence our analysis. Clearly, the existence of a non-zero b_2 does not affect t-channel contributions. As for the s-channel one, the only influence of b_2 would be through the width of the q^*. However, even for comparable b_i, the width $\Gamma(q^*)$ is clearly dominated by the chromomagnetic moment (b_3) and even the inclusion of a nonzero b_2 would not cause a significant deviation in the branching fraction into $(q+\gamma)$. Thus, the assumption has,

at least, the merit of reducing the number of possible couplings and hence simplifying the analysis.

A further point needs to be noted here. With the Lagrangian of eq.(2.7) being a higher dimensional operator, the cross sections would typically grow with the center of mass energy, consequently violating unitarity. This is not unexpected in an effective theory as the term in eq.(2.7) is only the first term and the loss of unitarity, to a given order, is presumably cured once suitable higher dimensional operators are included in eq.(2.7). An equivalent way to achieve the same goal is to consider the b_i to be form factors rather than constants. To this end, we shall define the $q^*q\gamma$ and q^*qg vertices to be given by

$$\begin{aligned} \overline{q^*}\, q\, \gamma_\mu(p) : &\qquad \frac{e\, e_q\, f_1}{\Lambda}\, \left(1+\frac{Q^2}{\Lambda^2}\right)^{-n_1}\, \sigma_{\mu\nu}\, p^\nu \\ \overline{q^*}\, q\, g_\mu(p) : &\qquad \frac{g_s f_3}{\Lambda}\, \left(1+\frac{Q^2}{\Lambda^2}\right)^{-n_3}\, \sigma_{\mu\nu}\, p^\nu\, T_\alpha \end{aligned} \tag{2.8}$$

where Q denotes the relevant momentum transfer and $f_i \sim 1$ are dimensionless constants related to b_i of eq.(2.7). It can be checked that, for $Q^2 = s$, unitarity is restored as long as the constants $n_i \geq 1$. From now on, eq.(2.8) defines our theory[1]. For the rest of our analysis, we shall confine ourselves to a discussion of $n_i = 1$. While this might seem to be an optimistic choice, it is not quite so. In fact, the collider search limits in the literature actually correspond to $n_i = 0$ and, thus, our limits would be more conservative.

2.6 Excited Quark Production

If the hypothesis of q^* is true, it is possible, indeed probable, that excited quarks can exist at a mass scale comparable to the dynamics of new binding force. In the simplest phenomenological model, the excited fermions are assumed to have both spin and isospin 1/2. Since they interact with the SM particles, they could be produced (if they exist!)

[1]While a Lagrangian formulation leading to such vertices would necessitate a seemingly non-local Lagrangian, this is not unexpected in an effective theory.

in different channels in pp collsions. At the LHC center of mass energy, one may either pair produce the excited quarks, primarily through gauge couplings, or their production can happen singly via quark-gluon fusion, providing q^*qg coupling strength is significant. Among the processes which can have contribution from such couplings are $\gamma + jet$ and dijet production while the trilinear coupling of excited quarks to its SM counterparts and photon could also change the rate of diphoton production. A striking signal of the first would be an enhancement in the production rate with a peak in the invariant mass of $\gamma + jet$ and dijet channels while in the latter channel an excess of events over SM diphoton will happen. The fact that experiments have not shown any signature for dijet signal and also due to isolation requirements in the present analysis, we have neglected their presence in the dijet mode. Moreover dijet final state has been explored quite well at the Tevatron.

Among the possible scenarios the exited quark could be produced in the final state or as a virtual state (as a propagator in a Feynman diagram) in the collision. Here we have only concentrated on their virtual effects in $\gamma + jet$ and $\gamma\gamma$ production at the LHC.

2.6.1 Photon+Jet Production

The SM production of $\gamma + jet$ at the leading order(LO) happens by three subprocess, namely, quark-gluon scattering also called Compton scattering, quark-antiquark annihilation and gluon-gluon fusion. The quark-gluon scattering is the dominating contributor to the total $\gamma + jet$ production at the LHC. For the virtual effects of q^* on direct photon production, we have considered the first two production modes only. Any attempt to calculate the box contribution through q^* would make the effective theory non-renormalizable. Although by the inclusion of suitable higher dimensional operators one can survive but then the contribution would presumably be very small compared to Compton and annihilation diagram to have any meaningful effect on our analysis.

2.6.1.1 $qg \to \gamma + jet$ via $q*$

With the introduction of vertex as mentioned in eq.(2.8), the subprocess $qg \to q\gamma$ acquires a new contribution as portrayed in Fig. 2.8(b). Adding this diagram to pure QCD contribution, the ensuing differential cross sections reads as:

$$\begin{aligned}
\left.\frac{d\sigma}{d\hat{t}}\right|_{qg\to q\gamma} &= \frac{-\pi\,\alpha\,\alpha_s\,e_q^2}{3\,\hat{s}^2}\left[C_{sm} + 2\frac{f_1 f_3}{\Lambda^2}C_I + \frac{f_1^2 f_3^2}{\Lambda^4}C_Q\right] \\
C_{sm} &\equiv \frac{\hat{u}}{\hat{s}} + \frac{\hat{s}}{\hat{u}} \\
C_I &\equiv \frac{\hat{s}^2\,(\hat{s} - M_{q*}^2)\,\mathcal{F}_s}{(\hat{s} - M_{q*}^2)^2 + \Gamma^2 M_{q*}^2} + \frac{\hat{u}^2\,\mathcal{F}_u}{\hat{u} - M_{q*}^2} \\
C_Q &\equiv \left(\hat{s}\hat{u} + M_{q*}^2\hat{t}\right) \\
&\quad \left[\frac{\hat{s}^2\,\mathcal{F}_s^2}{(\hat{s} - M_{q*}^2)^2 + \Gamma^2 M_{q*}^2} + \frac{\hat{u}^2\,\mathcal{F}_u^2}{(\hat{u} - M_{q*}^2)^2}\right] \\
&+ 2M_{q*}^2\frac{\hat{s}\hat{t}\hat{u}}{\hat{u} - M_{q*}^2}\,\frac{(\hat{s} - M_{q*}^2)\,\mathcal{F}_s\,\mathcal{F}_u}{(\hat{s} - M_{q*}^2)^2 + \Gamma^2 M_{q*}^2} \\
\mathcal{F}_s &\equiv \left(1 + \hat{s}/\Lambda^2\right)^{-(n_1+n_3)} \\
\mathcal{F}_t &\equiv \left(1 - \hat{t}/\Lambda^2\right)^{-(n_1+n_3)} \\
\mathcal{F}_u &\equiv \left(1 - \hat{u}/\Lambda^2\right)^{-(n_1+n_3)}
\end{aligned} \tag{2.9}$$

Here the C_{sm} is the pure SM contribution, C_I is the interference term between the SM and new q^* physics while C_Q is purely new physics contribution.

The SM result will be recovered in the limit $\Lambda \to \infty$ which also implies that higher the compositeness scale Λ, it is harder to observe the signal for new physics due to much smaller contribution. Since $q^* \to \gamma + jet$ is a s-channel resonance contribution, a mass peak at M_{q^*} is expected over the SM continuum production in the invariant mass of final state particles, γ and jet. The new physics contribution to the differential cross

section thus depends on four parameters, namely f_1, f_3, Λ and the mass of the excited state M_{q^*}. For simplicity, we assume these to be flavor-independent (within a generation, it obviously has to be so). For eq.(2.7) to make sense as an effective *Lagrangian*, the masses have to be less than Λ (Ref.[68] requires that $M_{q^*} < \Lambda/\sqrt{2}$). Note that as long as $\Lambda \gg \hat{s}$, one of $f_{1,3}$ can always be absorbed in Λ. In our analysis, we have considered only moderate values for these parameters. The mandalstam variables $\hat{s}$, $\hat{t}$ and $\hat{u}$ used in

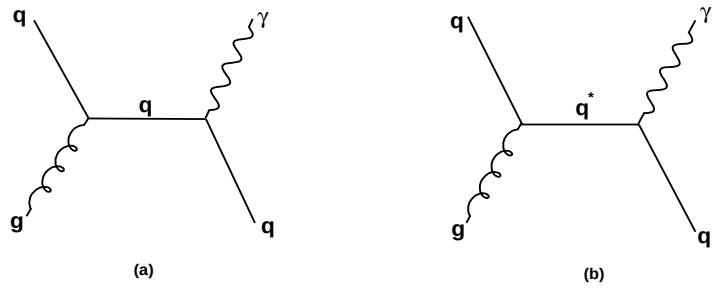

Figure 2.8 s-channel $\gamma + jet$ production through (a) SM (b) via q^* mediation(resonance production).

eq.(2.9) and the cross section based on parton model has been described in Appendix-A and B respectively.

2.6.1.2 $q\bar{q} \rightarrow \gamma + jet$ via $q*$

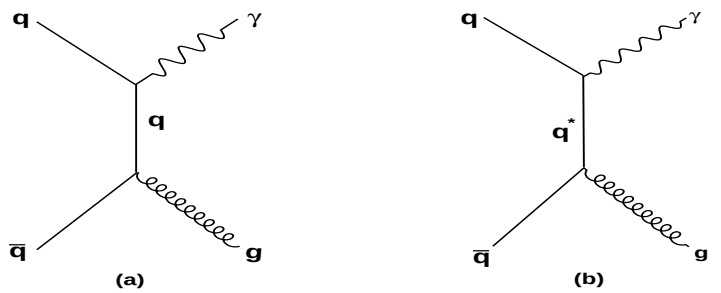

Figure 2.9 t-channel quark-antiquark annihilation for $\gamma + jet$ production through (a) SM (b) via q^*.

For $q\bar{q} \to g\gamma$ via q^*, the Feynman diagrams are shown in Fig. 2.9 and the differential cross-section are related to those in eq.(2.9) by crossing symmetry and are given by

$$\begin{aligned}
\left.\frac{d\sigma}{d\hat{t}}\right|_{q\bar{q}\to g\gamma} &= \frac{8\pi\,\alpha\,\alpha_s\,e_q^2}{9\,\hat{s}^2}\left[B_{sm} - 2\frac{f_1 f_3}{\Lambda^2}B_I + \frac{f_1^2 f_3^2}{\Lambda^4}B_Q\right] \\
B_{sm} &\equiv \frac{\hat{u}}{\hat{t}} + \frac{\hat{t}}{\hat{u}} \\
B_I &\equiv \frac{\hat{t}^2\,\mathcal{F}_t}{\hat{t} - M_{q*}^2} + \frac{\hat{u}^2\,\mathcal{F}_u}{\hat{u} - M_{q*}^2} \\
B_Q &\equiv \hat{t}\hat{u}\left[\frac{\hat{t}^2\,\mathcal{F}_t^2}{(\hat{t} - M_{q*}^2)^2} + \frac{\hat{u}^2\mathcal{F}_u^2}{(\hat{u} - M_{q*}^2)^2}\right] \\
&+ M_{q*}^2\,\hat{s}\left[\frac{\hat{t}\,\mathcal{F}_t}{\hat{t} - M_{q*}^2} + \frac{\hat{u}\,\mathcal{F}_u}{\hat{u} - M_{q*}^2}\right]^2
\end{aligned} \tag{2.10}$$

It should be noted that while eq.(2.7) represents the lowest order terms in an effective Lagrangian connecting q^* and q, we could, indeed, have written higher order (contact) terms such as $(\bar{q}\Gamma_i q)\,(\bar{q}\Gamma_i q^*)$ or $(\bar{q}\Gamma_i q)\,(\bar{q}^*\Gamma_i q^*)$, where Γ_i represent combinations of Dirac matrices. Both of these are $\mathcal{O}(\Lambda^{-2})$, and hence we would be justified in neglecting them in an effective theory treatment. The second of these terms would contribute to q^*-pair production. Apart from being kinematically suppressed, this can lead to a contribution to the signal under consideration only if two of the daughter entities from the q^*-decays are rendered invisible either by virtue of being outside of the detector acceptance parameters or as a result of merging. The resultant contribution is too small to be of any concern and, in fact, even the much larger QCD contribution to q^*-pair creation resulting from the gauge interaction of the q^*'s is very small for the sensitivity limits that we would turn out to reach. As for the $(\bar{q}\Gamma_i q)\,(\bar{q}\Gamma_i q^*)$ terms, once again the contribution to $q^* + q/g$ production is only $\mathcal{O}(\Lambda^{-4})$ and hence much smaller than the leading terms of eq.(2.9 & 2.10). Additionally, the need to lose a jet further suppresses the rates. And while such terms would also contribute to $\Gamma(q^*)$, the corresponding partial width would be

suppressed by a factor $\sim M_{q^*}^2/(4\pi\Lambda^2)$ or smaller compared to those of eq.(2.12).

2.6.2 Diphoton Production

The diphoton production in the presence of virtual production of q^* is the coherent addition of the two diagrams shown in Fig. 2.10. The differential cross-section is given as:

$$\begin{aligned}
\frac{d\sigma}{d\hat{t}} &= \frac{\pi\,\alpha^2}{3\,\hat{s}^2}\left[e_q^4\left(\frac{\hat{u}}{\hat{t}}+\frac{\hat{t}}{\hat{u}}\right)-\frac{2\,e_q^2}{\Omega^2}\left(\frac{\hat{t}^2}{\hat{T}}+\frac{\hat{u}^2}{\hat{U}}\right)\right. \\
&+ \left.\frac{1}{\Omega^4}\left\{\hat{t}\,\hat{u}\left(\frac{\hat{t}^2}{\hat{T}^2}+\frac{\hat{u}^2}{\hat{U}^2}\right)+M_{q^*}^2\,\hat{s}\left(\frac{\hat{t}}{\hat{T}}+\frac{\hat{u}}{\hat{U}}\right)^2\right\}\right] \\
\Omega &\equiv \Lambda\left(1+\frac{\hat{s}}{\Lambda^2}\right)^n \\
\hat{T} &\equiv \hat{t}-M_{q^*}^2 \qquad\qquad \hat{U}\equiv\hat{u}-M_{q^*}^2
\end{aligned} \tag{2.11}$$

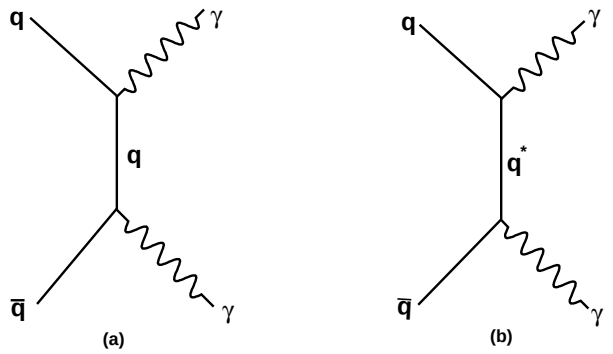

Figure 2.10 Diphoton final state production through quark-antiquark annihilation for (a) SM and (b) via excited quark q^*.

In Fig. 2.11, we present the additional contribution to the total diphoton cross section accruing from the new physics terms in eq.(2.11). Note that, unlike the QED contribution, this additional contribution does not suffer from collinear singularities. Contrary

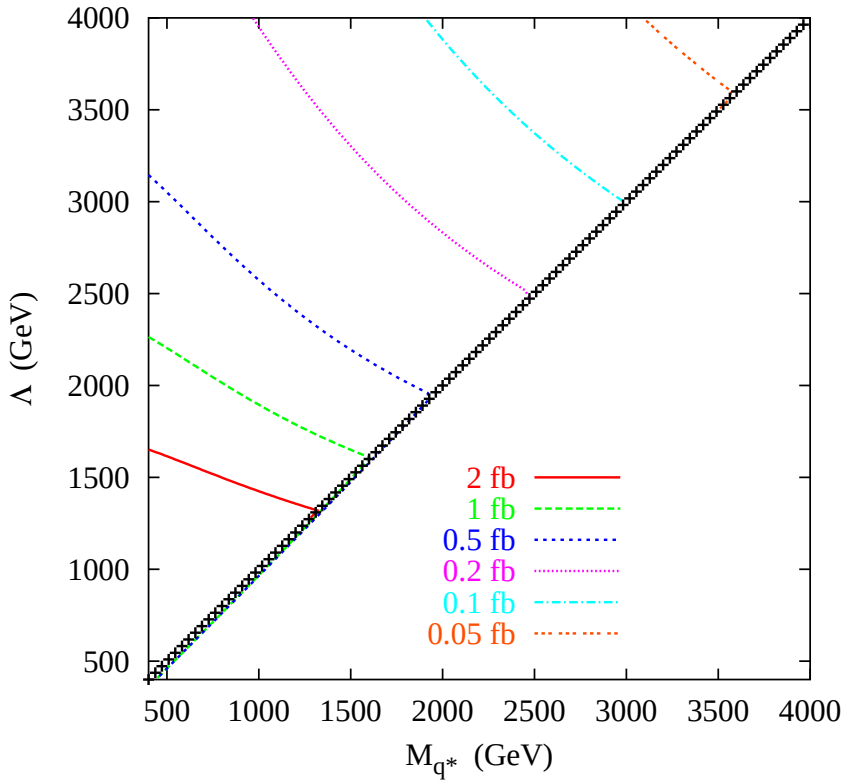

Figure 2.11 The contribution of new physics to the total SM production cross section of diphoton (evaluated at Matrix Element level).

to the case of actual production (and subsequent decay) of the excited state, the case under consideration is not associated with any resonant peak, but the presence of the new contribution preferentially enriches the large invariant mass end of the diphoton spectrum. The exchange of a large mass particle in the t– and u–channels naturally enhances the high-P_T photon sample. To improve the signal to noise ratio, we must then concentrate on such a phase-space restricted subset of the final state. As can be gleaned from a cursory examination of eq.(2.11), the aforementioned dependence of the new contribution on the photon P_T is not as extreme as that for the QED contribution. Thus, the imposition of such cuts as we discuss later, would not drastically change the shape of the iso-cross section contours as depicted in Fig. 2.11. Consequently, the exclusion contours that we have finally obtained bear considerable similarity with those in Fig. 2.11.

2.7 Width(Γ) of Excited Quark Resonance

In $\gamma + jet$ search mode one of the important factor is the width of s-channel resonances which can have a significant impact on the final results. With the aforementioned Lagrangian, the width of the q^* for $qg \to \gamma + jet$ is expressed as:

$$\begin{aligned} \Gamma(q^*) &= \Gamma_{q+g} + \Gamma_{q+\gamma} \\ \Gamma_{q+g} &= \frac{2\alpha_s f_3^2}{3}\,\Gamma_0 \\ \Gamma_{q+\gamma} &= \frac{e_q^2 \alpha_{em} f_1^2}{2}\,\Gamma_0 \\ \Gamma_0 &\equiv \frac{M_{q*}^3}{\Lambda^2}\left(1 - \frac{4m_q^2}{M_{q*}^2}\right)\left(1 - \frac{m_q^2}{M_{q*}^2}\right)^2 \end{aligned} \tag{2.12}$$

and can be very large for a heavy q^*. Since a wide resonance is often difficult to observe, this will turn out to have profound consequences. In Table 2.1 we show the widths for these exited states for different M_{q^*}. As can be seen that for higher masses the widths are large and their convolution with detector effects can make them even broaden. It should also be noted that total width receives dominant contribution from Γ_{q+g} as shown in Table 2.2.

2.8 Backgrounds

Various SM backgrounds which are relevant for these two($q^* \to \gamma + jet$ and $q^* \to \gamma\gamma$) analysis can be be summarized as follows:

- **For $\gamma + jet$ Search Mode**: SM QCD dijet, SM $\gamma + jet$, and $Z/W(\to jj) + \gamma$ production.

- **For $\gamma\gamma$ Search Mode**: SM QCD dijet, SM $\gamma + jet$ and SM $\gamma\gamma$ production

M_{q^*} (TeV)	$\Gamma(q^*)$ (GeV)	
	$f_1 = f_3 = 1.0$	$f_1 = f_3 = 0.5$
0.5	34.4	8.61
1.0	63.6	15.9
2.0	118	29.6
3.0	170	42.6
4.0	221	55.2
5.0	271	67.6
6.0	319	79.8

Table 2.1 $\Gamma(q^*)$ as a function of $M_{q^*}(=\Lambda)$ for different coupling strengths. Both α_s and α_{em} are evaluated at M_{q^*}.

SM QCD dijet: Among the backgrounds listed above, the QCD dijet production is the common background for both the channels. For higher transverse momentum, the total cross section is $\sim 10^4$ times larger than the SM $\gamma + jet$ production. This is because dijet production is enhanced by the order of the ratio of $\mathcal{O}(\alpha_s/\alpha)$ compared to $\gamma + jet$ production. The sub-processes which contributes to QCD dijet are $qg \to qg$, $q\bar{q} \to q\bar{q}$ and $gg \to gg$. The next-to-leading order(NLO) correction of the order $\mathcal{O}(\alpha_s)$ to these diagrams produces the LO contributions of the fragmentation type. These are also known as "bremsstrahlung contributions", where one photon comes out from the quark in the process of collinear fragmentation. The relevant diagrams are shown in Fig. 2.12. Similar contribution also arises from initial state radiation where photon can be radiated from incoming quark lines. As these photon do not emerge from the interaction vertex and have collinear quark which manifests as jets, these are easily removed with isolation requirements.

The other background to $\gamma + jet$(diphoton) comes mainly from the process when one(both) of the jet(s) in final state fragments into a highly energetic neutral meson which carries a large fraction of the parent parton's energy and then decays to photon

M_{q^*}	$\Gamma(q^*)$ (GeV) for f_i =1	
(TeV)	$\Gamma_{q+\gamma}$	Γ_{q+g}
0.5	0.88	33.5
1.0	1.8	61.8
2.0	3.6	114.7
3.0	5.4	165.0
4.0	7.2	213.8
5.0	9.0	261.5
6.0	10.9	308.2

Table 2.2 $\Gamma_{q+\gamma}$ and Γ_{q+g} as a function of $M_{q^*}(=\Lambda)$

.

final state. Figure 2.13 illustrates this contribution. These processes are described as $2 \rightarrow 2$ hard scattering convoluted with the fragmentation functions $D_{\gamma/q}(z_\gamma, \mu_f)$ and $D_{\gamma/g}(z_\gamma, \mu_f)$. These fragmentation functions gives the probability that a parton q/g will produce final state particle γ with momentum fraction z_γ during the fragmentation process. The μ_f is known as the fragmentation scale. When these scales are large compared to ∼1 GeV, these functions behave as $\alpha/\alpha_s(\mu_f)$, so that these contributions are of the same order as the *direct photon*. During fragmentation the most commonly produced particle is a neutral mesons called π^0. The π^0, has a branching fraction of ∼99 % for the decay to two photons. The two photons produced are mostly collinear and in detector they appear as a single electromagnetic cluster thus mimicking a fake photon. Table 2.3 shows some of the neutral mesons which could be produced in jet and then can further decay to photon final states hence contributing to electromagnetic fraction of a jet. Since these particles are produced via strong interaction, they are copiously produced at hadron colliders. Although only a small fraction $\sim 10^{-3} - 10^{-4}$ of partons fragments in this way, since the dijet cross-section is $\sim 10^3 - 10^4$ times larger than direct photon production, the background contribution is of the same order as direct photon production. The experimental challenges and solutions involved in removing

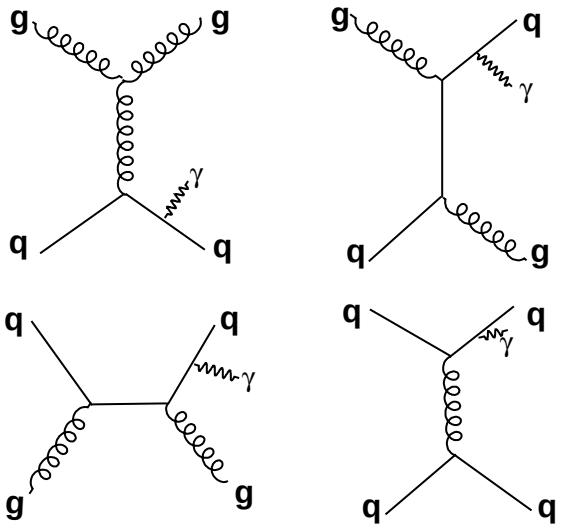

Figure 2.12 Bremsstrahlung contribution of QCD dijet production.

this background is a major part of any direct photon analysis. Apart from isolation

Particles	Mass (GeV/c^2)	Decay Products	Branching Ratio
π^0	0.135	$\gamma\gamma$	0.99
η	0.547	$\gamma\gamma$	0.39
η	0.547	$3\pi^0$	0.32
η	0.547	$\pi^0\pi^-\pi^+$	0.23
K_s^0	0.494	$2\pi^0$	0.31
ω	0.781	$\pi^0\gamma$	0.09

Table 2.3 Neutral mesons decay to various photon states which can mimic as hard photon in a detector.

requirements, the QCD dijet cross-section falls very rapidly($\sim P_T^{-4}$) with increasing P_T of the jets thus providing an additional means to suppress this background specially for the study of large transverse momentum photons and jets.

For $q^* \rightarrow \gamma\gamma$ study we have not taken into account the background due to QCD dijet because isolation requirement on both photon reduces this drastically. Moreover to

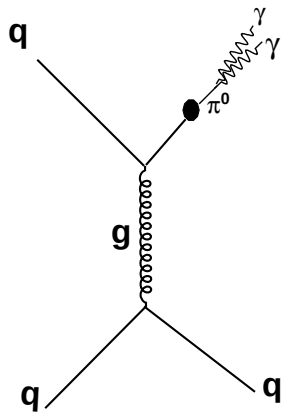

Figure 2.13 EM enriched jets as a background for direct photon signal.

study this small background precisely large statistics sample generation is needed which was not possible with the available resources. Though in the end we have estimated its contribution quantitatively.

SM $\gamma + jet$: The SM production of $\gamma+jet$ is given by three subprocesses $qg \rightarrow \gamma+jet$ (Fig. 2.8(a)), $q\bar{q} \rightarrow \gamma + jet$(Fig. 2.9(a)) and gluon-gluon scattering $gg \rightarrow \gamma + jet$ shown in Fig. 2.14(a). For high P_T^{γ}(e.g. $\geq 100GeV$) production quark-gluon scattering is the most dominating process at the LHC. Although $q\bar{q} \rightarrow \gamma+jet$ is subdominant contributor compared to Compton scattering its fraction increases for higher P_T^{γ}. The gluon-gluon fusion constitutes a very small fraction of the total cross section of $\gamma + jet$ production. These subprocesses constitute an irreducible background for the $\gamma + jet$ signal in q^* search. In case of $\gamma\gamma$ final state analysis these are the potential background where the jet fragmentation could reduce the signal significance.

SM $\gamma\gamma$: For $\gamma\gamma$ production via q^* signal, the irreducible background comes from the Born-level process $q\bar{q} \rightarrow \gamma\gamma$ (shown in Fig. 2.10). The additional contribution comes from the box diagram as shown in Fig. 2.14(b). Being an $\mathcal{O}(\alpha^2\alpha_s^2)$ order process, the

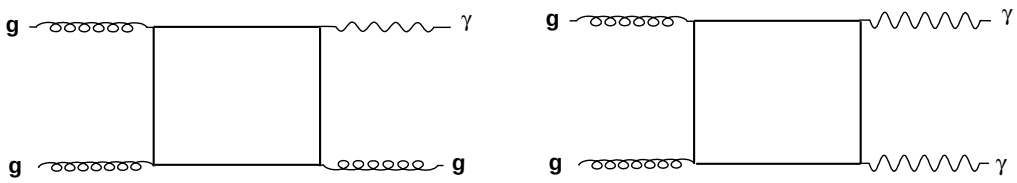

Figure 2.14 Box diagram for (a)$\gamma + jet$ and (b)$\gamma\gamma$ production.

cross section for the box diagram is relatively small compared to the Born production. Moreover with tighter phase space restriction the cross-section reduces drastically. Despite these facts since the gg luminosity at the LHC will be very large due to small x reach (i.e. high Q^2 transfer) of the machine and hence the $gg \rightarrow \gamma\gamma$ could be quite important.

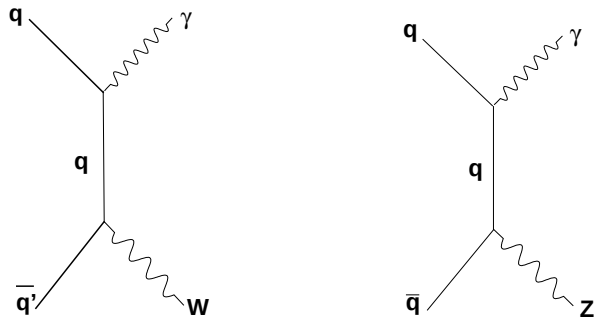

Figure 2.15 SM $\gamma + W/Z(\rightarrow jj)$ production.

SM $q\bar{q} \rightarrow W/Z + \gamma$**:** The SM $q\bar{q} \rightarrow \gamma + W/Z$ is the other final state which can mimic $\gamma + jet$ and diphoton signal of q^*. The W and Z could decay to two jets and if the longitudinal boost is large enough, these two jets could merge thus giving one photon and one jet. The other scenario could be that one of the jets is lost in detector cracks or does not have enough energy to pass the offline threshold for jet reconstruction.

Although these backgrounds are very small compared to QCD jets, Compton scattering, and annihilation diagram for direct photon production but for the P_T^{γ} range considered in this study they are comparable to $gg \rightarrow \gamma g$ background. For the purpose of completeness we have accounted these backgrounds for $q^* \rightarrow \gamma + jet$ study. The relevant Feynman diagrams are shown in Fig. 2.15.

For diphoton analysis we have not considered this($W/Z + \gamma$) background because of a jet faking photon probability of $\sim 10^{-3} - 10^{-4}$ and the stringent isolation requirements reduce this contribution to a negligible level. In other words their inclusion would not change the result quantitatively.

Chapter 3

The LHC Machine and the CMS Experiment

"The science of today is the technology of tomorrow."

- Edward Teller.

3.1 The Large Hadron Collider

The Large Hadron Collider(LHC) machine of the European Organization for Nuclear Research(CERN) located on the Swiss-French border near Geneva, Switzerland is the world's most powerful proton proton collider. It will be soon colliding subatomic particles nearly at the speed of light to create miniature Big Bangs. The energy created in these collisions will be sufficient to produce the elusive Higgs boson (also known as *God Particle* [69]), miniature black holes and many other new phenomena which are possible at high momentum transfer. The LHC is built in the 27 km tunnel where the Large Electron Positron(LEP) collider was situated and will start operation in late 2009. The LHC will take advantage of the existing accelerator complex at CERN to create the proton beams and accelerate them. At its full operational capacity(expected sometimes

in 2012), the collider will have two counter-rotating proton beams each with an energy of 7 TeV thus giving a total collision energy of 14 TeV in the center of mass frame. In its intial phase of operation, as planned now, the LHC will collide protons at a center of mass energy of 7 TeV, or a beam energy of 3.5 TeV/beam. In this chapter we present a brief discussion of design, technical parameters and goals of the LHC machine and the CMS experiment.

The LHC is a natural choice as the next step in particle physics. Historically discoveries of new particles have been dominated by hadron colliders extending the accessible energy range upwards. In this way the LHC can be seen as a discovery machine with a dynamic range of discovery from energy scales of few hundred MeV in case of B-physics to a few TeV for the discovery of new vector bosons or composite quarks.

Figure 3.1 shows the schematic layout of the LHC ring within the CERN accelerator complex along with major experiments. The LHC ring is inclined at 1.14% with respect to the horizontal plane which gives a difference of 120 m across the tunnel diameter. The LHC ring is divided into eight arcs and eight straight sectors. The straight sectors are $\sim$528 m long and can serve as experimental insertions called insertion regions(IR). The whole LHC ring has been categorized in different insertion points from Point-1 to Point-8. The two high luminosity insertion points, Point-1 and Point-5, are located in opposite sectors to each other while the beam dump insertion is located at Point-6 where the two beams are vertically extracted using the "kicker" magnets and double steel septum magnets. The kicker magnets deflect the beam horizontally towards the septum magnets which further deflect the beam in vertical direction towards absorbers in a different tunnel. For beam dump each system has an independent abort system.

To achieve higher luminosity and keeping in view the physics goals at the TeV scale, two proton beams instead of proton-antiproton beams(as in the case of Tevatron), are used. Prior to being injected into the main accelerator, the particles are prepared by a series of systems that successively increase their energy. The first system is the lin-

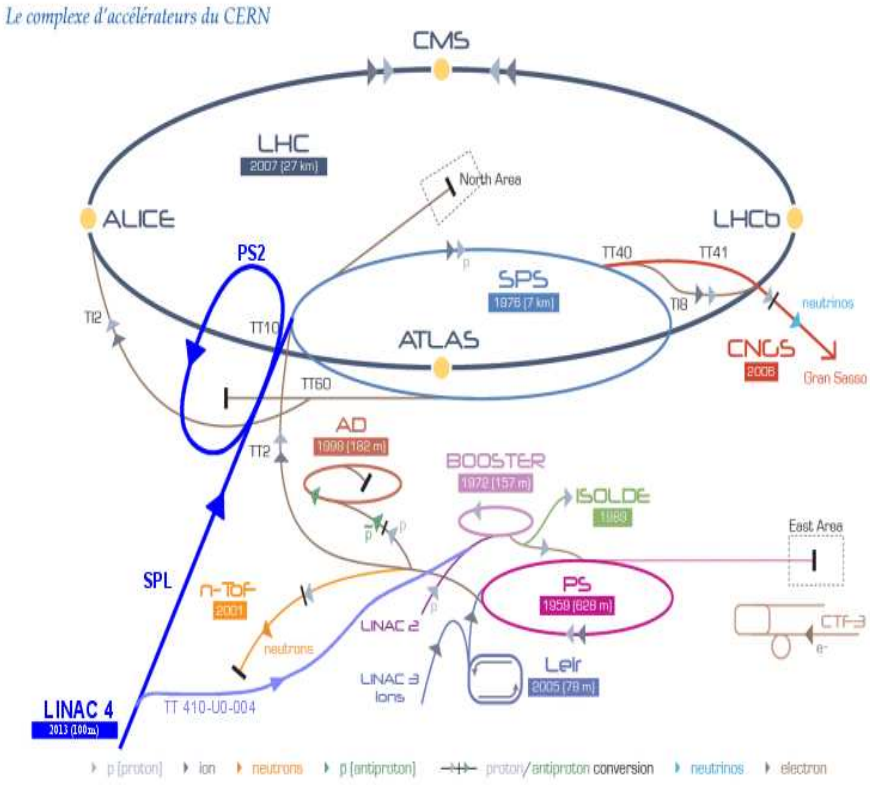

Figure 3.1 Layout of the LHC ring within the CERN accelerator complex.

ear particle accelerator LINAC2 generating 50 MeV protons, which feeds the Proton Synchrotron Booster (PSB). There the protons are accelerated to 1.4 GeV and injected into the Proton Synchrotron (PS), where they are accelerated upto 26 GeV. Finally the Super Proton Synchrotron (SPS) is used to further increase their energy to 450 GeV before they are injected(over a period of 20 minutes) into the main LHC ring. Here the proton bunches will be accumulated, accelerated (over a period of 20 minutes) to 7 TeV energy, and finally circulated for hours while collisions occur at the four intersection points(Point-1,2,5 and 8). Filling of LHC ring requires about 12 cycles of the SPS synchrotron and each SPS fill requires about 3-4 cycles of PS synchrotron. For storing and accelerating the beam, a superconducting radio frequency(RF) cavity system of 400 MHz with a revolution frequency of 11.245 kHz will be used. Two independent RF systems

will be used for efficient use and independent control of both the beams. To achieve this, the standard beam separation will be increased from 194 mm to 420 mm with the help of special superconducting dipoles but passing through the same cryostat. During injection, the error on the transverse direction are damped by the use of electrostatic deflectors.

To attain the design luminosity of $10^{34} cm^{-2} s^{-1}$, each proton beam will circulate 2808 bunches with $\sim 1.15 \times 10^{11}$ protons/bunch in the beam pipe. The proton bunches will cross each other every 25 ns which will be the collision frequency(40 MHz). Since protons are circulated in both the directions it excluded the possibility of a common vacuum and magnet system for both circulating beams unlike the case of Tevatron. The LHC was therefore designed with different magnetic fields and vacuum for the two beams in the main arc, and common sections in the insertion regions(IR) where the experimental detectors are located. For about 130 m of the IR, both beams share a common beam pipe.

The LHC accelerator performance depends on the superconducting magnets. These magnets are based on $NbTi$ Rutherford cables windings. The performance of the LHC's beam-guiding magnets is ensured by their operation in a superconductive state which can only be reached if the system is maintained at a very low temperature. Therefore the LHC requires the largest cryogenic infrastructure ever created. The temperature at the time of operation of LHC will be 1.9^oK (or -271.1^oC), a temperature lower than that of interstellar space. A total of 1232 superconducting dipole magnets having a magnetic field of 8.3 Tesla and kept at a temperature of 1.9^oK (to attain such high magnetic field) will be used to bend the proton beams. About 400 quadruple magnets will ensure that the beams are kept focussed and on the track. This means that they will control the beam's micrometer(μm) dimension all the way along their trajectory in the ring. These magnets are inserted in enclosures of liquid helium along with corrector magnets as well as other components. Some of the machine and beam parameters are shown in Table 3.1.

Beam parameters		
Beam Energy	(TeV)	7
Luminosity	$(cm^{-2}s^{-1})$	10^{34}
Time between collisions	(ns)	25
Bunch length	(cm)	7.7
Beam radius at interaction point	(μm)	15.9
Machine parameters		
Ring circumference	(m)	26658.9
RF frequency	(MHz)	400.8
Number of bunches		2808
Number of bending dipoles		1232
Magnetic length of the bending dipoles	(m)	14.2
Field of the bending dipoles	(T)	8.3
Bending radius	(m)	2784
Temperature of the main magnets	(^{o}K)	1.9

Table 3.1 Few important LHC parameters.

The LHC will also be used to collide heavy ions with heavy ions(as well with protons) with a collision energy of 1.15 PeV. The Pb ions will be first accelerated by the linear accelerator LINAC3, and the Low-Energy Ion Ring (LEIR) will be used as an ion storage and cooler unit. The ions will be further accelerated by the PS and SPS before being injected into LHC ring, where they will reach an energy of 2.76 TeV per nucleon.

3.2 Luminosity

One of the most important parameters of the LHC or any such other accelerator is its capability at which it can produce the expected or any new phenomena. This parameter is called the *luminosity* (L) and characterizes the number of collisions in a collider. Mathematically luminosity can be expressed as:

$$L = \frac{f N_1 N_2 n_b \gamma_r F(\theta)}{4\pi\epsilon_n \beta^*} \tag{3.1}$$

where,

- f is the frequency of interaction of the proton beams with each other. For LHC the collision frequency is $f = 40$ MHz.
- $N_{1,2}$ are the number of particles per bunch in two colliding beams.
- n_b is the number of bunches per beam.
- γ_r is the relativistic gamma factor.
- ϵ_n is the normalized transverse beam emittance.
- β^* is the beta function at the collision point.
- $F(\theta)$ is the factor accounting for reduction in luminosity due to the crossing angle $\theta = 285$ μrad of the two beam in the circular ring. The factor $F(\theta)$ depends on the length of the bunch and it is about 85% for the LHC machine.

The collision frequency of 40 MHz corresponds to a bunch separation of 7.5 m in the LHC ring. The transverse dimension(known as emittance) of the beam is another parameter which can affect the luminosity. The RMS beam size at the interaction point is about 16.7 μm(with a β function of 0.55) while for collision the normalized transverse emittance is 3.75 μm. To achieve higher luminosity, a simple way is to increase the number of protons in each bunch. But this is limited by electromagnetic forces between the colliding bunches. Although the maximum luminosity achievable will be close to 2 $\times 10^{34}$ $cm^{-2}s^{-1}$, at this point to be in a stable region the nominal luminosity is fixed at $10^{34} cm^{-2}s^{-1}$. For the early phase of LHC operation it is foreseen to operate at lower luminosity $L_{low} \approx 10^{32} - 10^{33} cm^{-2}s^{-1}$ and only gradually increases to the design luminosity of $L_{high} \approx 10^{34} cm^{-2}s^{-1}$. The number of observed events (n_{obs}) for any physics

process and L are related as,

$$n_{obs} = \sigma.BR.\varepsilon.\int L.dt \tag{3.2}$$

where σ is the cross-section for a particular physics channel, BR is the branching ratio for the selected decay mode, ε is the detection efficiency, and $\int L.dt$ is the integrated luminosity. The requirement of having high luminosity is one of the reasons for the choice of a proton-proton collider. While a proton-antiproton collider has the advantage that both counter-rotating beams can be kept in the same beam pipe, producing enormous amounts of antiprotons required for the high luminosity is not realistic and would be more expensive than the proton-proton solution with separate beam pipes. This also gets support from the fact that at 10-14 TeV center of mass energy, most of the interesting events will be produced by gluon fusion and at these energy gluons have a similar PDF for a proton or an antiproton. The charge asymmetry introduced with a proton-proton collider is not a serious problem for the physics analysis. The two proton beams circulate in separate magnetic chambers. The chosen solution is a "twin bore" magnet where the two beam channels are within the same mechanical structure and cryostat but sees magnetic flux in opposite directions. This structure is more compact and more economical than two separate magnets.

3.3 Experiments at the LHC

At the LHC accelerator, the proton and heavy ions beams will collide with each other at four different collision points around the ring. These collision points are covered by four main detectors namely: **A T**oroidal **L**HC **A**pparatu**S** (**ATLAS**), **C**ompact **M**uon **S**olenoid (**CMS**), **A L**arge **I**on **C**ollider **E**xperiment (**ALICE**) and **LHCb**. The ATLAS and the CMS are multipurpose detectors and their main physics goals are: to

test the SM with very high precision; search for the origin of mass or discover the Higgs boson(s); search for super symmetric particles to reveal the nature of dark matter candidates; understand the nature of space-time by searching for extra dimensions, black holes etc; and to figure out the nature of Big-Bang nucleosynthesis or primordial plasma by investigating quark-gluon plasma state. The ALICE is a dedicated experiment for heavy ion collision and its main goal is to study the properties of quark-gluon plasma which existed in very early universe. The designed peak luminosity at ALICE will be $10^{27} cm^{-2} s^{-1}$. The LHCb will explore the matter-antimatter asymmetry by studying CP-violation in B-physics sector and aiming at a peak luminosity of $10^{32} cm^{-2} s^{-1}$. There are two other smaller experiments namely **TOT**al **E**lastic and diffractive cross section **M**easurement (**TOTEM**) and **L**arge **H**adron **C**ollider **f**orward (**LHCf**). The TOTEM experiment aims to study the protons from elastic scattering at small angels and will monitor the LHC luminosity. It is located at the same collision point as CMS. LHCf is dedicated for measurement of neutral particles emitted in very forward regions and will provide data for calibration of hadron interaction models. These models are used in very high energy cosmic ray experiments.

3.4 Compact Muon Solenoid(CMS) Detector

The CMS detector has been designed to exploit the full range of physics at the LHC upto the designed luminosity for a long period of operation. The CMS is one of the most complex detectors ever build. It is cylindrical in shape and has a diameter of 14.6 m and is 21.6 m long. The detector weighs about 12,500 tons and is one of the heaviest particle physics detectors ever built.

The CMS detector is made up of the following main sub-detectors as one moves out from the center of the detector: the tracker, the electromagnetic calorimeter (ECAL), the hadron calorimeter (HCAL), a solenoidal magnet and the muon chambers. The

solenoidal magnetic coil is 13 m long and has an inner diameter of ∼6 m that easily accommodates the inner tracker and calorimeters, thus giving very compact design(hence the name "Compact Muon"). To achieve a good momentum resolution with a compact design and without making a stringent demand on muon chambers, a high magnetic field of 3.8 Tesla was chosen to bend the charged particles. A schematic layout of the CMS detector along with main sub-detector systems is shown in Fig. 3.2. The main

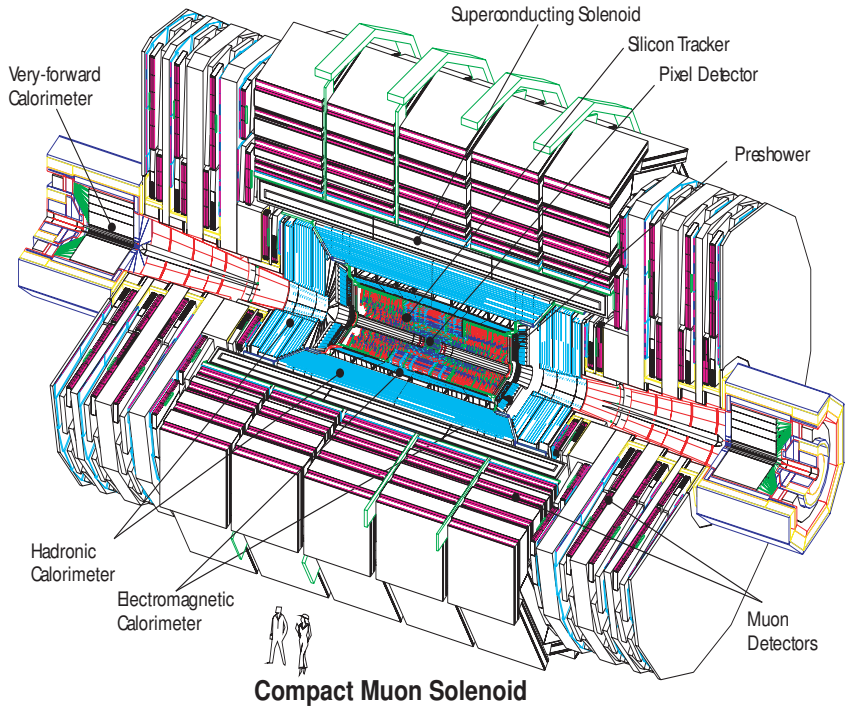

Figure 3.2 A schematic view of the CMS detector along with its all major subdetector systems.

characteristics of CMS detector are:

- A high quality tracking system with excellent charged particle momentum resolution and reconstruction efficiency.

- An excellent electromagnetic calorimeter having a wide coverage of $|\eta|$ <3.0, with $\sim$ 1%(at 100 GeV) mass resolution for diphoton and dielectron system. It has

excellent photon and electron isolation with efficient π^0 rejection.

- Good measurement of missing-transverse energy due to hermitic coverage of the detector.

- A high performance muon system for muon identification and momentum resolution($\sim$ 1% at 100 GeV) over a wide range of energy scale and angles.

- Efficient triggering and offline tagging of τ's and $b-$jets due to presence of pixel detector close to the interaction vertex.

3.4.1 The Tracker

The CMS tracking system consists of three main sub-detectors namely, the silicon pixels detector, silicon microstrip detector and Micro Strip Gas Chamber(MSGC). The tracking system and its different layers are shown schematically in Fig. 3.3.

The silicon pixel detector, the innermost tracking device, provides precise track origin by weighting the position of activated pixels, with respect to the magnitude of ionization caused by passing of a charge particle. There are three concentric layers in the barrel situated at distances of 4.3 cm, 7.2 cm and 11.0 cm respectively from the collision point while the endcaps have two discs on both sides at a distance of 32.5 cm and 46.5 cm from the interaction point. Together they cover in pseudorapidity upto $\sim$2.5. The pixel detector has a three dimensional spatial resolution of 10 μm in the $r-\varphi$ plane and 20 μm in the z-direction. There are a total of $\sim$66 million channels in silicon pixel detectors. All pixels have similar dimensions of 150 μm(length) $\times$ 100 μm(width) $\times$ 250 μm(depth) [70]. Here the length points along the z-direction in barrel and in ϕ direction for the endcap disks. Each of the four disks in endcap includes 24 wedge-shaped blades and are arranged in a turbine geometry. This is done by rotating the blades by an angle

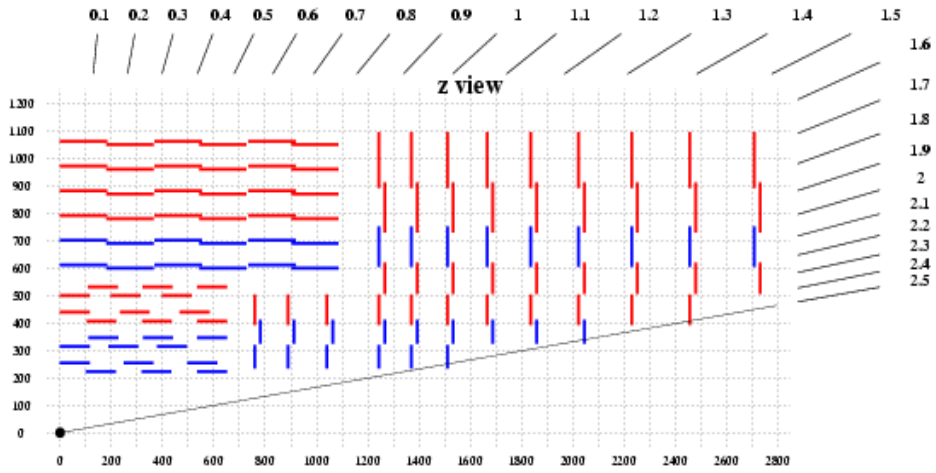

Figure 3.3 A schematic longitudinal view of the CMS tracker in terms of different layers and their arrangements in η and z direction in one quarter of the CMS detector.

of 20^0 around their radial symmetry axis(see Fig. 3.4). For reasons of low noise and long term stability, the pixel vertex detector will be operated at -10^oC.

The pixel detectors are covered by 10 concentric layers of silicon microstrip detectors in the barrel, while the endcap has nine such layers(TEC). In the barrel region these

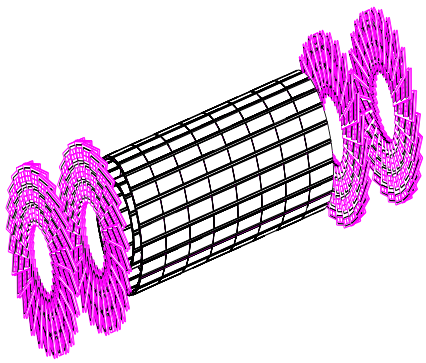

Figure 3.4 Layout of pixel detectors and the turbine shaped endcap disks in CMS.

detectors are located at a radius between 20 cm to 110 cm from the z-axis. The barrel section of the detector is categorized as Tracker Inner Barrel (TIB) and Tracker Outer

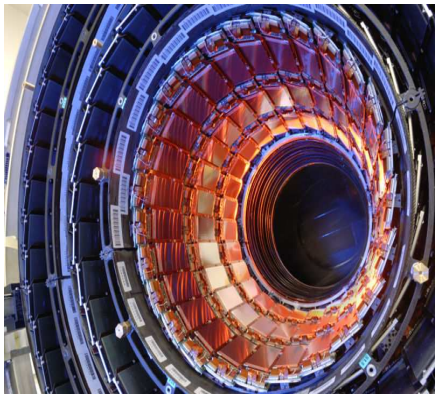

Figure 3.5 The picture of CMS inner silicon tracker at point 5.

Barrel (TOB). The TIB covers up to $|z| < 65$ cm and comprises of 4 inner layers with a resolution of 230 μm in z direction. The TOB consists of 6 outer layers and has a single point resolution of 530 μm in z direction. The TIB and TOB are complemented in the forward and backward region by the tracker inner disks(TID). The TID consists of three disks on each side and fills the gap between TIB, TOB and TEC. The silicon microstrip detector have ∼9.6 million channels. All silicon strip detectors are single sided and double sided are built by gluing two independent modules of single sided type back-to-back by a dedicated jig [71]. One of the main challenges at LHC is pattern recognition in the tracking system which requires low cell occupancy(i.e. high granularity) and high hit redundancy(large number of hits for a track). These requirements are fulfilled by the inclusion of MSGC detectors which are 6 m long and 3 m in diameter. They have been designed in such a way that they provide an average of 6 hits per track.

The overall design requirement of the tracking system is to reconstruct isolated high P_T tracks with an efficiency $> 95\%$ and high P_T charged particles in the jets with an efficiency $> 90\%$ over the full pseudorapidity range. The high P_T electron reconstruction efficiency is more than 90% while for muons($P_T^{\mu} > 1$ GeV) it is better than 98%. The transverse momentum resolution for isolated track is expected to be $\Delta P_T/P_T \approx 0.15 P_T \oplus$ 0.5% (in TeV/c) for $|\eta| \leq 1.6$ and could go upto $\Delta P_T/P_T \approx 0.60 P_T \oplus 0.5\%$ for the full

tracker coverage upto $|\eta|$ ≤2.5. If the outer muon chamber is also taken into account, the muon momentum resolution for 100 GeV muon for $|\eta|$ ≤2, comes out to be $\Delta P_T/P_T \approx 4.5\sqrt{p}\%$(where p is in TeV/c). Similarly the impact parameter resolution (in the plane perpendicular to beam axis) will be better than 35 μm over the full η coverage for particles with $P_T \geq 10$ GeV while in longitudinal plane it will be better than 75 μm. The tracking system with all its subdetector will provide an efficient b-tagging($> 50\%$) in the E_T range of 50-200 GeV [71, 72, 73].

The harsh radiation environment in the close vicinity of the collision point will be a major issue for the functioning of the tracker. The innermost layer of the pixel detector is expected to be taken out after four years of LHC operation at the designed luminosity. The outer layers are expected to survive for at least six years.

3.4.2 The Electromagnetic Calorimeter

The CMS electromagnetic calorimeter(ECAL) will play an important role in the study of new phenomena especially in search for intermediate mass Higgs boson decaying to two photon final state. Fig. 3.6 shows a schematic representation of different sub-detectors in CMS ECAL and their η coverage. The CMS ECAL consists of ECAL Barrel(EB), ECAL Endcaps(EE), and preshower detector in endcaps and has a geometrical coverage upto $|\eta| \leq 3.0$. Precise measurement of electron and photon and their separation is possible upto $|\eta|$ <2.6 because the tracker coverage support exists only in this region. Moreover hard radiation environment and pileup contribution in the forward region also adds to this limitation. The detector is designed to have an excellent position and energy resolution for electron and photon in the energy range of 1 GeV to 1 TeV.

The requirements of a compact EM calorimeter design inside the solenoid magnet, fine granularity and a fast response were best fulfilled by lead tungstate($PbWO_4$) crystals. The $PbWO_4$ crystals have a short radiation length(0.89 cm), small Moliere radius(2.2

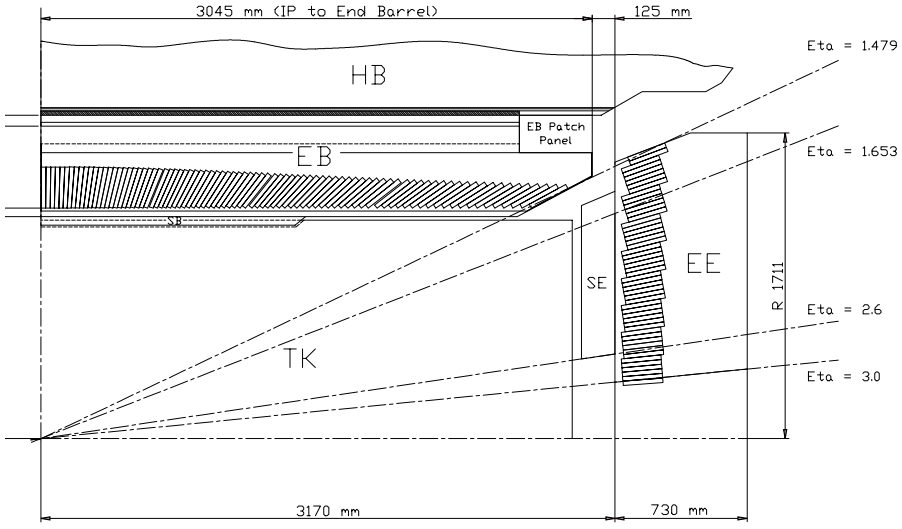

Figure 3.6 Layout of ECAL subdetectors presented schematically in one quarter of the CMS detector.

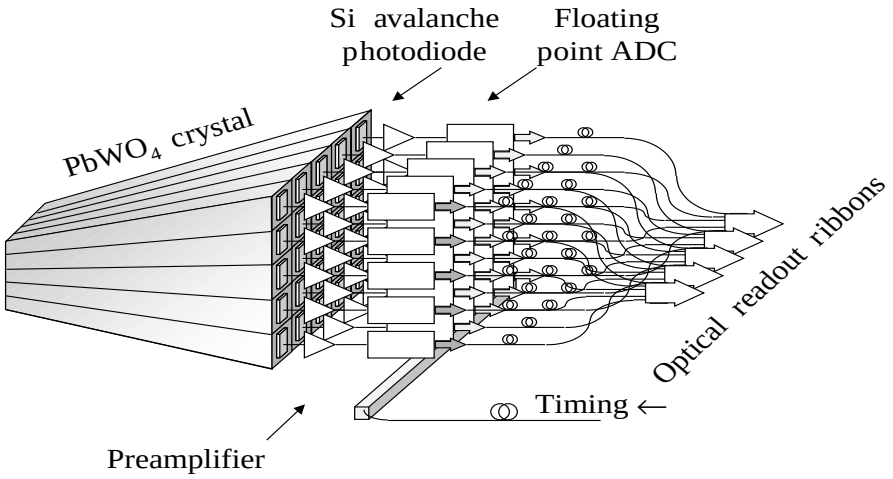

Figure 3.7 A schematic layout of electronic readout system for a 5×5 cluster module of $PbWO_4$ crystals in CMS ECAL.

cm), fast scintillation time(80% of the light is emitted within 25 ns), and are radiation hard(upto 10 Mrad). Beside these features it can easily be produced from available raw materials. The ECAL consists of 61,200 lead-tungstate crystals in the barrel ($|\eta|$ <1.44) region, and 7234 crystals each are mounted in the two endcaps($1.56 < |\eta| < 3.0$). In the barrel region each crystal has a size of 22×22 mm^2 and is 230 mm long. The crystals are 25.8 radiation length (X_0) in depth and contain most ($\sim$ 99%) of the electromagnetic shower while the endcap crystals are $24.7X_0$ deep. The granularity of the crystals in barrel is $\Delta\eta \times \Delta\phi = 0.0175 \times 0.0175$. In endcaps the off-pointing projective geometry using tapered crystal with a dimension of $24.7 \times 24.7 \times 220$ mm^3 are used. The granularity in endcaps varies from 0.0175×0.0175 to 0.05×0.05. Although lead tungstate crystal has a fast response time of 25 ns but due to low light yield the intrinsic gain is achieved by the use of photo detectors. An ECAL module of 5×5 matrix along with silicon avalanche photodiode(APDs) and readout system for barrel is shown in Fig. 3.7. In endcaps the APDs are replaced by vacuum photodiodes(VPTs).

For rejection of energetic photons arising from $\pi^0 \rightarrow \gamma\gamma$, an additional Pb-Si preshower detector is inserted before the crystal calorimeter for $1.653 \leq \eta \leq 2.6$. It contains two layers of lead, $2X_0$ and $1X_0$ in thickness respectively and each layer of lead is followed by a layer of silicon strip detector. Each silicon sensor has an area of 61×61 mm^2 and are made of 32 strips with a pitch of 1.9 mm. The lead layers generate the shower and silicon detectors measure the energy and impact position of the electromagnetic shower with good accuracy(300 μm at 50 GeV). With excellent design and very fine granularity, a single electromagnetic shower can be separated from two close electromagnetic showers arising from decay of π^0. The CMS ECAL energy resolution is given by

$$\frac{\delta E}{E} = \frac{a}{\sqrt{E}} \oplus \frac{a_n}{E} \oplus C \tag{3.3}$$

where a is the stochastic term(due to sampling fluctuation and shower containment),

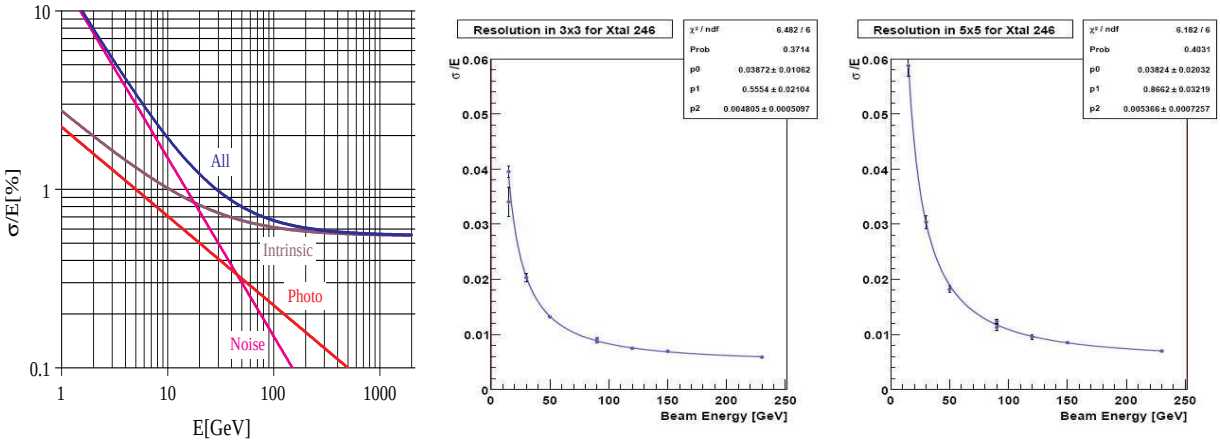

Figure 3.8 (Left)Expected energy resolution and contribution from different sources as a function of energy for CMS ECAL(from TDR). (Right)Energy resolution obtained in test beam for a typical crystal in the endcaps [74].

a_n is the noise term(due to pileup and electronics) and C is the constant term(due to calibration errors and various systematic effects). Using test beam data [74] taken in 2007, value of a and C has been measured to be 5.3% and 0.4% respectively. These are very close to the values of 2.7%(5.7%) for barrel (endcaps) for a and 0.55% for the constant term as mentioned in the CMS Technical Design Report [75]. The C term gives the largest contribution to the energy resolution for high transverse momentum(E_T >100 GeV) photons and electrons. Fig. 3.8(right)shows one of the latest results for test beam energy measurements of ECAL crystals [74].

3.4.2.1 Photon Reconstruction in ECAL

When a particle passes through the calorimeter, it produces a shower whose energy is absorbed by the crystals of the calorimeter. The photon deposits its energy in the ECAL with a subsequent showering in the form of e^+e^- creation($\gamma \rightarrow e^+e^-, e^\pm \rightarrow \gamma e^\pm$ and so on) and this energy generally spreads over many ECAL crystals in close geometrical proximity. These crystals are termed as cluster and the central crystal of the cluster usually have the highest deposited energy. Sometimes photon interacts with

the tracker material and an $e^{\pm}$ pair is produced which forms two nearby clusters in ECAL. Similarly the detector noise can also form small clusters in ECAL. To account for such energy usually cluster of clusters, known as *supercluster* is formed. While forming these superclusters noise can be rejected by requiring a minimum energy or E_T threshold on each crystal's energy. CMS experiment uses two separate clustering algorithms called Hybrid and Multi5X5 to form superclusters in the barrel and the endcaps respectively. The two algorithms are described briefly in the following section.

Hybrid Algorithm

This algorithm is used for the barrel section of the CMS detector and already forms part of CMS offline reconstruction analysis. The initial step in the reconstruction process is to start with a seed crystal in ECAL, called *ECAL rechits*, that represents a local energy maximum and fulfills the requirement of some E_T(or E) threshold. Using this seed as reference, "dominos" of crystals are formed. Each domino is centered at a seed crystal and extends in η direction. The dominos are formed either by 1×3 (if the maximum energy crystal has $E_T > 1$ GeV) or 1×5 crystal configuration for N steps crystal in each direction(as shown in Fig. 3.9). Nearby dominos are added to form the supercluster in ϕ direction. Some predetermined threshold is used to remove dominos which are most likely formed due to detector noise and largely determined from test beam results. The dominos of supercluster are then broken into basic cluster with each basic cluster having a seed domino with E greater than a threshold of E_{seed}. These basic clusters till now have been used to construct various isolation variables.

Multi5×5 Algorithm

For the endcaps, Multi5×5 superclustering algorithm is used. This algorithm has been recently included in the reconstruction process by replacing the Island algorithm for the endcaps. The first step in clustering is to search for rechits to find seed candidates

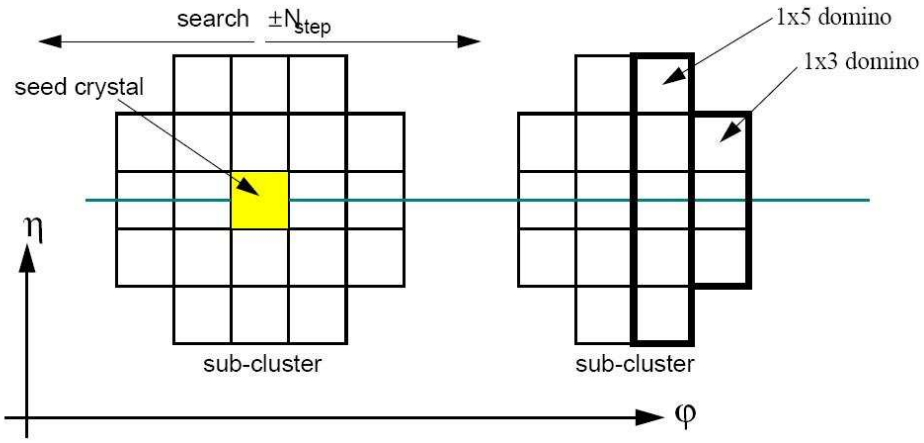

Figure 3.9 The hybrid algorithm and formation of 1×3 and 1×5 dominos in the ECAL crystal.

with transverse energy greater than some threshold. Once such a seed is found, a 5×5 crystal cluster is formed taking seed as the center of the cluster. The crystal which are added to a cluster are removed from the list of available crystals for the next cluster formation except those at the edges of the cluster. In Multi5×5 algorithm, these fixed size 5×5 crystals are called basic clusters and then these basic clusters are combined into supercluster object (this is in contrast to the hybrid algorithm where first supercluster are formed and then basic clusters are made). Since in the endcaps, bremsstrahlung from electron spreads in the ϕ direction, hence to recover this energy, the supercluster formation takes into account those clusters which are localized in η but spread in ϕ. For making supercluster from basic clusters again a basic cluster seed is chosen with some E_T threshold and other basic clusters are added to it based on whether η and ϕ falls within the η and ϕ roads of the basic cluster seed. These η, ϕ roads are defined by the parameters $\Delta\eta_{multi}(0.6)$ and $\Delta\phi_{multi}(0.06)$, which are the absolute values of the largest allowed seed cluster-to-cluster distances (basically basic cluster are matched to seed cluster in this way). Then supercluster formed are combined with preshower energy clusters to form the electromagnetic candidates.

3.4.3 The Hadron Calorimeter

The CMS hadron calorimeter(HCAL) will play a crucial role in search for new physics at the LHC. It will not only measure the jets from quarks and gluons but is also important for the measurement of missing transverse energy($\not{E}_T$). The HCAL also complements electron, photon and muon identification in ECAL and muon detector respectively. The HCAL in CMS detector can be categorized in the following pseudorapidity ranges: Hadron Barrel(HB) in $|\eta| \leq 1.305$, Hadron Endcaps(HE) in $1.305 < |\eta| < 3.0$, Hadron Forwards(HF) in $3.0 \leq |\eta| \leq 5.0$ and Hadron Outer(HO) for $|\eta| \leq 1.26$. Amongst these only HO is located outside the solenoidal magnet. Fig. 3.10 shows the above categorization schematically in $r - z$ plane and the respective η coverage.

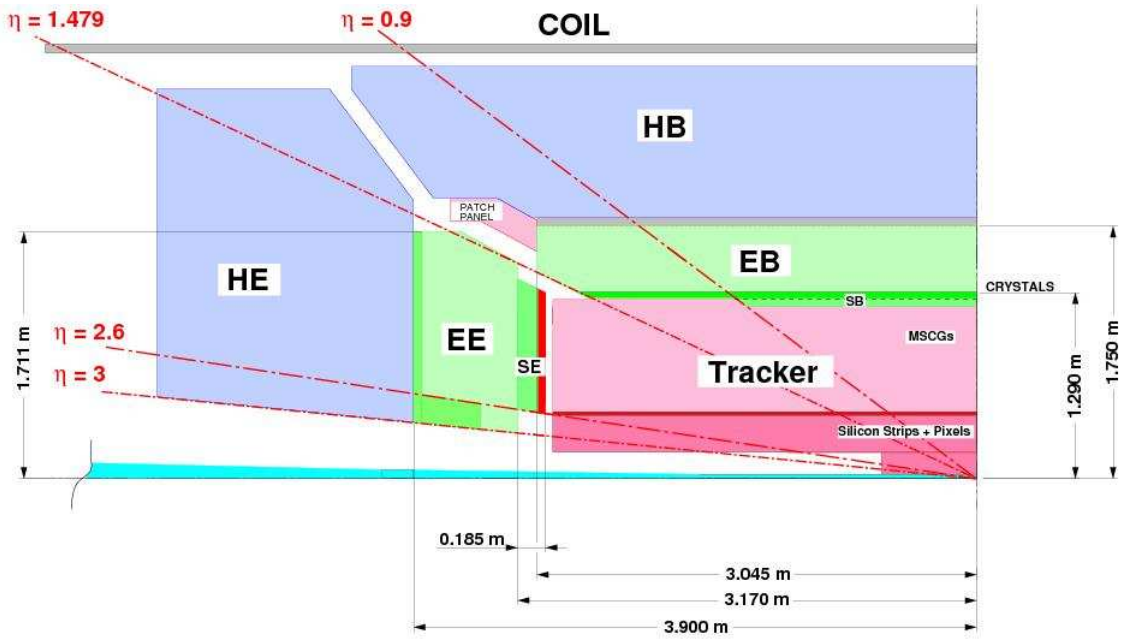

Figure 3.10 Different geometrical coverage of hadron calorimeter(HCAL) in CMS experiment(HO is not shown in this diagram).

The HB is 9 m long, 1 m thick and 6 m at the outermost diameter. It consists of two half barrels of 18 identical 20^0 wedges in ϕ. Each wedge is made up of brass alloy absorber plates with wavelength shifting fiber(WLS) readout. The HE has a diameter

ranging from 0.8 m to 6 m and a thickness of 1.6 m. For both HB and HE a sampling calorimeter made up of plastic scintillator sandwiched between the brass plates has been used. The choice of brass is due to the fact that it is non-magnetic in nature and has a short interaction length(λ_I). The HB contains 14 brass plates plus 2 external steel plates for mechanical strength. The first plate is 40 mm thick steel followed by eight brass plate each 50 mm thick, followed by six 56.5 mm thick brass plates and finally a 75 mm thick steel plate. The total thickness of the absorber at η =0.0 is about 5.82λ_I. The active scintillation tiles are 3.7 mm thick except the very first layer in the barrel which is 9 mm thick. The endcaps have 19 layers of active plates with similar thickness as in HB while for absorbers, which are entirely made up of brass, the thickness is 78 mm. The segmentation in HB and HE is $\Delta\eta \times \Delta\phi$ =0.087 $\times$ 0.087 while near and beyond $|\eta|$ =3, it becomes twice. The overall thickness in HB and HE varies from 5.15λ_I to 10.6λ_I as a function of increasing polar angle. The optical signal in the active component are detected with hybrid photo diodes(HPDs) mounted at the end of barrel.

To avoid shower leakage in the central region, additional outer hadronic calorimeter(HO) has been introduced after the magnet, which leads to a minimum of $\sim$ 11λ_I for calorimeter system in $|\eta|$ <1.26. The HO consists of two layers of scintillator tiles located on either side of the first layer of return yoke (YB1). The YB1 is about 30 cm thick and also acts as an absorber for the HO. The scintillation light is collected through WLS fibers embedded in the grooves of scintillation tiles.

Since the HF calorimeter($|\eta| \geq$3) is expected to experience very high flux from collision debris, it has been designed to survive the harsh radiation environment. The HF consists of quartz-fibers embedded in steel absorber. The forward calorimeter is essentially a cylindrical structure with outer radius of 130 cm and the front face of the calorimeter is located at 11.15 m from the collision point. The structure is divided in 20^o modular 18 wedges in ϕ. The steel absorber structure is composed of 5 mm thick grooved plates inserted with fibers. From functional point of view the detector is divided

longitudinally into two segments. Half of the fibers covers the full depth(termed as *long*) of the absorber while half(*short*) of them start after 22 cm from the front of the detector. This design compensates for the different response for hadronic and electromagnetic shower, and are read separately through different readouts. The Cherenkov radiation is produced in the active material of HF detector when hadrons interact with it. These signals are transmitted to phototubes(PMTs) through quartz fibers. Typical diameter of these fibers is 600 μm for core and about 800 μm with protective layer of acrylate buffer. These fibers run parallel to beamline and are bundled such that they form tower in $\Delta\eta \times \Delta\phi$ =0.175×0.175.

The energy resolution for a signle pion interacting with HCAL has been estimated to be $65\%/\sqrt{E} \oplus 5\%$ for the barrel ($|\eta| < 1.44$), $83\%/\sqrt{E} \oplus 5\%$ for the endcaps ($1.56 < |\eta| < 3.0$) and $100\%/\sqrt{E} \oplus 5\%$ for the forward region ($|\eta| > 3.0$) [76]. In a similar fashion as for ECAL, for high p_T jets(> 100 GeV), the constant term of 5% is the dominating contributor for the jet resolution. The latest test beam results shows that single pion interaction in the HCAL and ECAL+HCAL calorimetry yield a resolution function:

$$\frac{\Delta E}{E} = \frac{94\%}{\sqrt{E}} \oplus 4.5\% \tag{3.4}$$

and

$$\frac{\Delta E}{E} = \frac{83\%}{\sqrt{E}} \oplus 4.5\% \tag{3.5}$$

respectively. The expected performance for hadrons in the forward region is.

$$\frac{\Delta E}{E} = \frac{172\%}{\sqrt{E}} \oplus 9.0\% \tag{3.6}$$

Although with energy calibration the resultant jet energy resolution is expected to be better with $\Delta E/E = 118(156)\%/\sqrt{E} \oplus 7.0(5.0)\%$ for high(low) luminosity [73, 77, 78].

3.4.3.1 Jet Reconstruction in HCAL

As quarks and gluons can not be observed directly but fragments into a number of hadrons through hadronization, hence the jet reconstruction algorithms are used to collect this spread of energy in large $\eta - \phi$ region of HCAL. There are several algorithms which cluster energy deposits in CMS calorimeters into collimated objects of stable particles called "CaloJets". The calorimeter jets or Calojets are reconstructed using the calorimeter towers (also know as "CaloTowers") as input. These calotowers are made up of one or more HCAL cells and corresponding ECAL crystals due to electromagnetic fraction of a jet. In barrel, one HCAL cell and a 5×5 ECAL cluster forms a project tower while in the forward region a more complex combination is used. For standard jet reconstruction the calorimetric cell and the calotower has to pass certain threshold level. In CMS, iterative cone [79] and SIScone [80] algorithms are widely used for offline reconstruction of jets. In the following section we discuss the Midpoint cone [81] and SISCone algorithms while the iterative cone algorithm is described in the next chapter.

Midpoint Cone Algorithm

In this algorithm the calorimeter towers are considered for seed if they have a E_T >1 GeV and are put in a descending order and later they are used as the starting point for jet reconstruction. The procedure for Midpoint cone [81] algorithm is based on a iterative search to find a stable cone of radius R($= \sqrt{\Delta\eta^2 + \Delta\phi^2}$). The towers or rechits which comes inside this cone are not removed from the list and remains available for the next proto-jet. In this way overlapping prot-jets are formed. The infrared safety is taken into account by considering the midpoint between each pair of proto-jets (which are closer than the 2R) as additional seed for the combined momentum. Then these midpoints are again used to find more proto-jets. When all proto-jets are formed, merging and splitting procedure is applied. If the highest E_T proto-jet does not share any object or tower with other proto-jets, it is defined as jet and removed from the list of proto-jets. Otherwise,

the transverse energy shared with the highest E_T neighbor prot-jet is compared to the total transverse energy of this neighbor proto-jet. If this fraction is greater than 50% the proto-jets are merged, otherwise the shared objects are individually assigned to the proto-jet that is closet in $\eta - \phi$ space. This procedure is repeated with the next highest E_T proto-jet. To define the jet four momentum, usually a recombination scheme(such as E-Scheme) is used for all the algorithms. It has been found that Midpoint cone algorithm is not a infrared-safe method for pQCD orders beyond NLO.

SISCone Algorithm

SISCone [80] is the "**S**eedless **I**nfrared-**S**afe **C**one" algorithm for jet reconstruction. The only disadvantage it has compared to the Midpoint Cone clustering algorithm is its higher execution time. This algorithm is also collinear safe to all orders of pQCD and is now part of the CMS reconstruction softwares.

3.4.4 The Muon System

Many of the benchmark physics channels(e.g. $H \rightarrow ZZ \rightarrow \mu\mu\mu\mu$) for discovery of new physics contains muons in the final state and hence a very precise measurement of properties of these particles is one of the central ideas behind the CMS detector design. The design of muon chambers were driven by very strong requirements of precision and redundancy. For example, for good physics performance in the golden channel for high mass Higgs search ($H \rightarrow ZZ \rightarrow \mu\mu\mu\mu$), a transverse momentum resolution of $\sim$9% (15-40%) is required for 200 GeV(1 TeV) muons [82]. Combining the information from inner tracker, a global resolution of 1%(5%) for low P_T(1 TeV) muon is expected [83]. Also, the muon chambers must have very fast trigger timing to cope with the 40 MHz collision rate. It must work in a harsh radiation environment with a magnetic field of $\sim$3.0 Tesla and a very high muon rate in endcaps and forward regions.

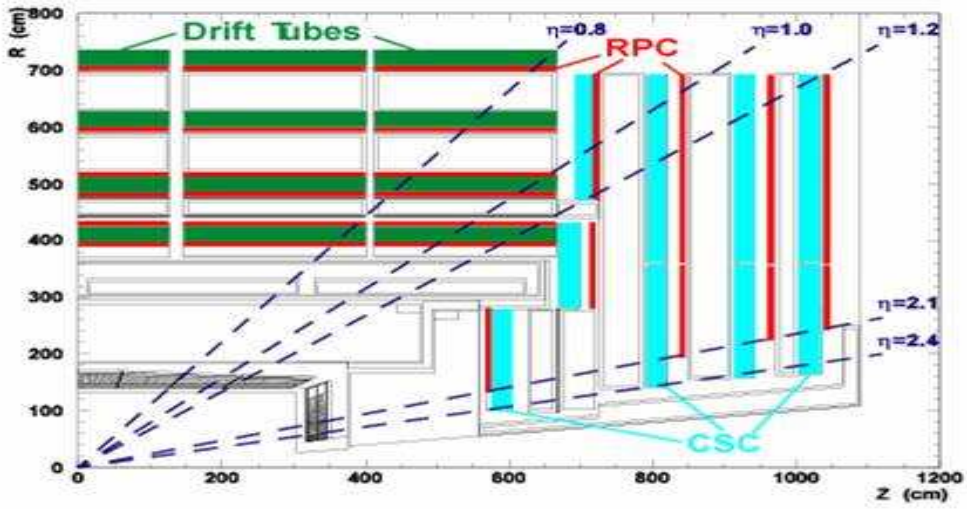

Figure 3.11 Layout of different types of muon chambers and their location in one quarter of the CMS detector.

The muon system of CMS can broadly be divided into barrel($|\eta| < 1.2$) and endcap ($0.9 < |\eta| < 2.4$) regions. The barrel region is made up of drift tube(DT) chambers while in the endcaps cathode strip chambers(CSC) have been used. In the barrel, muons are identified in four concentric ("stations") layers (see Fig. 3.11), each consisting of several planes of DT, inserted in the solenoid return yoke. Each of the station is segmented in three parts and hence a total of 12 sectors. In the barrel region the momentum is measured three times: inside the inner tracking volume, just after the coil in muon chambers, and in the flux return region. The DT detectors are rectangular in shape and they have a drift time of 380 ns. For barrel an overall spatial resolution of 100 μm in the $r - \phi$ plane and 150 μm in the beam direction is expected.

The choice of CSC in endcaps is due to its capability to operate at a higher flux rate ($\sim$ 100 kHz cm^{-2}) and a non uniform magnetic field of 1-3 TeV. Each CSC is a multiplicational chamber with trapezoidal shape. Each station also contains triggering planes made up of Resistive Plate Chambers(RPC) as shown in Fig. 3.11. The CSCs are distributed in concentric rings of 18 or 36 chambers, 3 rings in the internal face(ME1),

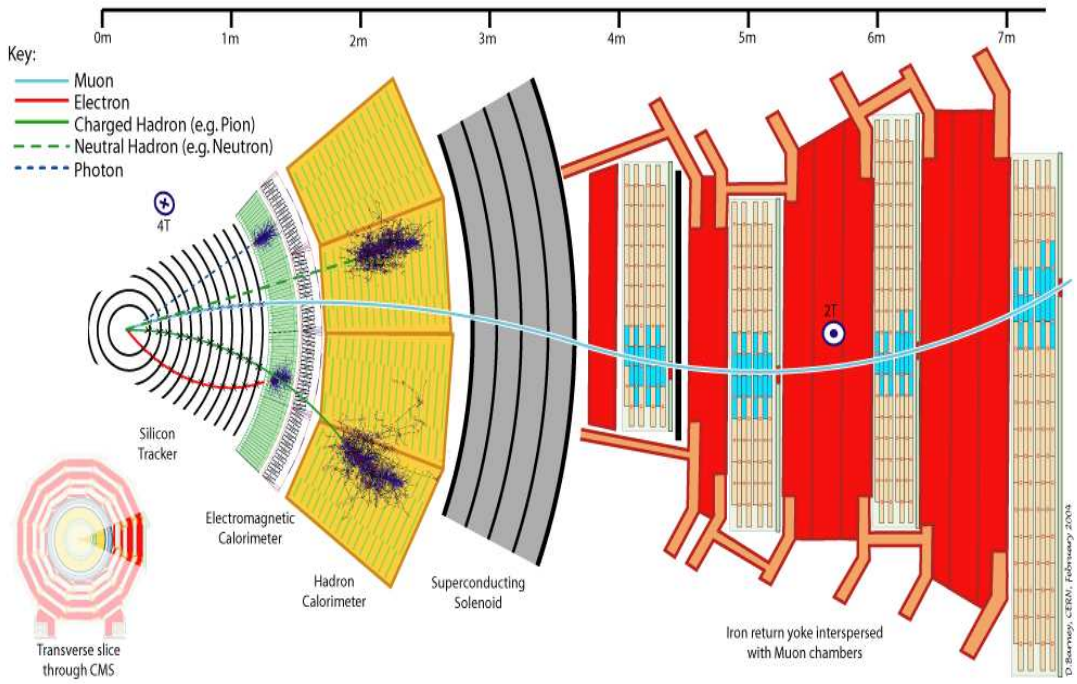

Figure 3.12 A schematic representation of a muon passing through all major detectors including the muon chambers in the magnetic field.

2 in the middle disk(ME2, ME3) and the 4th one in large η region(ME4).

Fast triggering in the muon spectrometer is ensured by inclusion of RPCs both in barrel and endcaps. The DT and RPCs are coupled together in the barrel region and each DT has either one or two RPCs planes. In the endcaps the RPCs are installed at the faces of iron disks. A maximum of 6 RPC plane in barrel and 3 plane in endcaps can be crossed by a high momentum muon. The triggering through RPC is based on pattern comparator algorithms(PACT). The RPCs are made of double thin gaseous gap using two bakelite plates separated by insulating spacers. They work in avalanche mode, has a time resolution of $\sim$1.5 ns and space resolution better than 1 cm [83, 84]. Figure 3.12 shows a schematic view of a muon passing through various subdetectors of the CMS detector including inner tracker, calorimeter, solenoid and the muon chambers.

3.5 L1, HLT Triggers and DAQ System

The CMS trigger and the data acquisition system is designed to cope with the unprecedented interaction rate [83, 85, 86]. At the designed luminosity of $10^{34}cm^{-2}s^{-1}$, the beam crossing rate will be 40 MHz with an event size of ∼1 MB, hence it will not be possible to store every interaction for offline processing. At CMS the maximum rate of data storage for offline processing is limited to 100 Hz which must be efficiently used to select and store interesting physics events. For this purpose CMS has employed two level trigger systems to reduce the rate upto the level of 100 Hz. The first level is called the Level-1 Trigger(L1), which is based on highly customized fast electronics followed by the High Level Trigger(HLT) which is implemented on a large cluster of commercial processors (Event Filter, Event Filter Farm). Various components of DAQ and triggers system for CMS are shown schematically in Fig. 3.13 .

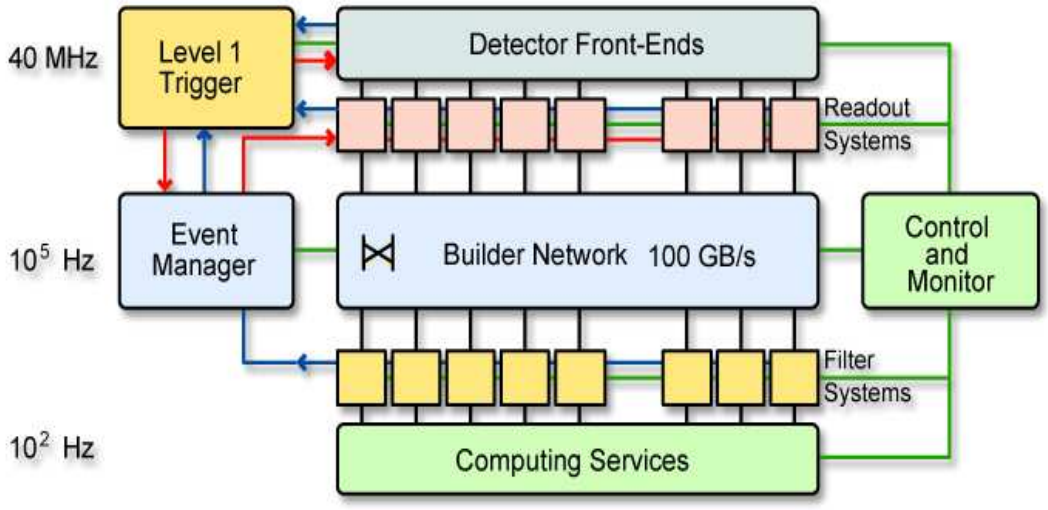

Figure 3.13 A layout of CMS architecture of Data Acquisition System(DAQ) and Trigger and various important components.

The L1 trigger has access only to coarsely segmented calorimeter and muon detector information in order to identify various physics candidate objects. At this stage isolation

criteria is applied without any information from the tracking system. The rejection and acceptance by trigger is based on the characteristics of the trigger objects. These trigger objects or candidates are identified from the detector information. The data from the front end electronics of various sub detectors are put into 10^7 channels with a latency time(or *dead* time) of 3.1 μs. This latency time is equivalent to 128×25 ns beam crossing at the designed luminosity. After an event gets accepted by the L1 trigger, about 700 Front End(FE) modules holds the stored event data, each carrying abut 1-2 kB of data per L1 trigger accepted event. The L1 accepted signals(10^2 kHz) and raw readout data are sent to a computer farm through a temporary storage buffer.

The next level is HLT which applies a reduction factor of 1000 to the output of L1 trigger. The full resolution and granularity of the detector is used to achieve such a large rejection factor. At this stage the information from tracker is also used for isolation and trigger selection and it is as sophisticated as at the time of offline processing of the data. It essentially combines the traditional L2 and L3 trigger components and allows a coherent use of HLT algorithms for multiple physics channels. Here the software used are the same as will be used in offline analysis of the data. This requires fully programable commercial processors(EF farms) for the running of HLT algorithms with a mean time of 10 ms per event along with the maximum input rate of 100 kHz. The trigger selection are implemented as "trigger path" where a trigger path is a set of algorithms which reconstruct one or more physics candidates and applies selection criteria to these reconstructed candidates and their various isolation and kinematical quantities. If the event passes one or more of these paths, the event gets accepted and stored for analysis. Table 3.2 shows few trigger paths for photon/electron HLT selection in CMS for different physics studies at $\sqrt{s} = 14$ TeV. In Table 3.3, various HLT triggers paths for photon and their expected rates are shown at $\sqrt{s} = 10$ TeV for $1 \times 10^{31} cm^{-2} s^{-1}$[87]. These triggers will be used for MC exercises in CMS till the end of 2009.

The DAQ system collects the data from ∼650 FE at the detector side, to the "filter

Trigger Path	Signal	Background	Total
Single Electron ($E_T > 26$ GeV)	$W \to e\nu$ 9.8 Hz $Z \to e^+e^-$ 1.3 Hz	Jets 9.4 Hz	20.5 Hz
Double Electron ($E_T^1, E_T^1 > 12$ GeV)	$Z \to e^+e^-$ 1.1 Hz	Jets 0.8 Hz	1.9 Hz
Single Photon ($E_T > 80$ GeV)	$\gamma + jet$ 2.1 Hz	Jets 1.4 Hz	3.5 Hz
Double Photon ($E_T^1, E_T^1 > 30$ GeV)	≈0 Hz	Jets 1.9 Hz $\gamma + jets$ 0.4 Hz	2.3 Hz

Table 3.2 HLT triggers and output rates for photon and electron for different HLT trigger paths at a luminosity of 2 $\times 10^{33} cm^{-2} s^{-1}$ for $\sqrt{s} = 14$ TeV.

Trigger Path Name	E_T (GeV)	HLT Pre-scale	HLT rate (Hz)
$HLT - Photon15 - L1R$	>15	20	8.03±0.82
$HLT - Photon20 - LooseEcalIso - Track - L1R$	>20	10	4.60±0.62
$HLT - Photon25 - L1R$	>25	1	20.50±1.31
$HLT - DoublePhoton15 - L1R$	>15	10	4.69±0.63
$HLT - Double - Photon15 - VeryLooseEcalIso - L1R$	>15	1	0.17±0.12

Table 3.3 HLT triggers and output rates for photon for different HLT trigger paths at a luminosity of 1 $\times 10^{31} cm^{-2} s^{-1}$ for $\sqrt{s} = 10$ TeV.

units" for processing of complete units. Thus DAQ is expected to provide a 100 kHz $\times$1 MB= 100 GB/s bandwidth for a sustained transfer of data from FE to about 1000 processors for HLT processing. The intermediate stages of such large transfer rate requires of a switching networks also called "Builder Network". The flow of data from FE to EF farm takes place through Event Manager(which is responsible for data flow through the DAQ) and Control and Monitor System (responsible for control, monitoring and configuration of all elements).

At the startup of the LHC the data from minimum bias events and objects from SM physics signatures will be used for calibration and alignment of the detectors. At a low luminosity of $10^{32} cm^{-2} s^{-1}$, the time constraint on L1 output will eventually lead to a

rate of 50 kHz. Due to various uncertainties involved in QCD events (being the largest fraction), a reduction factor of three will be used to make it ∼12 kHz at L1 level. For HLT, the expected output for the first three months is expected to be ∼150 kHz(reduced by a factor of 2 due to involved uncertainties). The time budget for this configuration has been estimated ∼40 ms.

Chapter 4

Event Generation

"Programming software is a constant fight."

- Anonymous.

Although the tree-level perturbative quantum field theory (QFT) has a simple description of the scattering and decay processes in an event in high energy collision, the observed high-energy processes usually contain significant amount of modifications, e.g., photon and gluon bremsstrahlung, loop diagram corrections, which are usually complex to be easily calculated directly at the diagrammatic level. Also, the non-perturbative nature of the QCD bound states make it necessary to include information that are outside the perturbative QFT. And in collisional systems more complex than few leptons and hadrons (e.g. heavy-ion collisions), the collective behavior of the system would involve a phenomenological description that also cannot be easily obtained from the fundamental field theory by trivial calculations. Any realistic description of the underlying physical process in a particle accelerator experiment, therefore, requires an adequate inclusion of these complex behaviors accompanying the actual process. Based on the fact that in most processes, factorization of the full process into individual problems is possible

(briefly discussed in Appendix-B), these individual processes are calculated separately, and then probabilistic branching among them are performed using Monte Carlo methods to produce full event in Monte Carlo event generators. These Monte Carlo event generators are equipped with physics details as well as supported by advance mathematical calculations.

4.1 Monte Carlo Event Generators

The task of a Monte Carlo(MC) event generator is to perform, initial composition, initial state radiations, hard scattering, resonance decays, final state radiations, underlying and multi-parton(MPI) interactions and hadronization. There are separate categories of generators which only produce the hard matrix elements without any showering and hadronization of partons. The final state under the present work, $\gamma + jet$ and $\gamma\gamma$ production has been well integrated in most of these packages.

There are several MC generator programs that generate events in proton-proton, proton-antiproton, electron-positron, electron-proton and other such collisions. Among these the general purpose MC generators are PYTHIA [88], HERWIG [89], ISAJET [90]. They have included all the generation steps mentioned above from PDFs to hadronization to final state particles. They are based on perturbative QCD and phenomenological models (for various new physics signals). These are LO event generators and effectively do resummation upto LO with the inclusion of parton showers. These generators are also used for showering and hadronizaiton of hard matrix elements generated from other generators which can not perform this task. The final-state particles generated by event generators can be fed into detector simulation softwares, allowing a precise prediction and verification for the entire system of experimental setup. However, as the detector simulation is usually a complex and computationally expensive task, simple event analy-

sis techniques are also performed directly on event generator results and have been found useful.

On the other hand Alpgen [91], Madgrpah [92], MC@NLO [93] and many such other generators perform very specific generations. These are hard matrix element generators and can produce multiple parton states. These generators are expected to provide a better description of kinematical shapes and cross section for various processes as it actually happens in pp or $p\bar{p}$ collisions. The final state of an event usually contains many jets and other particles. For example in Alpgen one can generate $\gamma + jet$ with $\gamma + 1jet$, $\gamma + 2jet$, upto $\gamma + 6jet$ final state. The presence of each extra jet affects the kinematical quantities like transverse momentum, back-to-back behavior of the leading γ and the leading jet. Similarly these generators can produce $M\gamma + Njet$ with the restrictions $M > 0$ and $N + M \leq 8$. For the showering and hadronization, these generators can be interfaced with PYTHIA and HERWIG using Les Houches Accord(LHA) interface procedure.

There are other types of generators that also do partonic level calculation for cross-section rather than producing events. The best examples in view of present analysis are JETPHOX and DIPHOX programs specially designed for an effective full NLO calculation [94]. These packages are able to reproduce the inclusive experimental data for $\gamma + jet$ and $\gamma\gamma$ production at Tevatron [39] quite precisely and even explain those features which were not answered by other MC generators. They take into account one fragmentation contribution at NLO level and two fragmentation processes at LO level. The other feature they provide is the use of isolation requirements to compare with the data in a realistic manner [39, 40] which has really helped in classifying many features of the actual data not understood before.

For the analysis presented in this thesis for both signal and background event generation, we have used PYTHIA as the event generator.

4.1.1 Hadronization Models in Monte Carlo Generators

For any analysis, especially involving γ and jet in the final state, the process of hadronization of parton/quark is of immense importance for a realistic description of full event due to fake photons arising from jets. In MC generators the treatment of colored partons to colorless hadrons is based on theoretical and phenomenological models. Different prescription has been developed over the years to describe the hadronization phenomena. Each methodology contains several parameters that are tuned using experimental data. At present PYTHIA and HERWIG are mostly used for showering and hadronization purpose in MC simulations. Below we present a brief description of the hadronization models used by these programs.

- String Model: The PYTHIA uses string model for event generation. In this model as the final state q and $\bar{q}$ partons move apart from common production vertex, the physical picture is that of a color flux tube being stretched apart between q and $\bar{q}$. If the tube is assumed to be uniform along its length, this automatically leads to confinement scenario with a linearly rising potential. As they move apart, with the increase in potential stored in the string, it breaks and creates new $q'\bar{q'}$ pairs. So the system splits into two color singlets of $q\bar{q'}$ and $q'\bar{q}$. If the invariant mass of either of the pair is large enough, further pair creation may proceed in a similar manner. In this model, the process is assumed to proceed until only on-mass-shell hadrons remain. Figure 4.1(a) shows the schematic picture of string model of hadronization.

- Cluster Model: The HERWIG uses cluster model of hadronization. The cluster model is very different compared to the string model. This model is based on the color pre-confinement property of perturbative QCD(pQCD). After the parton shower evolution, the remaining gluons split into $q\bar{q}$ pairs. The nearest q and $\bar{q}$ then combine into a color singlet cluster with a mass of the order of few GeV.

These clusters decay directly into two hadrons unless they are very heavy, in that case they decay to two clusters; or too light then to a single hadron. In many experiments it has been tested that the hadronic energy and transverse momentum are estimated quite well for final state in this model. In Fig. 4.1(b), we show the schematic description of cluster model for hadronization.

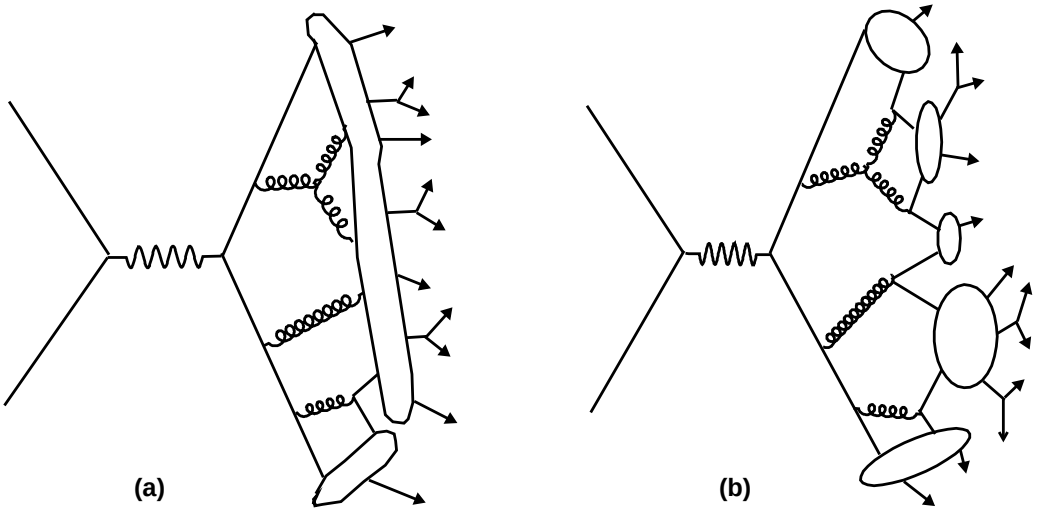

Figure 4.1 Hadronization using (a)*string* and (b) *cluster* models in Monte Carlo event generators.

4.1.2 CMKIN: CMS Event KINematics Generation

CMKIN is a standard framework developed for CMS simulation studies to provide the interface for various matrix element generator to go through the process of showering and hadronization using PYTHIA and HERWIG. The output of CMKIN can be used as input to detector simulation [95]. The advantage of using CMKIN is that it converts and stores the event information in a common format know as HEPEVT format. HEPEVT is a common block which is a HEP standard to store all the event information [96]. These HEPEVT can be converted to ntuple and then to roottuple which can be easily

analyzed within the ROOT framework. The maximum number of particles/parton which can be stored in HEPEVT is about 3200 hence HEPEVT is stored in packed format. This packing increases the capacity up to 3900 particles thus reducing the size of final rootuple. Various matrix element generators like Alpgen, CompHep, Madgrpah, TopRex events can be used in CMKIN for showering and hadronization using LHA [97]. Using LHAPDF package [98] latest PDFs such as CTEQ6M, MRST can also be used very easily within the CMKIN framework. The input parameters for event generation are provided using simple user datacards. To select and store only those events which fulfill certain kinematical requirements *user selection* routines are used.

4.1.3 Pre-Selection

Since a jet faking a photon probability varies from $\sim 10^{-3} - 10^{-4}$ as a function of photon P_T, to reasonably estimate the QCD background for photons and to reduce statistical fluctuations in the measured kinematical quantities, usually a large statistics of QCD background is needed. For practical reasons it is not possible to keep such large number of events, out of which a large fraction will be filtered due to some phase space restriction at the beginning of an analysis. Since each event consists of many particles created in the collision, the ntuple or rootuple containing their kinematical information are very large in size and it is difficult to store them for practical purposes. Moreover processing uninteresting events will be time consuming from the analysis point of view. To avoid such problems usually pre-selection routines are used to filter out events which are *not* useful for the analysis. We have used a similar user-selection routine for event generation for both analysis presented in this thesis. The two main task of this pre-selection routine are:

- To run algorithm(defined in the next section) for photon and jet candidate formation at the generator level, and

- Apply P_T threshold on leading photon and leading jet candidates to select useful events for further analysis.

4.2 Photon Candidates

Since the SM $\gamma + jet$ and QCD dijet production processes form a significant background to $q\bar{q} \to \gamma\gamma$ and $pp \to \gamma + jet$ via q^* exchange, it is crucial to understand the mechanism of a jet faking a photon and include its effects into the results. The identification of a reconstructed object as a photon candidate depends on the specific design of the detector and the reconstruction algorithm. Taking this into consideration, at the generator level, we have used a clustering algorithm to account for fake photons arising from jets [99]. The CMS experiment uses $PbWO_4$ crystals for the electromagnetic calorimeter (ECAL). Each crystal covers 0.0175×0.0175 (1°) in the $\Delta\eta - \Delta\phi$ space. For photon candidate reconstruction, we have used a similar algorithm as "hybrid" algorithm [100] discussed briefly in chapter-3.

The first step of the algorithm is to find a seed above a certain minimum transverse momentum threshold P_T^{min} of 5 GeV [75]. Only final state electromagnetic(EM) objects, i.e., γ, e^+ and e^- are chosen as seed. Subsequently, one searches for electromagnetic particles around the seed in the $\eta - \phi$ direction, where $\Delta\eta$ and $\Delta\phi$ distance from the seed object is at most 0.09. This extension is equivalent to 10×10 crystal matrix size in the CMS detector. The CMS experiment uses 5×5 crystal size to form an energy cluster and nearby non-overlapping clusters are merged to reconstruct a photon candidate. However, in our effort to mimic this reconstruction process at the generator level, we chose to be conservative and used a 10×10 crystal to collect the EM energy. We define the momentum of a photon candidate to be the vector sum of the momenta of the electromagnetic objects in such crystals. This is also known as *E-scheme*. A photon candidate could be either a direct photon or other electromagnetic objects such

as $\pi^0 \rightarrow \gamma\gamma, \eta \rightarrow \gamma\gamma, \rho^0 \rightarrow \gamma\gamma$ etc. In case of $\gamma\gamma$ analysis, events with two highest E_T photons having $\cos\theta_{\gamma_1\gamma_2} > 0.9$, $\theta_{\gamma_1\gamma_2}$ being the opening angle between the two photons, are not considered because they could merge into a single energy cluster in the real detector. On the other hand no such condition was used for $\gamma + jet$ analysis.

Following this algorithm and requiring the photon to be isolated (to be discussed later), the estimated probability of a jet faking a photon in $\gamma + jet$ channel is $\sim 10^{-3}$. With the use of above mentioned algorithm at the generator level, the major sources found for fake photons are shown in Table 4.1 along with their respective contributions to selected photon candidates.

Particles	Fake photon contribution
π^0	~81 %
η	~12 %
ω	~3 %

Table 4.1 Major contribution of mesons to fake photons in a $\gamma + jet$ event sample.

4.2.1 Comparison with Fast Detector Simulation

We compared our results from generator level studies with the fast detector simulation(FAMOS [101]) used for CMS experiment and they are found to be in good agreement. For this comparison we have used FAMOS version 1.4.0. In Fig. 4.2 we show $\Delta\eta$ and $\Delta\phi$ difference between the reconstructed EgammaSuperCluster from FAMOS and the Generator level photon candidates(or *Generator level EgammaSuperCluster*). The photons were E_T ordered and then matched between the two sets with the condition that $\Delta\eta \leq 0.1$ and $\Delta\phi \leq 0.1$ between the photons. We have also checked the correlation between the generator level photon candidate and FAMOS EgammaSuperCluster. Figure 4.3 shows the correlation between η and ϕ for generated and reconstructed photon candidates. It is found that more than 90% of photons matches with the above men-

tioned condition. This matching was done by applying equal P_T threshold requirements on both generator level and reconstructed photons. Here it should be emphasized that at the reconstruction level we have not taken into account the converted photons which may reduce the matching efficiency by ~ 5 %. If the P_T requirement on the reconstructed EgammaSuperCluster is lowered by 3-4 GeV then the matching efficiency increases by 2-3 %. We found similar outcomes for low P_T ($50 < P_T^{\gamma} < 200GeV$) photons.

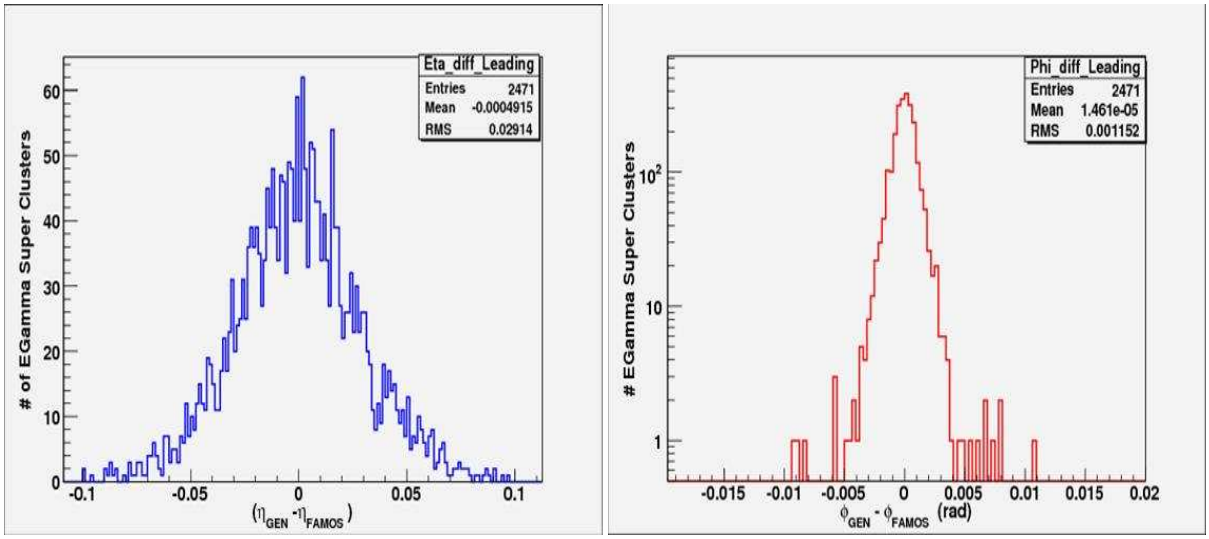

Figure 4.2 Difference in η and ϕ between reconstructed(FAMOS) and generator(GEN) level photon candidates.

We also compare the resolution for different energy bins obtained for the generator level algorithm. Figure 4.4 shows the energy difference between the reconstructed photon candidate (E_{FAMOS}) and the generator level photon candidate (E_{GEN}) for two different energy bins. A Gaussian distribution has been used to fit the histograms. The energy resolution for the CMS ECAL is given by those in eq.(3.3): where the stochastic term(a), noise term(a_n) and constant term (C) are added in quadrature. For each of these terms, we have used values identical to those for the electromagnetic calorimeter of the CMS

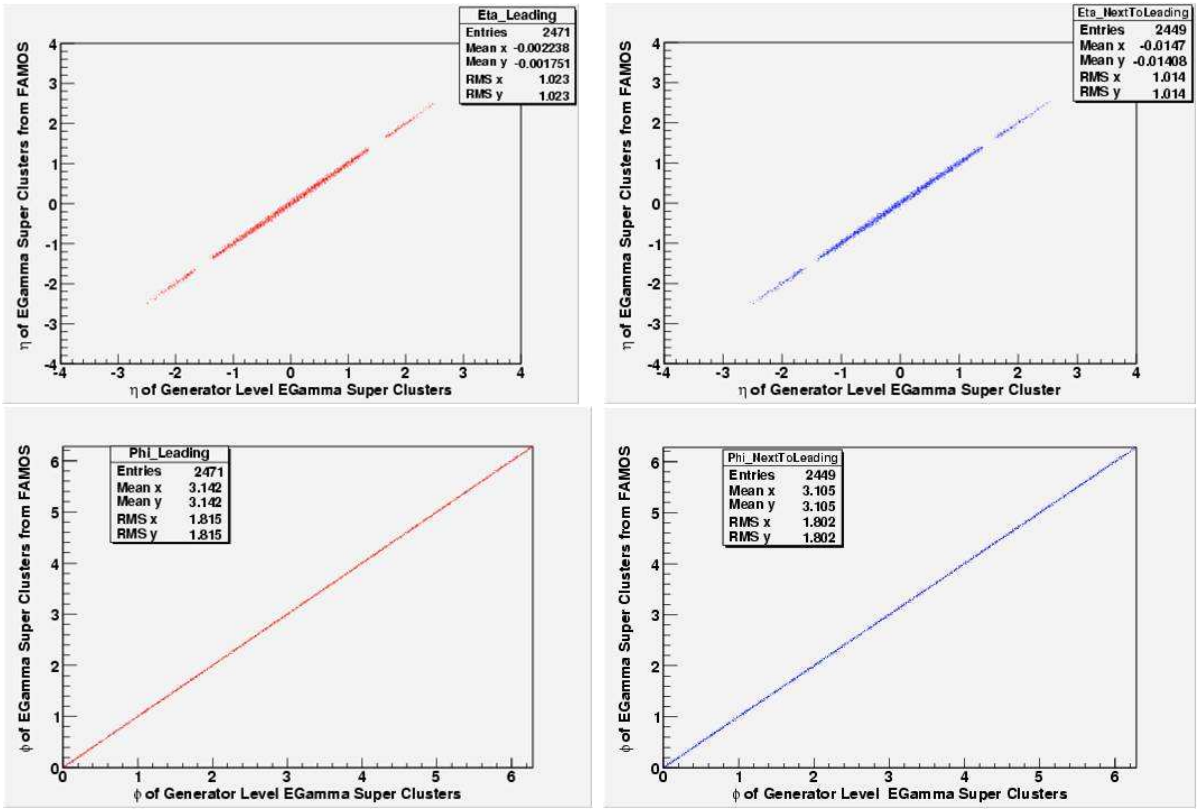

Figure 4.3 Correlation in η and ϕ for the reconstructed and the generator level photon candidates in $\gamma + jet$ events.

[75], namely

$$
\begin{aligned}
C &= 0.55\% \\
a_n &= \begin{cases} 2.1 \times 10^{-3}\,\mathrm{GeV} & |\eta| < 1.5 \\ 2.45 \times 10^{-3}\,\mathrm{GeV} & 1.5 \le |\eta| \le 2.5 \end{cases} \\
a &= \begin{cases} 2.7 \times 10^{-2}\,\mathrm{GeV}^{1/2} & |\eta| < 1.5 \\ 5.7 \times 10^{-2}\,\mathrm{GeV}^{1/2} & 1.5 \le |\eta| \le 2.5\ . \end{cases}
\end{aligned}
$$

For high energy photons the constant (C) term dominates the above expression and one expects a resolution of 0.55% for $E > 100$ GeV. Figure 4.5 shows energy resolution obtained with $\Delta E = E_{FAMOS} - E_{GEN}$. It is in good agreement with CMS ECAL PTDR result(see chapter-3, Fig 3.8(left)).

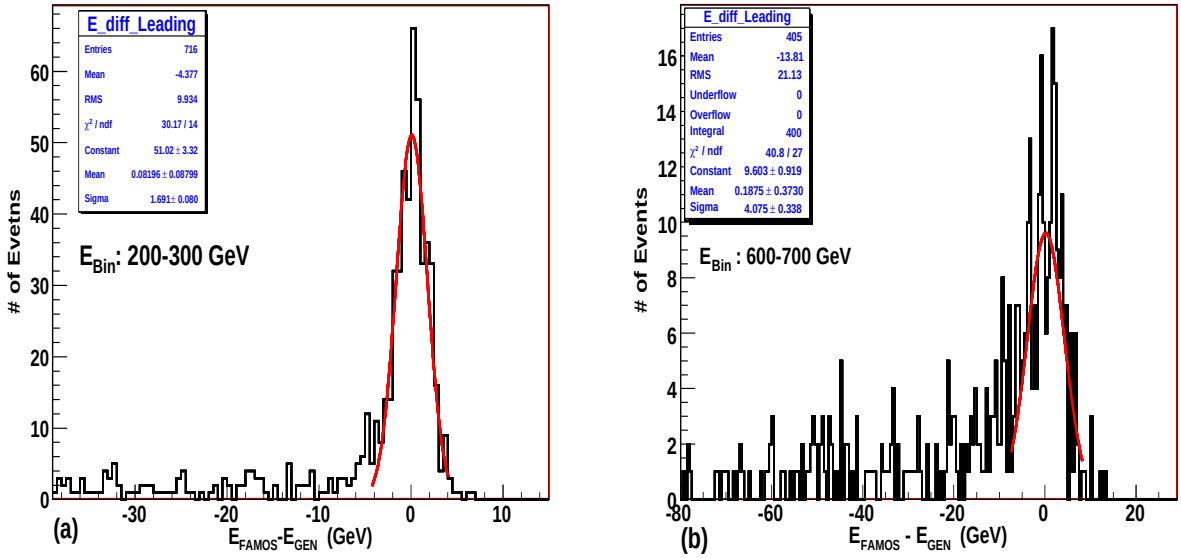

Figure 4.4 Difference in energy between the reconstructed photon candidates (E_{FAMOS}) and the generator level photon candidate (E_{GEN}) for different energy bins.

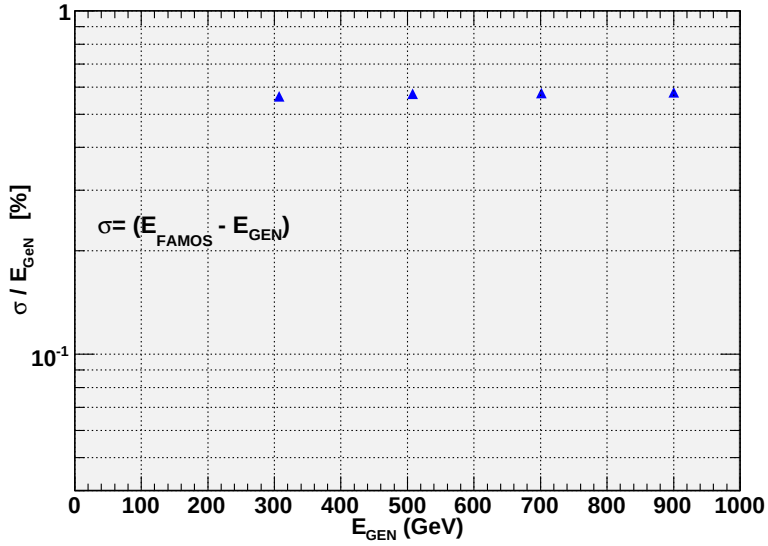

Figure 4.5 Energy resolution obtained from FAMOS using generator level photon candidate formation algorithm.

4.3 Jet Candidates

In chapter-3, we have briefly discussed some of the jet reconstruction algorithms. In CMS, one of the algorithms used for offline analysis is called *Iterative Cone* algorithm. We have used this method for particle level jet formation for $\gamma + jet$ analysis.

Iterative Cone Algorithm

For jet reconstruction, various algorithms have been used by different collider experiments. These include the Midpoint Cone [81], Iterative Cone [79, 102], and the K_t algorithm [103, 104, 105]. These algorithms are used mostly for offline analysis. Since we have used the CMS setup in our analysis, we used Iterative Cone algorithm to reconstruct jets at the generator level. Being much faster, this is commonly used for software based triggers. While the first algorithms for the jets at the hadron colliders started with simple cones in the $\Delta\eta - \Delta\phi$ space [106], clustering techniques have greatly improved in sophistication over the last two decades[81, 103]. For a real detector, the first step in the reconstruction process, before invoking the jet algorithm, is to apply noise and pile-up suppression with a set of cuts on E_T. To simulate "perfect detector jets", we used a seed P_T cut on the P_T-ordered final state particles and selected only those which have a transverse momentum above the required minimum[2] of $P_{Tseed} \geq$1.0 GeV. Once the seed is selected, we searched around for all the particles in a cone of $\Delta R \leq 0.5$. The objects inside the cone are used to calculate a *proto-jet* direction and energy using the E-scheme($\sum P_i$). The computed direction is then used to seed a new proto-jet. The procedure is repeated until both the energy and the direction of the putative jet is stable between iterations. We quantify this by requiring that the energy should change by less than 1% and the direction by less than $\Delta R = 0.01$. When a stable proto-jet is found, all

[2]The seed threshold can vary from 0.5 to 2.0 GeV depending on the energy of the reconstructed jet.

objects in the proto-jet are removed from the list of input objects and the stable proto-jet is added to the list of jets. The whole procedure is repeated until the list is bereft of objects with an E_T above the seed threshold. The cone size and the seed threshold are the parameters of the algorithm.

4.4 Events Generation for $\gamma + jet$ Analysis

Since the theoretical model of compositeness under consideration as described in chapter-2, is not available in any of the event generators for event production, we calculated the matrix elements and incorporated them inside the PYTHIA framework for event generation, showering and hadronization. For this PYTHIA version v6.325 was used within CMKIN framework to produce rootuple. During the generation the initial state radiation (ISR), final state radiation (FSR) and multi-parton (MPI) interactions were kept "ON" with the default values. Various input parameters used for signal and background generation are listed in Table 4.2. For event generation we have not applied any pseudorapidity cut on the photon and jet. Since the study is limited to high E_T photon and jet, the particles are usually produced in the central rapidity and hence pseudorapidity restriction is not needed. Since our aim was for an analysis with $P_T^{\gamma,jet} \geq 200$ GeV, to generate events with this requirement we used the CKIN(3) parameter($\hat{P_T}$ cut) in PYTHIA. It defines the lower limit on P_T of the outgoing partons in center of momentum frame in a $2 \rightarrow 2$ hard scattering process. To avoid any biasing in the threshold value of the analysis, the $\hat{P_T}$ values were chosen slightly lower than the $P_T^{\gamma,jet}$ thresholds. To get enough statistics for both the signal and the backgrounds, we divided the whole analysis into three phase space regions determined by the value of the P_T of the final state γ and the jet. Following $\hat{P_T}$ criteria have been used for different mass points of signal:

- $\hat{P_T} \geq 180\,\text{GeV}$(Low): $M_{q*} = 1.0$–3.0 TeV,

Parameters	**Signal**	**Backgrounds**
Subprocess	$qg \rightarrow \gamma q$ via q^* $q\bar{q} \rightarrow \gamma g$ via q^*	MSEL=1 (QCD Jets) MSEL=14, 29, 115 (SM $\gamma + jet$) MSEL=19, 20 ($W/Z(\rightarrow jj) + \gamma$)
$\sqrt{s}$	14 TeV	14 TeV
Q^2	$\hat{s}$	$\hat{s}$
PDF used	CTEQ5L [107]	CTEQ5L
$\hat{P_T}$ Cut (CKIN(3) parameter in PYTHIA)	$\hat{P_T} \geq 180$ GeV (M_{q*} =1.0-3.0 TeV) $\hat{P_T} \geq 450$ GeV (M_{q*} =3.5-4.5 TeV) $\hat{P_T} \geq 950$ GeV (M_{q*} =4.5-6.0 TeV)	$\hat{P_T} \geq 180$, 450, 950 GeV

Table 4.2 Input parameters used in PYTHIA for event generation for signal and backgrounds in $\gamma + jet$ analysis. MSEL are the corresponding PYTHIA switches for different processes.

- $\hat{P_T} \geq 450\,\text{GeV}$(Medium): $M_{q*} = 3.5$–4.5 TeV,
- $\hat{P_T} \geq 950\,\text{GeV}$(High): $M_{q*} = 5.0$–6.0 TeV.

Here, it should be noted that categorization of "low", "medium" and "high" P_T are in a relative sense. A total of 16 signal mass points, 11 for coupling strength $f_1 = f_3 = 1.0$ (with a step size of 0.5 TeV) and 5 for $f_1 = f_3 = 0.5$ were generated. Different backgrounds were also generated in various $\hat{P_T}$ range. Figure. 4.6 shows excess of production cross section due to q^* contribution over the SM (for Compton and annihilation processes only) $\gamma + jet$ production.

Table 4.3 gives the summary of generated and preselected events in terms of cross section for $qg \rightarrow \gamma + jet$ with f_i =1. The lower numbers in brackets are for those from $q\bar{q} \rightarrow \gamma + jet$ via q^* signal. For preselection we used respectively P_T threshold of 200 GeV, 500 GeV and 1 TeV in three phase space regions(the effect of η cut to retain events in the CMS fiducial volume will be discussed in the next chapter). A similar statistics is used for generation of other signal mass points. In Table 4.4 we show the corresponding

$M_{q^*} = \Lambda$ **(TeV)**	$\hat{P_T}$ **(GeV)**	σ **generated (in** pb**)**	σ **preselected (in** pb**)**	**Events Analysed**
1.0	≥ 180	67.29 (9.04)	36.64 (3.92)	5×10^5 (2×10^5)
4.0	≥ 450	1.02 (2.29×10^{-1})	0.45 (8.99×10^{-2})	8×10^5 (2×10^5)
5.0	≥ 950	1.87×10^{-2} (5.59×10^{-3})	1.02×10^{-2} (2.52×10^{-3})	6×10^5 (2×10^5)

Table 4.3 The cross-section for generated and preselected events, and the number of events analyzed for Compton(annihilation) process.

summary for background events for low P_T ($\hat{P_T} \geq 180GeV$). The change in cross section with increasing P_T for photon and jet for different backgrounds is shown in Table 4.5. It should be noted here that with increase in $\hat{P_T}$ the contribution from $q\bar{q} \rightarrow \gamma + jet$ increases to total single direct photon background. For $W/Z + \gamma$ cross-section, branching fraction for $W/Z \rightarrow jj$ have been taken into account.

4.4.1 Smearing Effect

While a detailed and full-scale detector simulation is beyond the scope of this work, realistic detector effects can easily be approximated. To this end, we smear the generator level information with ECAL and HCAL resolutions of the CMS detector. For ECAL we use the resolution function as mentioned previously and the resolutions for $\Delta\eta$ and $\Delta\phi$ were taken to be 0.02 and 0.001 respectively for both the barrel and endcaps. For the hadronic calorimeter, the resolutions were once again assumed to be the same as those

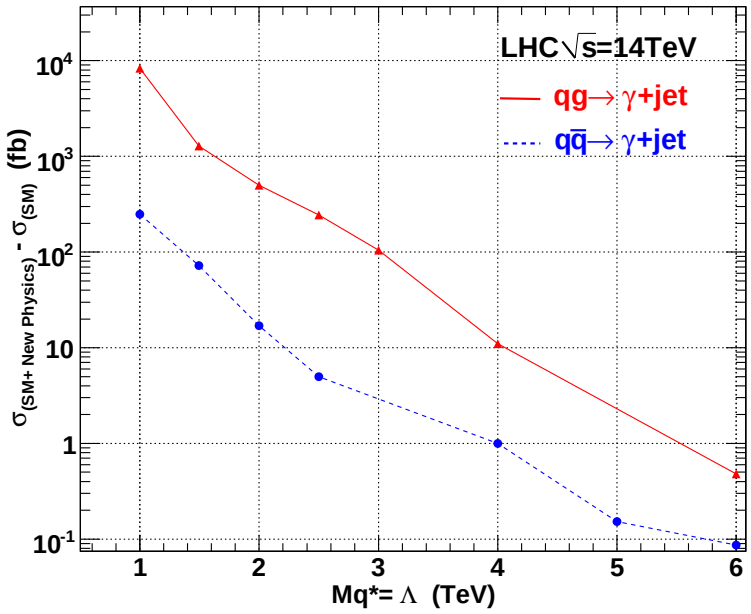

Figure 4.6 Excess of cross section over SM $\gamma + jet$ due to $q^* \rightarrow \gamma + jet$ for $Mq^*(= \Lambda)$ at $\sqrt{s} = 14$ TeV. Only Compton and annihilation diagrams have been taken into account.

Processs	$\hat{P_T}$ **(GeV)**	σ **generated (in** pb**)**	σ **preselected (in** pb**)**	**Events Analysed**
QCD dijet	≥ 180	74770	657.91	404761
$qg \rightarrow \gamma q$	≥ 180	58.96	28.52	241853
$q\bar{q} \rightarrow \gamma g$		8.79	3.72	211808
$gg \rightarrow \gamma g$		5.43×10^{-3}	1.71	157868
$Z(\rightarrow jj) + \gamma$	≥ 180	1.47×10^{-1}	0.58	197137
$W(\rightarrow jj) + \gamma$		1.08×10^{-1}	0.44	203203

Table 4.4 The cross sections for generation, pre-selection and the number of events analyzed for various backgrounds with $\hat{P_T} \geq 180$ GeV. Events were similarly generated with $\hat{P_T} \geq 450$ and 950 GeV.

Process	**50-100 GeV (pb)**	**100-200 GeV (pb)**	**200-400 GeV (pb)**	**400-600 GeV (pb)**	**600-1000 GeV (pb)**	**1000-1500 GeV (pb)**	**> 1500 GeV (pb)**
$qg \to \gamma q$	7.22×10^3	569	36.3	1.53	2.22×10^{-1}	1.19×10^{-2}	7.6×10^{-4}
$q\bar{q} \to \gamma g$	652	65.3	5.56	3.18×10^{-1}	5.67×10^{-2}	3.76×10^{-3}	2.8×10^{-4}
$gg \to \gamma g$	1.79	8.6×10^{-2}	3.1×10^{-3}	7.04×10^{-5}	6.32×10^{-6}	1.75×10^{-7}	5.8×10^{-9}
QCD Jet	1.71×10^7	9.70×10^5	4.44×10^4	1.39×10^3	171	8.19	5.34×10^{-1}
$^1Z(jj) + \gamma$	5.08	8.49×10^{-1}	9.50×10^{-2}	6.23×10^{-3}	1.16×10^{-3}	8.48×10^{-5}	6.46×10^{-6}
$^1W(jj) + \gamma$	4.80	6.93×10^{-1}	6.19×10^{-2}	4.16×10^{-3}	7.39×10^{-4}	4.67×10^{-5}	2.99×10^{-6}

Table 4.5 Production cross section in different $\hat{P}_T$ bins for various SM backgrounds with $\gamma + Jet$ final state.

for the CMS HCAL [76, 108][3], namely,

- Barrel:
$$\frac{\Delta E}{E} = \frac{65\%}{\sqrt{E/\,\mathrm{GeV}}} \oplus 5\%, \Delta\eta = 0.04, \Delta\phi = 0.02$$
- Endcaps:
$$\frac{\Delta E}{E} = \frac{83\%}{\sqrt{E/\,\mathrm{GeV}}} \oplus 5\%, \Delta\eta = 0.03, \Delta\phi = 0.02$$
- Forward regions:
$$\frac{\Delta E}{E} = \frac{100\%}{\sqrt{E/\,\mathrm{GeV}}} \oplus 5\%, \Delta\eta = 0.04, \Delta\phi = 0.04\ .$$

The 4-momentum of the photon and jet are recalculated after applying these resolution effects using an appropriate Gaussian smeared function. In Fig. 4.7, we show the effect of resolution on the mass peak for a M_{q^*} of 1 TeV. Here it should be pointed out that in the energy resolution of jet the constant term of $\sim$5% is the dominating contributor

[3]Ref. [108] is an internal document of the CMS collaboration and hence not available for outside community.

for energetic jets, which is indeed the case here. So even after smearing the effect does not look so profound.

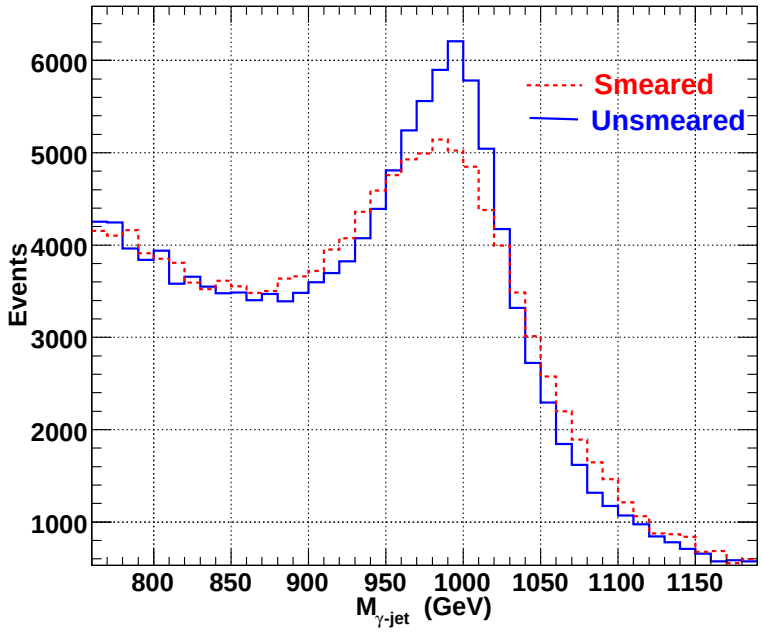

Figure 4.7 Effect of smearing on the mass bump of an excited quark of 1 TeV.

4.5 Events Generation for $\gamma\gamma$ Analysis

For this analysis the signal comprises of $q\bar{q} \rightarrow \gamma\gamma$. Like the $\gamma + jet$ resonance signal, here too the calculated matrix elements were incorporated inside PYTHIA. The input parameters used to generate these events are shown in Table 4.6. In view of the fact that the signal events preferentially populate the large transverse momentum part of the phase space, events were generated with $\hat{P}_T \geq 190$ GeV and $|\eta| < 2.7$ respectively. The final η of the reconstructed photon could be slightly different from the generated one because of steps such as ISR, FSR evolution in an event and due to photon formation algorithm and smearing effects. Since we place a final requirements of η^{γ} $\leq$2.5, this

Parameters	**Signal**	**Backgrounds**
Subprocess	$q\bar{q} \rightarrow \gamma\gamma$ via q^*	MSEL=18, 114(SM $\gamma\gamma$) MSEL=14, 29, 115 (SM $\gamma + jet$)
$\sqrt{s}$	14 TeV	14 TeV
Q^2	$\hat{s}$	$\hat{s}$
PDF used	CTEQ5L	CTEQ5L
$\hat{P_T}$ Cut (CKIN(3) parameter in PYTHIA)	$\hat{P_T} \geq 190$ GeV	$\hat{P_T} \geq 190$ GeV

Table 4.6 Input parameters used in PYTHIA for event generation for signal and backgrounds for $\gamma\gamma$ analysis.

does not bias our analysis. Although the η coverage of ECAL in CMS detector extends upto η =3.0, the photon can only be distinguished from electron (due to vertex detector and preshower coverage) upto η <2.5. Hence we restricted our study to this region. Requiring certain cut on η for generation also rids us of a very large fraction of the SM background events which, understandably, are peaked at small angles or are of small transverse momenta. For complete analysis more than 120 signal points were generated in $\Lambda - M_{q^*}$ plane. For each point a 50 K trial was used for event generation in PYTHIA. In Table 4.7 we have presented the generated and preselected cross sections along with the events analysed for few mass points. Figure 4.8 shows deviation in cross section from $q\bar{q} \rightarrow \gamma\gamma$(SM) with Λ for different values of M_{q*}. Clearly, the variation is well-approximated by a Λ^{-2} contribution superimposed upon a constant(the SM value). This is reflective of the fact that, for large Λ, new physics contribution is dominated by the interference term in eq.(2.11) rather than the pure Λ^{-4} term. If we had imposed harder

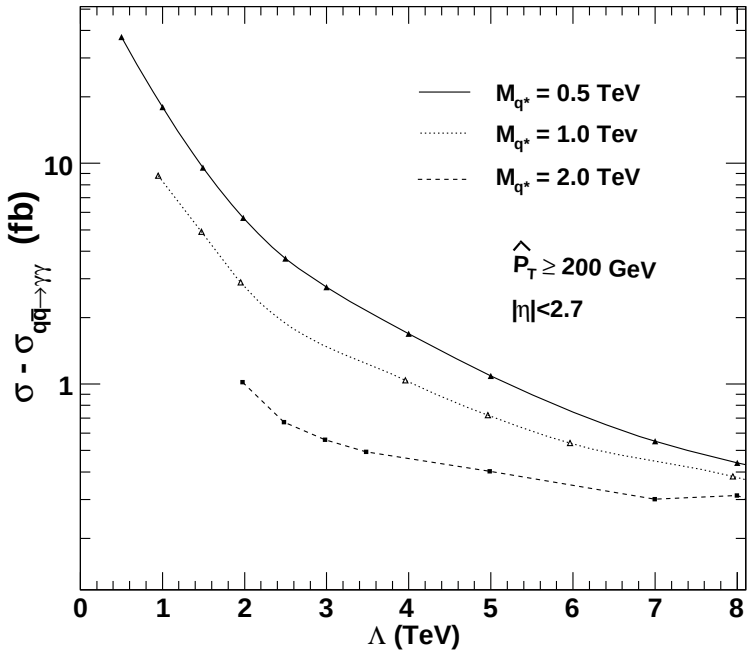

Figure 4.8 Deviation in cross section from $q\bar{q} \to \gamma\gamma$(SM) with Λ for different values of M_q^* at $\sqrt{s} = 14$ TeV

cuts on the photons, the latter term would have dominated (albeit at the cost of reducing event numbers and hence the sensitivity). For background generation a large statistics of 15×10^6 events were generated out of which 242K events with atleast two γ in the event were analyzed after preselection. Similarly large statistics was generated for SM diphoton process. Table 4.8 shows various SM production cross section for diphoton analysis along with the number of events analyzed. The preselection efficiency was found to be $\sim$ 1.5% for $\gamma + jet$ background which includes fake photon probability, and 72.9(53.1)% for $q\bar{q} \to \gamma\gamma(gg \to \gamma\gamma)$ backgrounds. For different mass points of the signal the preselection efficiency was found to be between 60-65 %. At this stage it must be noted that, in the final selection, in both the analysis we have used the fiducial volume of the electromagnetic calorimeter of the CMS detector i.e. $|\eta^\gamma| \leq$2.5 with 1.444 $\leq |\eta^\gamma| \leq$ 1.566 excluded on account of the insensitive region between the barrel and the

$M_{q^*} = \Lambda$ **(TeV)**	$\hat{P_T}$ **(GeV)**	σ **generated (in** fb**)**	σ **preselected (in** fb**)**	**Events Anaysed**
0.7		98.06	64.27	23366
1.0		85.14	54.64	23187
1.5	For all	78.76	49.70	23118
2.0	≥ 190	77.17	48.43	23173
2.5		76.45	47.79	23162
3.0		76.30	47.73	23124

Table 4.7 Cross sections for generation, preselection, and the number of events analyzed for $q\bar{q} \rightarrow \gamma\gamma$ via q^* signal. A large number of signal points(more than 120 mass points) were generated with similar statistics for the whole analysis.

Process	$\hat{P_T}$ **(GeV)**	σ **generated (in** fb**)**	σ **preselected (in** fb**)**	**Events Analysed**
$\gamma + jet$	≥ 190	48970	787	241177
$q\bar{q} \rightarrow \gamma\gamma$ (Born)	≥ 190	76.05	55.51	50000
$gg \rightarrow \gamma\gamma$ (Box)	≥ 190	5.18	2.91	50000

Table 4.8 The SM background cross-sections for diphoton study with $\hat{P}_T \geq$190 GeV and $|\eta^\gamma| <$2.7 at $\sqrt{s} =$14 TeV.

endcaps [100]. For jets we restricted the study to $|\eta^{jet}| \leq 3.0$.

Chapter 5

Analysis

"Problems cannot be solved at the same level of awareness that created them."

- Albert Einstein.

In the previous chapter we have discussed event generation and the algorithms used to mimic the detector effects for photon and jet candidate formation separately for both the analysis. In this chapter we are going to describe various kinematical and isolation cuts used to extract the q^* signal with $\gamma + jet$ and $\gamma\gamma$ final states from SM backgrounds. Here, our main focuss will be on various isolation variables used for the analysis and their effects. Due to similarity in both the analysis we first present the $\gamma + jet$ analysis in detail followed by search in $\gamma\gamma$ mode with the resulting distributions.

For both these analysis it is important to separate fake photons from the true photons. For such separation to be effective one must understand the photon formation in the detector. A simple way to reconstruct a photon is by summing the energy deposited in a limited region of ECAL in $\Delta\eta - \Delta\phi$ space, given by $\Delta R \equiv \sqrt{\Delta\phi^2 + \Delta\eta^2}$ and containing most of the energy of the electromagnetic object. These electromagnetic objects are called "photon" if they fulfill certain requirements of photon identification (also called *PhotonID*) based on certain isolation criteria.

5.1 Isolation Variables

For any analysis involving direct photon(s) in the final state, the crucial part is to identify and separate the *real* hard photon(s) from the fake candidates coming from enormous QCD backgrounds. This could be based on the topological characteristics of true direct single (or double) photon, where a true hard photon is very well separated from hadronic environment. To remove events with fake photons, photons are required not to have associated charged tracks and large hadronic activities within an isolation cone of size $R_{\rm iso}$. This is implemented by requiring that the scalar/vector sum of energy/transverse momentum within $R_{\rm iso}$ in the tracking system as well as in ECAL and HCAL should be below a certain threshold. Although, in cases where photon carries most of the momentum of the fragmenting parton, a fake photon can easily mimic a real hard photon and such backgrounds could not be suppressed by just isolation requirements. For these more advance techniques such as Neural Net(NN), shower shape comparison etc. are used which are more relevant to study with full detector effects.

At Tevatron, CDF and DØ studies have used a cone based isolation algorithm with $R = 0.4$ wherein the E_T in the cone, after subtraction of photon E_T, is required to lie below a certain value. Additional criteria such as the consistency of the shower shape with a single photon shower (to separate it from $\pi^0 \rightarrow \gamma\gamma$) and the absence of matching tracks (for converted photons or tracks from associated charged hadrons due to fragmentation) have also been used. In LHC simulation studies, various tracker, ECAL and HCAL based quantities (e.g. number of tracks, scalar and vector P_T sum etc.) within a cone have been studied in detail. In the present analysis, we have tried to closely follow the isolation criteria used by earlier CMS studies [111], which are:

- Requirement on the number of tracks (N_{trk}) above a certain P_T threshold inside a cone around the photon candidate.

- Requirement on the scalar sum of transverse energy (E_{TSUM}) inside a cone around the photon. Although in a full detector simulation the E_{TSUM} is measured separately for ECAL and HCAL, while working at the generator level, we combine them into a single variable taking into account both electromagnetic and hadronic objects around the photon.

5.2 Analysis for $\gamma + jet$ production via q^*

As mentioned in chapter-4, for event generation, we have used P_T threshold requirement on leading photon and leading jet only. No pseudorapidity restrictions were applied. Figure 5.1 shows the resulting kinematical distributions of interest for the leading photon and jet with a preselection requirement of $P_T^{\gamma,jet} \geq 200$ GeV. Here the q^* state corresponds to M_{q^*} =1 TeV and f_i =1. The rise in the transverse momentum distributions of photon and jet from q^* in Fig. 5.1(a) and (b) respectively are primarily driven by the on-shell production of the q^* and, therefore, are centered slightly below $M_{q^*}/2$. Figure 5.1(c) and (d) respectively shows the pseudorapidity distribution of the leading photon and jet for signal and all the backgrounds. These distributions do not show any sensitivity for the new physics. On the other hand as evident from Fig. 5.1(e), an excess in the invariant mass ($M_{\gamma-jet}$) spectrum at M_{q^*} value of signal, would be quite prominent for even $\int L.dt$ =1 pb^{-1}. In the invariant mass distribution the t-channel ($q\bar{q}$ annihilation) contribution manifests itself in the elongation of the side bands due to its flat excess over the SM production. Although the QCD dijet background is the most dominating even after taking into account the mistagging probability, it falls very rapidly with $P_T^{\gamma/\mathrm{jet}}$. Figure 5.1(f) shows the distribution in the center of mass scattering angle given by $\cos\theta^* = \tanh[(\eta^\gamma - \eta^{jet})/2.0]$, where θ^* is the angle between the leading photon and the jet. Although $\cos\theta^*$ variable has been used in earlier experimental studies to put bounds on Λ for different models, it does not give any sensitivity in our case. The

major discriminating variables between the signal and backgrounds are P_T^{γ}, P_T^{jet} and the invariant mass distribution of photon and jet. Other variables do not give any handle in separating signal from the backgrounds. Figure 5.2 shows similar distributions as in Fig. 5.1 but for the $M_{q^*} = 5$ TeV. For these distributions we require $P_T^{\gamma,jet} \geq 1$ TeV at the pre-selection level. Since the P_T^{γ} spectrum from the QCD background falls very rapidly, the signal dominates the background for $P_T^{\gamma} \geq 2$ TeV even without isolation cuts. For the corresponding invariant mass ($M_{\gamma-jet}$) distribution (see Fig. 5.2(e)) a combination of the large natural width and smearing effects result in a broad bump rather than a sharp one. Once again, other distributions do not discriminate between the signal and the backgrounds in any forceful manner. One of the interesting features to be noted in Fig. 5.2(c) is an obvious dip in η^{γ} spectrum for $W + \gamma$ events. This is discussed in the next section.

5.2.1 "Dip" in η^{γ} for $W + \gamma$

While the slight dip in the central η^{γ} region for the $W+\gamma$ process might seem intriguing, especially in the absence of such a dip in the $Z + \gamma$ distribution (being quite similar processes), it is but a straightforward reflection of the well-known Radiation-Amplitude-Zero(RAZ) effect in the former [112, 113]. That the RAZ in the angular distribution is apparent only for the high $P_T^{\gamma,jet}$ cutoff case can be understood by realizing that the rapidity of the photon as measured in the laboratory can be related to the rapidity (scattering angle) in the partonic subprocess center of mass frame through

$$\eta(\gamma) = \frac{1}{2} ln \left(\frac{x_1}{x_2} \right) + \eta^*(\gamma)$$

where x_i are the momentum fractions of the incoming partons. For small $\hat{s}$(hence lower CKIN(3) cuts) the parton densities are maximized when the (anti-)quark acquire small(large) momentum fractions respectively. This leads to a considerably large contri-

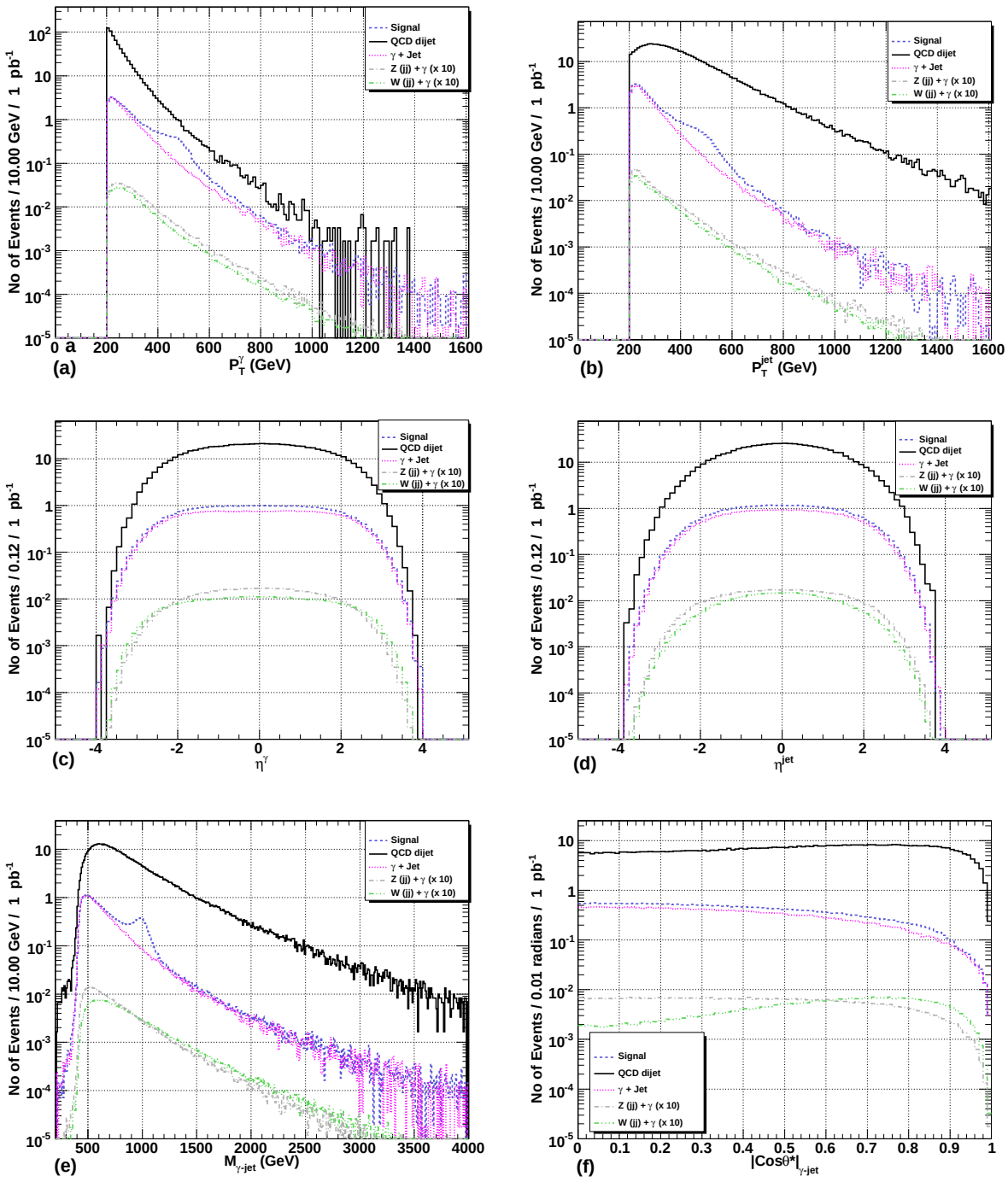

Figure 5.1 Kinematic variable distributions with a preselection requirement of $P_T^{\gamma,jet} \geq$ 200 GeV (a) P_T^{γ} distribution (b) P_T^{jet} distribution (c) η^{γ} distribution (d) η^{jet} distribution (e) $M_{\gamma-jet}$ distribution and (f)$|\cos\theta^*|_{\gamma-jet}$. The signal corresponds to $M_{q^*} = 1\,\text{TeV}$. In these figures the contributions from $W/Z + \gamma$ have been scaled up by a factor of 10 for better visibility

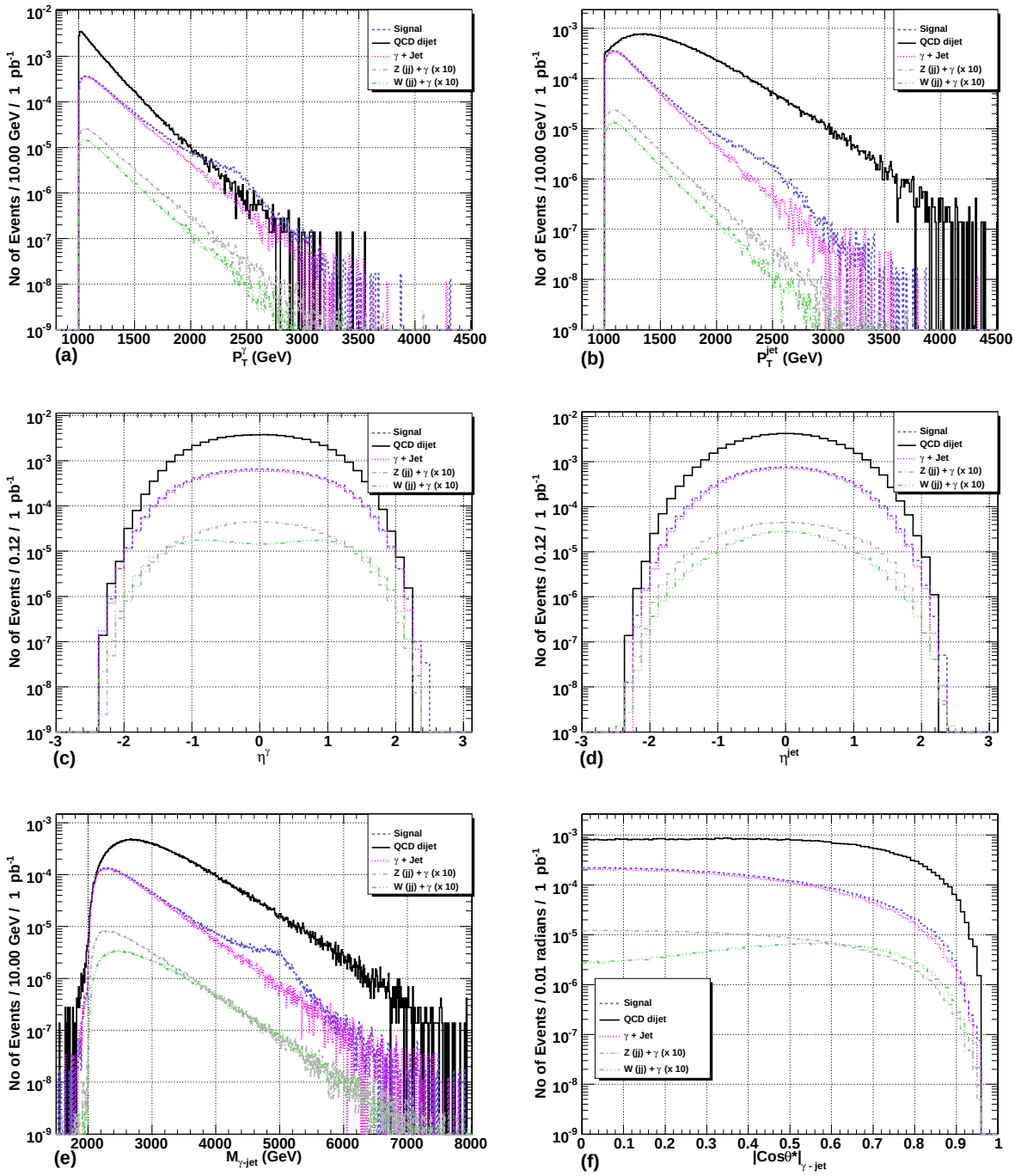

Figure 5.2 As in Fig.5.1 but for a signal corresponding to $M_{q^*} = 5\,\text{TeV}$ with preselection requirement of $P_T^{\gamma,jet} \geq 1$ TeV.

bution to η^γ from the boost, thereby smearing the original double peaked η^γ distribution into centrally peaked one. On the contrary, for typically high $\hat{s}$ (CKIN(3)$\gtrsim$ 1 TeV) the x_i's tend to be not too different thereby reducing the smearing on this account and hence retaining the originally double peak distributions of η^γ.

5.2.2 Preselection Efficiency & Geometrical Acceptance

Table 5.1 shows the preselection efficiency and geometrical acceptance for the fiducial volume of the CMS detector for various backgrounds and M_{q^*} signal of 1, 4 and 5 TeV against the total generated events. It might appear strange that efficiency due to P_T cut is quite low (for example 48% for 1 TeV mass point), but this is mainly because a very large fraction of events are generated with $\hat{P_T} > 180$ GeV in the range of 180 GeV$< P_T <$200 GeV. The other noticeable feature is the low rejection due to geometrical coverage selection for high mass signal and background events. As these events are generated with a very high $\hat{P_T}$ threshold which produces photon and jets in the transverse direction, hence they are populated in the central region of the detector. A similar behavior is observed for other mass points in three different phase spaces. Here the efficiency due to η selection is cumulative to those from preselection with transverse momentum cuts.

Table 5.1 also shows the statistical uncertainties for the above mentioned efficiencies. The statistical errors reported are calculated against the total generated events. If the total generated events are N_{gen} and the selected events are N_{sel} then the selection efficiency is simply given by $\varepsilon = \frac{N_{sel}}{N_{gen}}$. The statistical error on ε is given by:

$$(\delta\varepsilon)^2 = \left(\frac{\partial\varepsilon}{\partial N_{sel}}\right)^2 (\delta N_{sel})^2 + \left(\frac{\partial\varepsilon}{\partial N_{gen}}\right)^2 (\delta N_{gen})^2 \tag{5.1}$$

Selection Cut	Signal[4] %	$\gamma + Jet$ %	QCD %	$Z + \gamma$ %	$W + \gamma$ %
$P_T^{\gamma,jet} \geq 200GeV$	48.7 ±0.075 [1 TeV]	44.2 ±0.094	0.90 ±0.014	38.4 ±0.088	37.1 ±0.086
$P_T^{\gamma,jet} \geq 500GeV$	40.2 ±0.055 [4 TeV]	39.8 ±0.089	0.42 ±0.007	50.4 ± 0.10	50.6 ±0.101
$P_T^{\gamma,jet} \geq 1TeV$	47.4 ±0.073 [5 TeV]	46.0 ±0.096	0.51 ±0.008	58.8 ±0.11	59.9 ±0.109
$\|\eta^{\gamma}\| \leq 2.5$, $\|\eta^{jet}\| \leq 3.0$, $\|\eta^{\gamma}\| \notin [1.4442, 1.5666]$	42.4 ± 0.070 [1 TeV]	38.2 ±0.088	0.81 ±0.013	32.8 ±0.081	33.2 ±0.082
	38.2 ±0.055 [4 TeV]	37.8 ±0.083	0.40 ±0.007	47.4 ±0.097	48.4 ±0.098
	46.4 ±0.073 [5 TeV]	45.0 ±0.073	0.50 ±0.008	56.3 ±0.11	58.7 ±0.108

Table 5.1 Preselection efficiency and geometrical acceptance along with statistical error for various SM backgrounds and few signal points.($Note^4$: Here the SM $\gamma + jet$ production is included in the signal.)

As δN_{gen} =0, hence the above form reduces to,

$$\delta\varepsilon = \frac{1}{N_{gen}}\delta N_{sel} \tag{5.2}$$

$$\delta\varepsilon = \frac{\sqrt{N_{sel}}}{N_{gen}} = \sqrt{\frac{\varepsilon}{N_{gen}}} \tag{5.3}$$

In this analysis the mentioned statistical uncertainties against total generated events for various quantities are estimated in a similar way. In most of the cases the statistical error is found to be less than 0.3%.

5.2.3 Track Isolation

For track isolation study we have considered only 'stable' charged particles e.g. $\pi^{\pm}$, $K^{\pm}$, $e^{\pm}$ and $P^{\pm}$ which also contribute major fraction of charged tracks in an event. The

other particles are found to have negligible contribution. Indeed, $\pi^{\pm}$ alone contributes more than 80% of the charged tracks. Figure 5.3 shows a distribution of number of charged tracks (N_{trk}) around the leading photon in a cone of size $\Delta R \leq 0.35$ for a signal of $M_{q^*} = 1$ TeV and for the total background. Since the leading photon is the *true* photon for signal events, most of them are associated with zero tracks (N_{trk} =0) and the distribution falls off very rapidly for larger N_{trk} values. For background events though, the distribution peaks at N_{trk} ∼7-8 and then falls slowly. The small rise at $N_{trk} = 0$ is due to the fact that $\gamma + jet$(SM) and $W/Z + \gamma$ backgrounds have true photons as the leading photon in the event and have no tracks around them, while the rising part along with the extended tail is mainly contributed by the QCD dijet events where the fake photon typically has a large number of tracks associated with it.

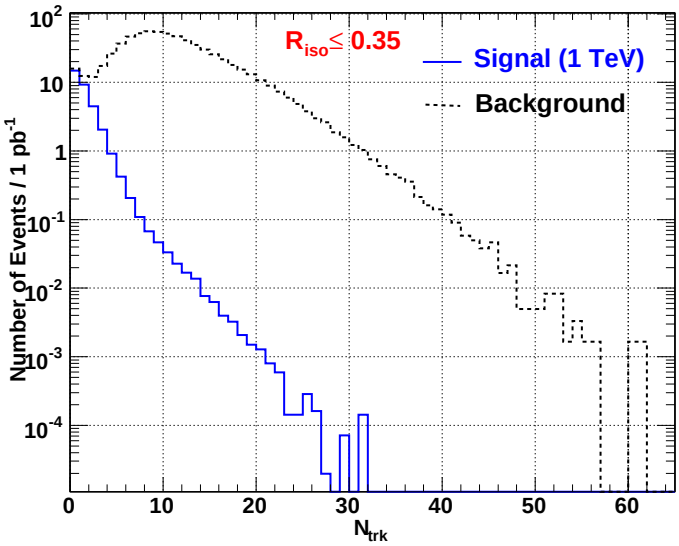

Figure 5.3 Number of tracks(N_{trk}) around the photon for the signal (M_{q^*} =1 TeV) and the background events.

In *pp* collision at the LHC, a large number of soft tracks (in the range of a few MeVs to a few GeVs) will be produced in each event. The main sources of such soft tracks are ISR, FSR, minimum bias and underlying events. For a direct photon emerging from the

hard interaction, such soft tracks could actually be in the near vicinity of the photon. Labeling such photons as non-isolated could potentially reduce the signal efficiency, and many interesting events, such as those in this study, could be lost. To prevent such losses, the tracks are usually required to pass a certain minimum selection criteria, with the requirement on minimum transverse momentum threshold as a common practice [99, 111, 114]. Adopting this strategy, we investigate the dependence of the signal efficiency and the signal/background (S/B) ratio on the chosen P_T threshold (P_{Tmin}^{trk}), varying the latter between 1-3 GeV [99]. To optimize the value of P_{Tmin}^{trk}, it is useful to examine both

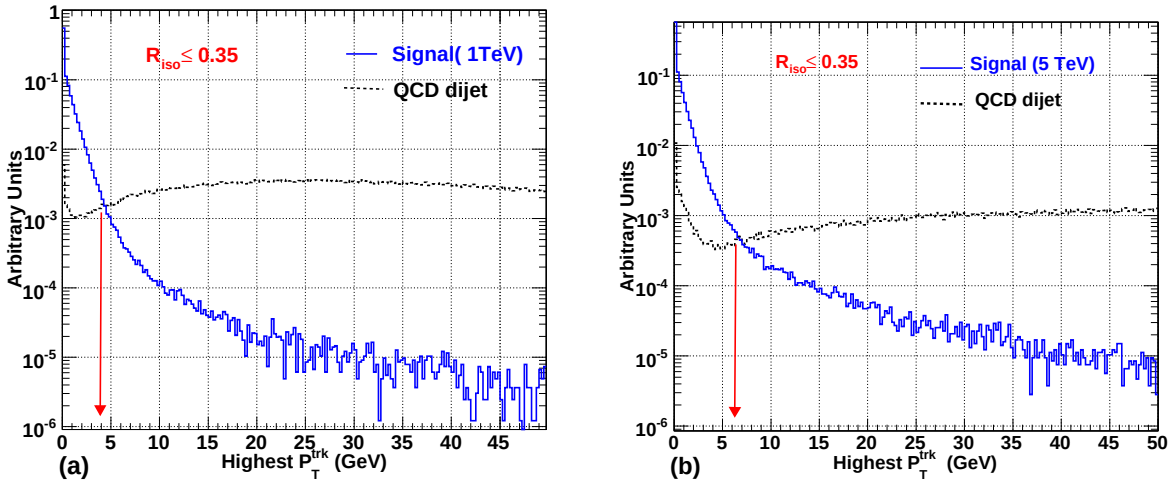

Figure 5.4 Highest P_T track around the leading photon for the signal and the QCD background a) M_{q^*} =1 TeV b) M_{q^*} =5 TeV. An isolation cone of size R =0.35 has been used. The distributions are normalized to unity. Note that shape of the background differs between the two panels on account of differing requirements on $\hat{P}_T$(vide chapter-4.)

the signal and the QCD dijet background in terms of the distribution for the highest-P_T track inside an isolation cone. In Fig 5.4(a) and (b) respectively, we display this distribution for the signal for M_{q^*} = 1 TeV and 5 TeV. Accompanying these, in each case, are the corresponding QCD dijet background. For the sake of comparison both the distributions have been normalized to unity. It is evident that tracks accompanying signal photon tend to have lower P_T, whereas for background photons, the distribution

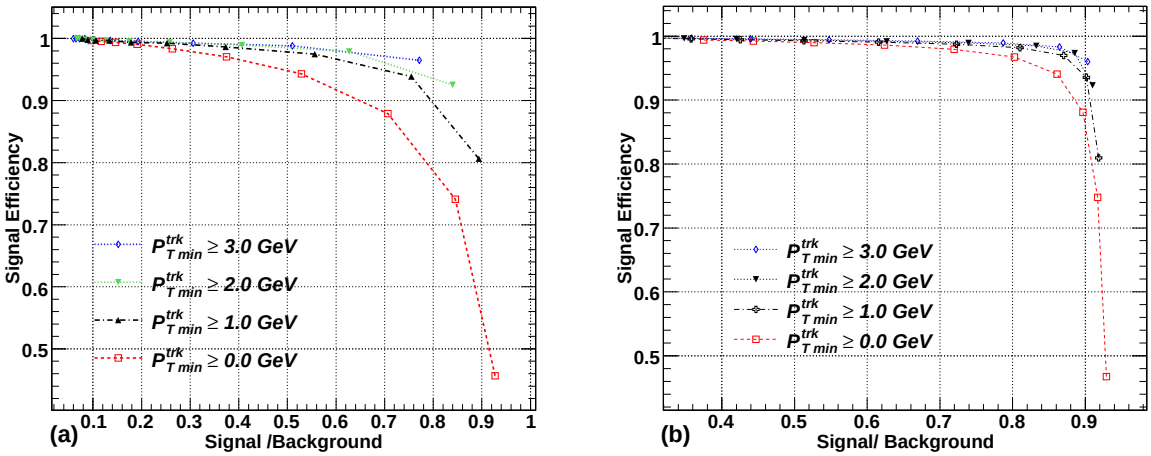

Figure 5.5 Effect of P^{trk}_{Tmin} requirement on signal efficiency vs S/B for the photons from a) 1 TeV signal b) 5 TeV signal. For a given threshold (P^{trk}_{Tmin}), the individual points correspond to differing values of the number of tracks, N_{trk}, allowed in a cone starting with 0 tracks (for the rightmost point) and increasing in steps of one.

is very broad one. An indication for the choice of optimal value of P^{trk}_{Tmin} is given by the point of intersection of the two normalized distributions (signal and background). The optimal choice does depend on the signal profile (determined, in a large measure by the typical momentum transfer in the collision), as evident from the crossover points being ∼4 (6) GeV for signals corresponding to M_{q^*} of 1 (5) TeV. Thus, characterizing only those tracks, around a photon, with a $P_T \gtrsim 4\,\mathrm{GeV}$ as true tracks (or, in other words, accepting photons with accompanying tracks satisfying $P_T \leq P^{trk}_{Tmin} \sim 4\,\mathrm{GeV}$ as true photons) would mean that a very large fraction of the signal is retained while a significant fraction of the background is rejected. In this study, we accept a photon to be an isolated one if there is no track with minimum transverse momentum (P^{trk}_{Tmin}) within a given isolation cone. It should be noted that comparative distributions of signal and total background, as shown in Fig. 5.3 are with P^{trk}_{Tmin} =0, and is not overly sensitive to moderate changes in the P^{trk}_{Tmin} value.

In Fig. 5.5, we display the consequent interplay between signal efficiency and the signal to background ratio (S/B) as a function of P^{trk}_{Tmin}, for two different signal points

(M_{q^*} =1 TeV and 5 TeV) belonging to different phase space region. It is evident from the distributions that adopting a higher threshold would remarkably increase the signal efficiency with only a small loss in the S/B ratio. More importantly, the track isolation requirement reduces the fake photon events with its major effect showing up in the QCD dijet background. It is obvious that a strict requirement of $N_{trk} = 0$ with P^{trk}_{Tmin} >some minimum value in a given cone around the photon reduces only a small fraction of the signal whereas the S/B ratio is improved considerably.

To keep the analysis simple and uniform for all the signal mass points, we have dispensed with a M_{q^*}-dependent choice of the threshold, and instead demand $P^{trk}_{Tmin} \geq 3$ GeV and $N_{trk} = 0$ irrespective of the mass of the q^* being searched for or in other words we put more emphasis on those points which could be accessible with early data. Although a choice of $P^{trk}_{Tmin} \geq 4$ GeV would have led to better result, we make a conservative choice to account for the fact that, in a real detector, the tracking efficiency is usually less than 100%.

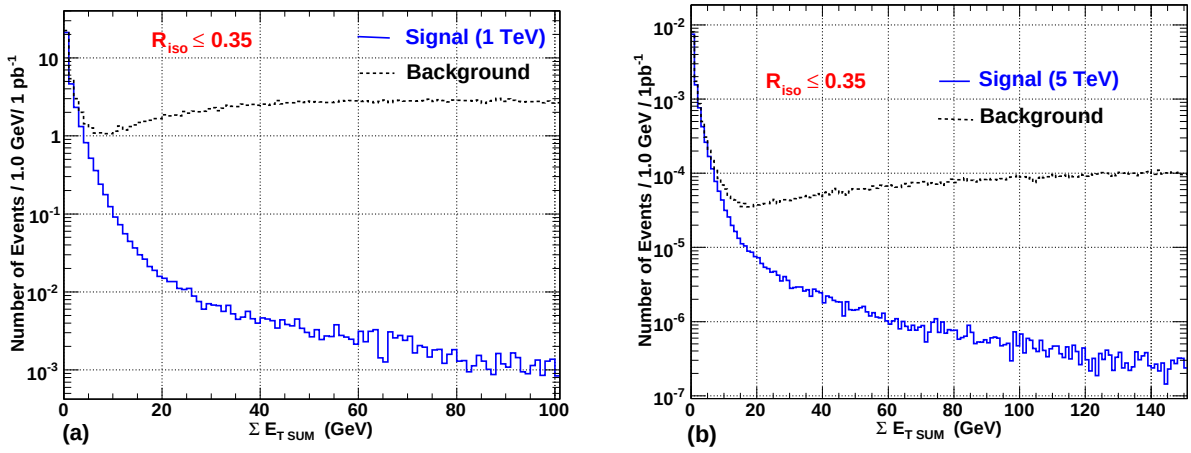

Figure 5.6 E_{TSUM} around the photon for signal and background events for a) M_{q^*} =1 TeV b) M_{q^*} =5 TeV signal. Distributions are normalized for $\int Ldt$ =1 pb^{-1}.

5.2.4 E_T Sum Isolation

We now discuss the next isolation variable, namely the scalar sum of transverse energy inside a cone around the photon candidate. Here, the E_{TSUM} is the combined scalar sum of transverse energy of the electromagnetic and hadronic particles around the photon candidate inside an isolation cone. Figure 5.6a(b) show respectively the E_{TSUM} distribution for the leading photon for $M_{q^*} = 1\,(5)\,\text{TeV}$ for an isolation cone of size $\Delta R = 0.35$. Both these distributions have been normalized for an integrated luminosity of 1 pb^{-1}. It is evident that, in either case, a large fraction of signal events have $E_{TSUM} \leq 5.0\,\text{GeV}$ whereas the background events generically have $E_{TSUM} \geq 5\,\text{GeV}$. For $M_{q^*} = 5\,\text{TeV}$, the discriminating point is slightly higher. Similar to previous subsection, we study the dependence of signal efficiency and S/B ratio on the choice of cone size and E_{TSUM} threshold.

Figure 5.7(a) and (b) respectively show the signal efficiency vs. S/B ratio for different cone sizes and for 1 TeV and 5 TeV signal points. It is evident that, for a given signal efficiency, a higher S/B ratio can be attained for larger cone sizes. For example, requiring E_{TSUM} >5 GeV for $\Delta R \leq$0.35 leads to a large signal efficiency ($\sim 92\%$) and $S/B > 0.88$ for either choices of M_{q^*}. On the other hand, any relaxation beyond $E_{TSUM} > 5.0\,\text{GeV}$ reduces S/B considerably with only a very small gain in signal efficiency. Several E_{TSUM} thresholds for different cone sizes are analyzed along with track isolation requirements to chose a better signal efficiency along with the S/B ratio.

5.2.5 Selection Cuts

In Table 5.2, we show the efficiencies for signal and backgrounds for different isolation variables with varying thresholds. Since we aim to observe any excess as a mass peak over the SM continuum and, in the early phase of the LHC operation, would be able to identify a signal only for low masses, it is rather important to have a large signal efficiency

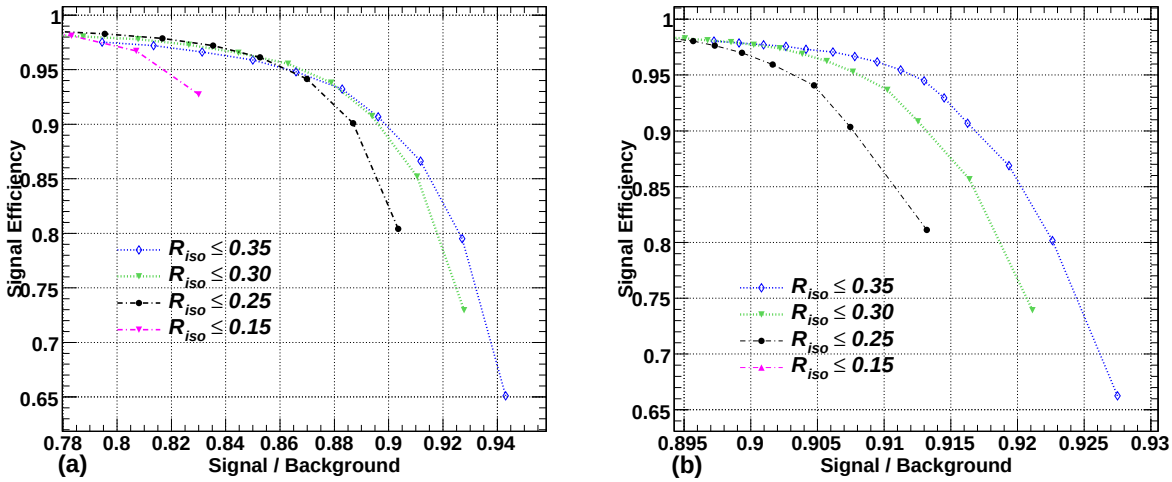

Figure 5.7 Signal efficiency vs. S/B ratio for different cone sizes for different choices of the E_{TSUM} threshold around the leading photon for (a) M_{q^*} =1 TeV and (b) M_{q^*} = 5 TeV. For each choice of the cone size, individual points correspond to a particular choice for the E_{TSUM} threshold in that cone, starting with 1 GeV at the rightmost point and going up in steps of 1 GeV.

and S/B ratio for smaller M_{q^*}. Hence we have used the isolation criteria befitting a 1 TeV signal point, and performed this analysis for all the signal points considered in this study. Note that, while it is indeed possible to have yet other criteria to select different threshold based on real detector simulation, the qualitative differences in the results are small.

Based on these studies, the final selection cuts applied are as follows (the $P_T^{\gamma,jet}$ requirements being determined by the range of M_{q^*} being investigated, vide chapter-4):

- P_T^{γ}, $P_T^{jet} \geq 200$ GeV(500 GeV, 1 TeV);
- $|\eta^{\gamma}| \leq 2.5 \quad \& \quad |\eta^{\gamma}| \notin [1.4442, 1.5666]$;
- $|\eta^{jet}| \leq 3.0$;
- $N_{trk} = 0$ for $P_T^{trk} \geq 3.0$ GeV within $R_{iso} \leq 0.35$;
- $E_{TSUM} < 5.0$ GeV within $R_{iso} \leq 0.35$.

R_{iso}	N_{trk}	P_{Tmin}^{trk} (GeV)	E_{TSUM}^{max} (GeV)	S[5] (%)	QCD (%)	$\gamma + Jet$ (%)	$Z + \gamma$ (%)	$W + \gamma$ (%)	(S/B)
				$M_{q^*} = 1.0$ TeV					
0.30	0	1.0	5.0	73.6±0.13	0.93±0.014	72.9±0.18	75.0±0.20	71.9±0.19	0.970
			6.0	73.7±0.13	0.94±0.014	73.1±0.18	75.1±0.20	72.0±0.19	0.967
		2.0	5.0	81.2±0.14	1.12±0.016	80.6±0.19	82.9±0.21	79.4±0.20	0.951
			6.0	81.7±0.14	1.15±0.016	81.0±0.19	83.3±0.21	79.9±0.20	0.946
		3.0	5.0	83.0±0.14	1.19±0.016	82.3±0.19	84.8±0.21	81.2±0.21	0.941
			6.0	83.7±0.14	1.25±0.017	83.1±0.19	85.6±0.22	81.9±0.21	0.930
0.35	0	1.0	5.0	69.8±0.13	0.82±0.014	69.3±0.18	71.1±0.19	68.2±0.19	0.984
			6.0	70.1±0.13	0.83±0.014	69.5±0.18	71.4±0.19	68.5±0.19	0.982
		2.0	5.0	79.0±0.14	1.01±0.016	78.4±0.19	80.5±0.21	77.2±0.20	0.967
			6.0	79.8±0.14	1.05±0.016	79.1±0.19	81.4±0.21	78.0±0.20	0.960
		3.0	5.0	81.0±0.14	1.08±0.016	80.4±0.19	82.6±0.21	79.2±0.20	0.957
			6.0	82.2±0.14	1.14±0.17	81.6±0.19	83.9±0.21	80.4±0.21	0.947
				$M_{q^*} = 5.0$ TeV					
0.30	0	1.0	5.0	82.9±0.15	1.82±0.020	83.1±0.19	83.3±0.17	81.6±0.17	0.955
			6.0	83.1±0.15	1.83±0.020	83.2±0.19	83.5±0.17	81.8±0.17	0.954
		2.0	5.0	91.1±0.10	2.11±0.022	91.1±0.20	91.5±0.17	89.5±0.17	0.950
			6.0	91.5±0.15	2.14±0.022	91.6±0.20	91.9±0.10	89.9±0.18	0.950
		3.0	5.0	92.9±0.15	2.17±0.022	93.0±0.20	93.4±0.18	91.3±0.18	0.949
			6.0	93.7±0.15	2.22±0.022	93.7±0.20	94.2±0.18	92.1±0.18	0.947
0.35	0	1.0	5.0	78.8±0.14	1.63±0.019	79.0±0.19	79.3±0.16	77.7±0.16	0.960
			6.0	79.0±0.10	1.64±0.019	79.2±0.19	79.5±0.16	77.9±0.16	0.960
		2.0	5.0	88.6±0.15	1.94±0.021	88.7±0.20	89.0±0.17	87.2±0.17	0.956
			6.0	89.3±0.15	1.97±0.021	89.4±0.20	89.8±0.17	87.9±0.17	0.956
		3.0	5.0	90.6±0.15	1.99±0.021	90.7±0.20	91.1±0.17	89.2±0.17	0.955
			6.0	91.9±0.15	2.04±0.021	91.9±0.20	92.4±0.18	90.5±0.18	0.954

Table 5.2 Fraction of events surviving for the signal and various backgrounds with statistical errors for different isolation cuts (after P_T Cut). ($Note^5$: Here the SM $\gamma + jet$ production is included in the signal.)

Table 5.3, shows the expected number of events for $M_{q^*} = \Lambda = 1\,\text{TeV}$ for an integrated luminosity of 100 pb^{-1} for various combinations of isolation variables discussed above.

Figure 5.8 shows the invariant mass distribution for both signal+background(S+B) and background(B) only after the all selection cuts.

5.2.6 Signal Extraction

For an analysis involving a mass peak search, one of the essential elements is to extract the peak events from the background by proper subtraction of the sidebands. We describe a procedure to estimate the number of events under the mass peak in case of a discovery (i.e. if the data supports the S+B hypothesis). Assuming an excess centered

R_{iso}	N_{trk}	P_{Tmin}^{trk} (GeV)	E_{TSUM}^{max} (GeV)	S[6]	QCD	$\gamma + Jet$	$Z + \gamma$	$W + \gamma$	Tot.Background	(S+B)
0.30	0	1.0	5.0	2734	626.2	2185	4.10	2.97	2818	3368
			6.0	2740	634.4	2190	4.11	2.98	2831	3381
		3.0	5.0	3085	803.0	2467	4.64	3.36	3278	3896
			6.0	3112	845.9	2490	4.68	3.39	3344	3966
0.35	0	1.0	5.0	2596	554.0	2076	3.89	2.82	2637	3157
			6.0	2604	560.8	2083	3.91	2.83	2650	3172
		3.0	5.0	3011	727.4	2409	4.52	3.28	3144	3747
			6.0	3054	772.1	2444	4.59	3.32	3224	3834

Table 5.3 Number of events surviving for $M_{q^*} = \Lambda$ =1 TeV signal and the backgrounds for $\int Ldt = 100\ pb^{-1}$ for different isolation cuts. ($Note$[6]: Here the SM $\gamma + jet$ production is included in the signal.)

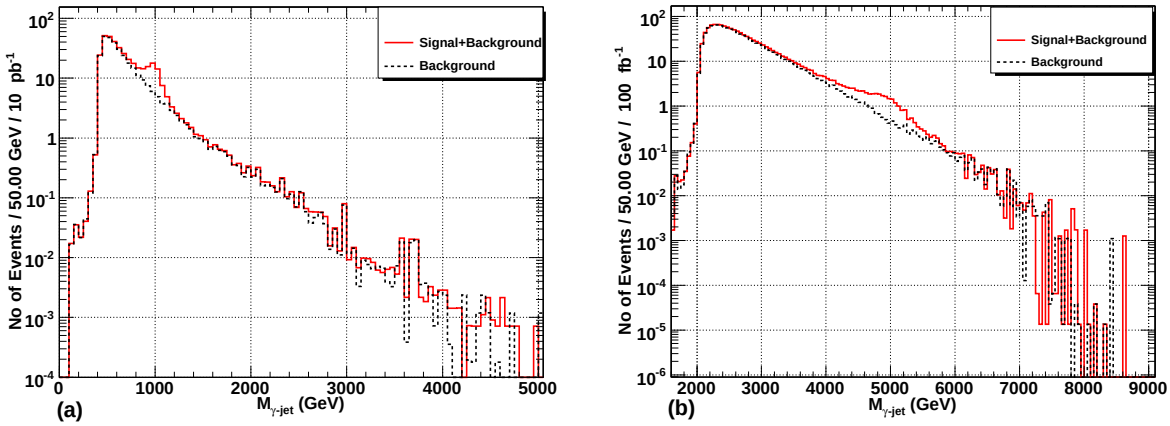

Figure 5.8 Invariant mass distribution for $\gamma-$jet system for signal+bacgkround and background only after all the isolation and kinematical cuts. (a) M_{q^*} =1 TeV (b) M_{q^*} =5 TeV.

approximately around $M_{\gamma-\text{jet}} = M_0$, the first step constitutes fitting the data over a $M_{\gamma-\text{jet}}$ range centered around M_0 but much wider than the region of the excess, the aim being to fit the background as well as the sidebands. While in a real experiment one would attempt to fit the sidebands from data alone, here we use a large MC sample to determine the shape of the sidebands and find that an exponential describes them well (see Fig. 5.9 for $M_0 = 1\,\text{TeV}$). To generate realistic distributions, we consider (s + b) events in each bin to be an independent Poisson distributed (and integer valued)

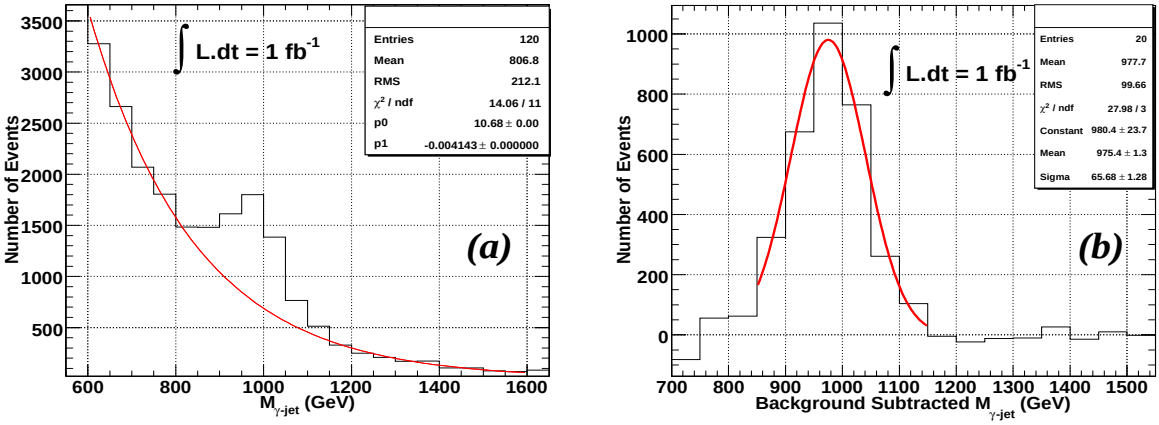

Figure 5.9 (a)Background fit on the (S+B) distribution with an exponential function for 1.0 TeV q^* for an integrated luminosity of 1 fb^{-1}. (b) Corresponding background subtracted invariant mass distribution.

variable with a mean equalling the theoretically expected number of events. A random fluctuation is then used to generate the "experimentally observed" events in the bin concerned. For a good background fit on the (S+B) distribution, an identified excess has clearly to be left out. To this end, we leave out the range $\sim [M_0 - 3\,\Gamma_0, M_0 + 3\,\Gamma_0]$ consonant with the binning algorithm where $\Gamma_0 = \Gamma(M_{q^*} = M_0)$. For a χ^2 minimization of the fit, the MINUIT [115] package was used within the *ROOT* framework [116]. The fit in Fig. 5.9(a) has been done for an integrated luminosity of 1 fb^{-1} although a 5σ signal significance for $M_{q^*} = 1\,\text{TeV}$ is attainable with only 10 pb^{-1} of data. Fig 5.9(b) shows the background subtracted mass distribution for M_{q^*} =1 TeV. Here we have used a single Gaussian to fit the mass spectrum. While an integrated luminosity of 1 fb^{-1} for new physics mass measurements would normally be considered meagre when compared to the LHC design parameters, it is interesting to consider the physics possibilities with far lower luminosities. Hence, we also extracted the mass peak events for 10 pb^{-1}, shown in Fig. 5.10. While the fit to the background is, understandably, not as good as in the earlier case, once the validity of an exponential fit is accepted, the background subtracted mass fit is still very convincing. In Fig. 5.10(b) the number of signal events under the

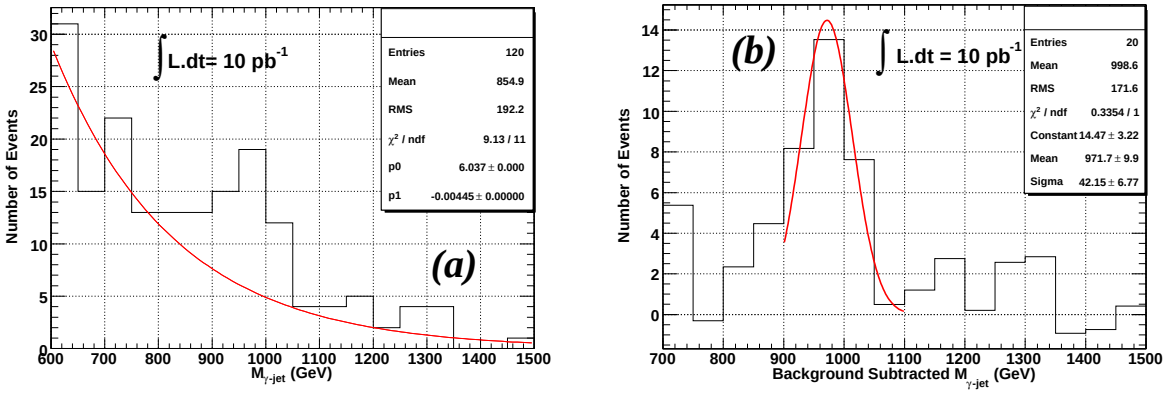

Figure 5.10 As in Fig.5.9, but for an integrated luminosity of 10 pb^{-1} only.

Gaussian fit and within the 800–1200 GeV mass range are found to be $30.5 \pm 5.5(stat.)$. The uncertainty due to error on fitting parameters are found to be at most 4.9 events. We note in passing that in an actual detector at the LHC the mass peak will have a tail on the lower mass side due to partial containment of showers and fitting this may need a Gaussian modified with a Landau or some other asymmetric distribution thereby broadening the mass peak somewhat.

The invariant mass distribution has two components, the natural Lorentzian part for an unstable particle with a large width and a Gaussian (or a double-Gaussian) distribution due to resolution effects. The combined distribution is a convolution of the two above. Although the combined distribution is thus not a simple one, a single Gaussian fits the mass peak reasonably well and hence we choose to fit the peak with a simple Gaussian.

5.3 Analysis for $\gamma\gamma$ production via q^*

The $\gamma\gamma$ final state has quite similar analysis strategy as for $q^* \rightarrow \gamma + jet$ with mainly two difference: (1) in the absence of mass peak in the $\gamma\gamma$ channel one needs to examine the complete mass range possible, and (2) since both the objects of interest in the final

state are photon hence the isolation requirement is quite important to overcome the backgrounds.

With the application of isolation criteria implying that the observed direct photon cross section is not inclusive anymore, the proper choice of isolation criteria becomes a key issue in matching observations with theoretical predictions. Since the present study searches for an excess of diphoton events over the SM prediction, this is important for us. However, this issue has been addressed in detail in the literature. Issues regarding the validity of factorization, the dependence of fragmentation functions on the isolation parameters and soft gluon divergences have been discussed in a number of papers [117, 118].

5.3.1 Track Isolation

For this analysis we have considered isolation variables(similar to previous study) for background reduction because of similar kinematical phase space and the same type of backgrounds. In addition we will discuss some extra variables for the present analysis, which could be useful for future studies.

5.3.1.1 Number of Tracks with Minimum P_T^{trk} Threshold

The distribution for the number of charged tracks with P_{Tmin}^{trk} >3.0 GeV in a cone size 0.35 pointing to either the leading photon or the second leading photon candidate are shown in Fig. 5.11. Although Fig. 5.11 shows the distribution for a particular value of P_T^{trk}, the features are generic for all values of P_T^{trk}. In the signal sample both the photon candidates are true photons and hence the distribution falls very rapidly. The situation is markedly different for the background. For a true $\gamma + jet$ event, the second leading photon is usually a fake one and has a large amount of hadronic activity around it. Consequently, the distribution (in Fig. 5.11(b)) reaches a maximum, around 5–6

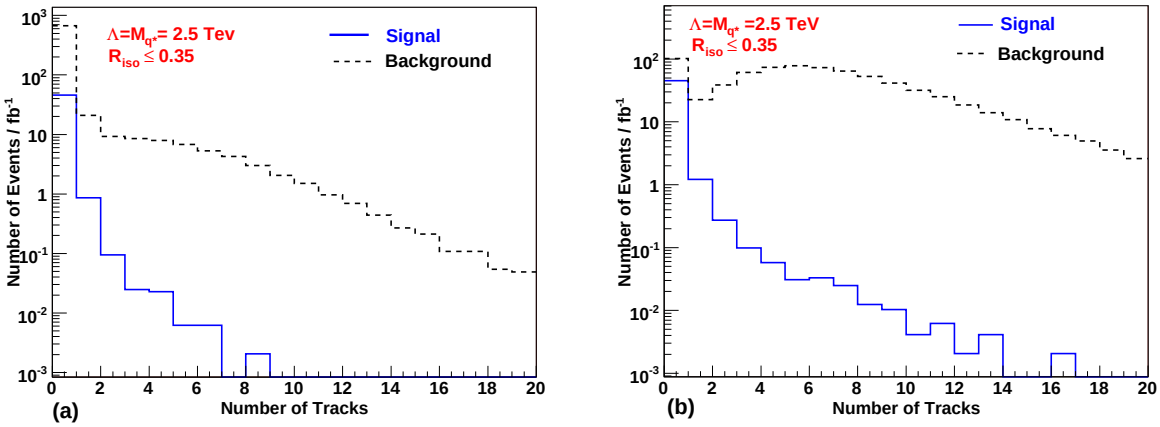

Figure 5.11 Number of tracks for the signal and the background events with $P_T^{trk} \geq 3.0$ GeV pointing to (a) leading photon and (b) second leading photon, in a cone of size 0.35.

tracks and then falls slowly. To understand the shape of the background distribution in Fig. 5.11(a), it should be realized that a small fraction of such events would actually have the fake photon as the leading one. Since such photons have a large number of tracks around them, an extended tail is seen in Fig. 5.11(a). The major source of tracks in case of a true photon are ISR, FSR and MPI, while the low-P_T^{trk} (< 1.5 GeV) tracks emanate mainly from the debris of the colliding protons. In various CMS studies P_{Tmin}^{trk} typically varies between 1-2 GeV [99].

Similar to our previous study, for this analysis too, we have considered several choices for P_{Tmin}^{trk}, viz 0.0, 1.0, 2.0 and 3.0 GeV respectively for different cone sizes. Signal efficiency and signal over background(S/B) ratio were calculated with these choices of P_{Tmin}^{trk} and various N_{trk}(number of tracks in a cone) possibilities. The results, for the second leading photon, are displayed in Fig. 5.12. It is obvious that for all values of P_{Tmin}^{trk} the signal efficiency increases(but at the cost of loss in S/B) with increase in number of tracks allowed in the cone. But as P_{Tmin}^{trk} increases the signal efficiency vs S/B is almost flat for $P_{Tmin}^{trk} \geq 3$ GeV. For N_{trk} =0 case, as P_{Tmin}^{trk} increases from 1 GeV to 3 GeV the signal efficiency increase by more than 15% with a very small reduction in S/B ratio. Understandably, neither the SM diphoton contribution (whether the Born or

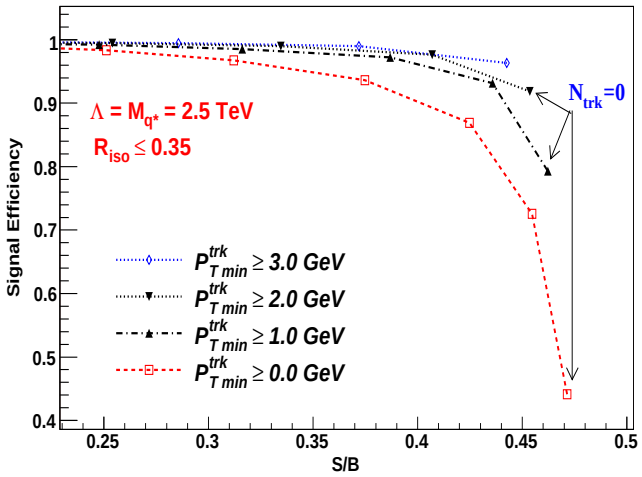

Figure 5.12 Effect of P_{Tmin}^{trk} on signal efficiency vs S/B for the second leading photon.

the box-mediated processes) nor the new physics contribution to the same are affected by the requirement of N_{trk}=0. Only the events from $\gamma + jet$ background are rejected. Fig.5.13(left) shows the corresponding distribution for the highest P_T track emanating from the second leading photon. Both the distributions (signal and $\gamma + jet$ background) have been normalized to unity. Clearly, the background dominates the signal for $P_{Tmin}^{trk} >$ 3.5 GeV, thus pointing out a means to reject a large fraction of the $\gamma + jet$ background. Only those events are accepted where neither of the photons have an associated track with P_T ≥3.0 GeV within the respective isolation cones (i.e. N_{trk}=0 for P_T^{trk} ≥3.0 GeV). Only the highest P_T track is considered because considering lower P_T tracks may affect signal efficiency as discussed previously. Since this study has been done at the generator level we have chosen P_{Tmin}^{trk} ≥3.0 GeV which is similar to $q^* \rightarrow \gamma + jet$ study.

Until now we have studied the effect of highest P_T track and number of tracks in a given cone size. The other variables found interesting but not used due to their strong correlation with variables already used in separating true photons from fake ones are:

- Nearest tracks's P_T and ΔR and

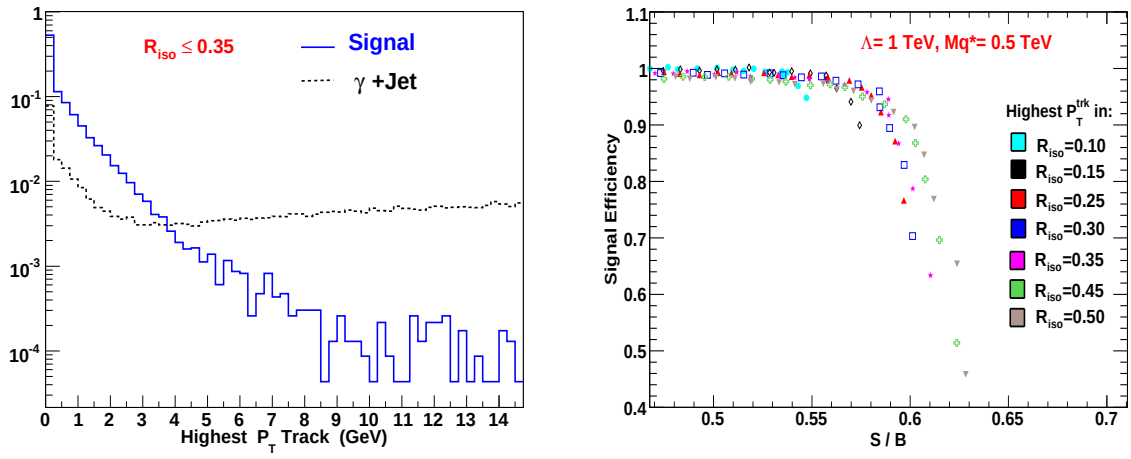

Figure 5.13 (Left)Highest P_T track profile around the second leading photon for both signal and $\gamma + jet$ background in an isolation cone of size 0.35. (Right)Variation in signal efficiency vs S/B for different isolation cone sizes and P_T^{trk}-threshold.

- $\vec{P}_T^{trk}$ sum around the photon.

We briefly discuss these two variables below.

5.3.1.2 Nearest Track's P_T and ΔR

This variable is based on different surroundings of a true hard photon and a fake photon. In Fig. 5.14(left), we show the distribution for P_T of the nearest track for both the background and the signal for the mass point with Λ =1.0 TeV and M_{q^*} =0.5 TeV. For these distributions no P_{Tmin}^{trk} threshold was applied. Hence the background has a large number of near soft tracks($P_T^{trk} < 2GeV$). It should be noted that for signal those events are also plotted in Fig. 5.14(left) which does not have any track around the photon and they contribute to the first P_T bin. As visible the signal spectrum fall very rapidly while the background behaves completely different. In a true photon case the nearby tracks are usually from the hadronization of a gluon emitted as ISR or from the debris of underlying and minimum bias events. Hence their distance (in $\eta - \phi$) is quite large for true photon compared to fake ones. Figure 5.14(right) shows ΔR of the

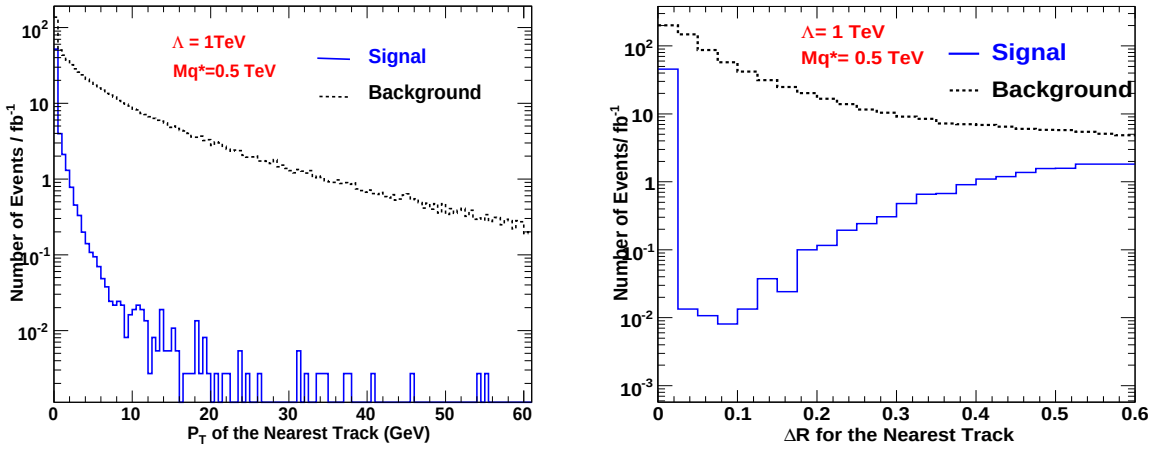

Figure 5.14 (Left) The transverse momentum of the nearest track and (Right) ΔR of the nearest track around the second leading photon for the signal and background.

nearest track from the photon in case of signal and background. The first bin for the signal has very large entry because of the fact that most of the events do not have any track (hence $\Delta R = 0.0$ is plotted here). For next few bins there are some events where the tracks are quite close to photon and with increase in ΔR the spectrum rises again as tracks from other source are associated with photon for large ΔR. For background large number of tracks in small cone size are expected around photon candidates and this decreases as ΔR increases as most of them are from the same parton after hadronization. Since the SM $\gamma\gamma$ production has a similar profile as signal, hence it adds to the later bins of the background distribution resulting in a slow falling distribution for the overall background.

Figure 5.15 shows signal efficiency vs S/B profile for first few nearest tracks for the two quantities discussed above. Figure 5.15(left) shows that for the 1^{st} nearest track these variables give the best optimization of signal efficiency for a given S/B ratio. For ΔR of the nearest tracks, the signal efficiency vs S/B profile is drawn by starting with ΔR =0.6 and than decreasing it in a step of 0.025.

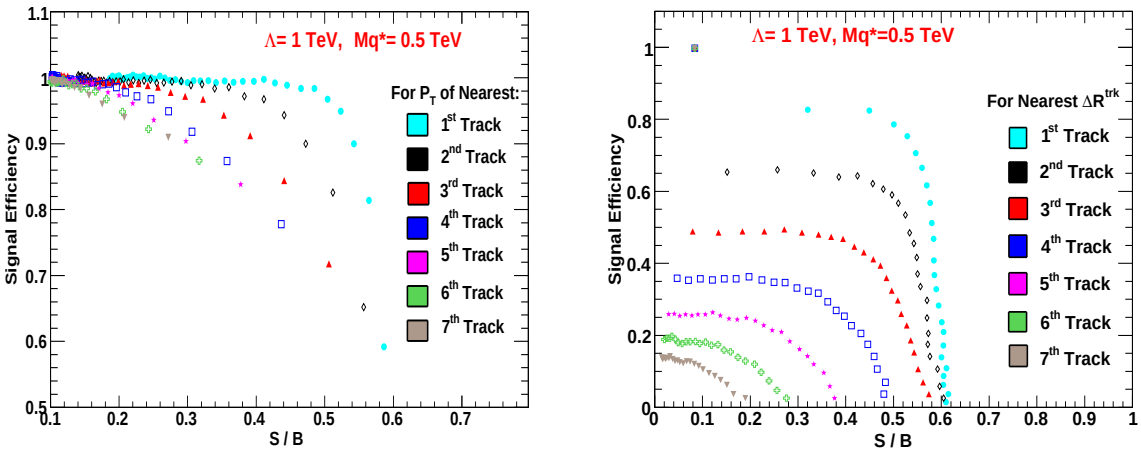

Figure 5.15 (Left)Signal vs S/B for nearest track transverse momentum and (Right) similar distribution for nearest track's ΔR.

5.3.1.3 $\vec{P}_T^{trk}$ sum around the photon

The $\vec{P}_T^{trk}$ sum is another variable which can separate a real photon from a fake one. $\vec{P}_T^{trk}$ sum in a cone is the vector sum of transverse momentum of all the tracks. Figure 5.16(left) shows the distribution for signal and background for this variable. This variable shows a similar behavior as for E_{TSUM} in the previous analysis of $q^* \rightarrow \gamma + jet$. In Fig. 5.16(right) we show the signal efficiency vs S/B ratio profile for this variable for second leading photon for different isolation cone sizes and with different threshold value of $\vec{P}_T^{trk}$-sum. Other than these two cuts discussed above, the ratio, $\vec{P}_T^{trk}/P_T^{\gamma}$ was also studied(not shown).

We studied the effects of these variables on signal and background events and applied these requirements over and above the N_{trk} and $\vec{P}_{Tmin}^{trk}$ cuts. This did not yield a better signal efficiency vs S/B curve. This is due to the fact that most of these selection criteria are correlated. Thus for the sake of simplicity we used only N_{trk} and P_{Tmin}^{trk} requirement for track isolation.

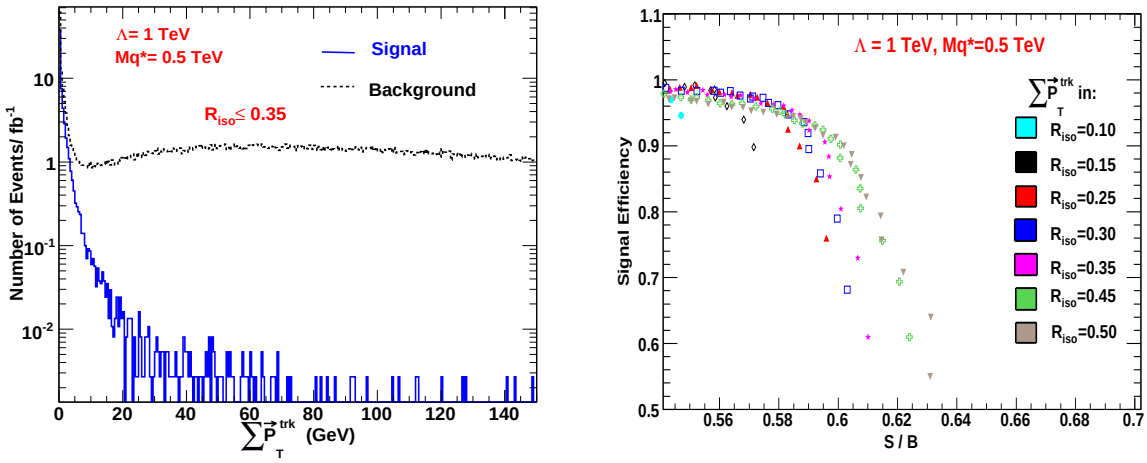

Figure 5.16 (Left)Different profile for signal and background with vector transverse momentum of tracks inside a cone. (Right) Signal efficiency vs S/B ratio for different threshold of vector transverse momentum.

5.3.2 E_T Sum Isolation

Defined as the cluster of energy inside a cone ΔR from which the energy of the photon is subtracted, the variable E_{TSUM} can be used to discriminate against an event wherein a jet fakes a photon. Figure 5.17 shows the normalized E_{TSUM} distributions for the signal and the backgrounds. The main aim of this study is to optimize the E_{TSUM} isolation variable so as to reduce the background from $\gamma + jet$ events (shown separately in Fig. 5.17). As expected the leading photon has similar distribution for the signal and the background. For the second photon though, the behaviors are very different and similar to those for $q^* \rightarrow \gamma + jet$. Most of the $\gamma + jet$ events have $E_{TSUM} > 5$ GeV and by $E_{TSUM} \gtrsim 10$ GeV, the S/B ratio is miniscule. In Fig. 5.18, we show the corresponding signal efficiency(92%) vs S/B ratio for different values of E_{TSUM} and cone sizes around the second leading photon. Each point corresponds to a different E_{TSUM} threshold, varied in steps of 1 GeV beginning with 1.0 GeV. The final choice of the cone size and the E_{TSUM} threshold depends on the track isolation efficiency, the signal efficiency, and the S/B ratio.

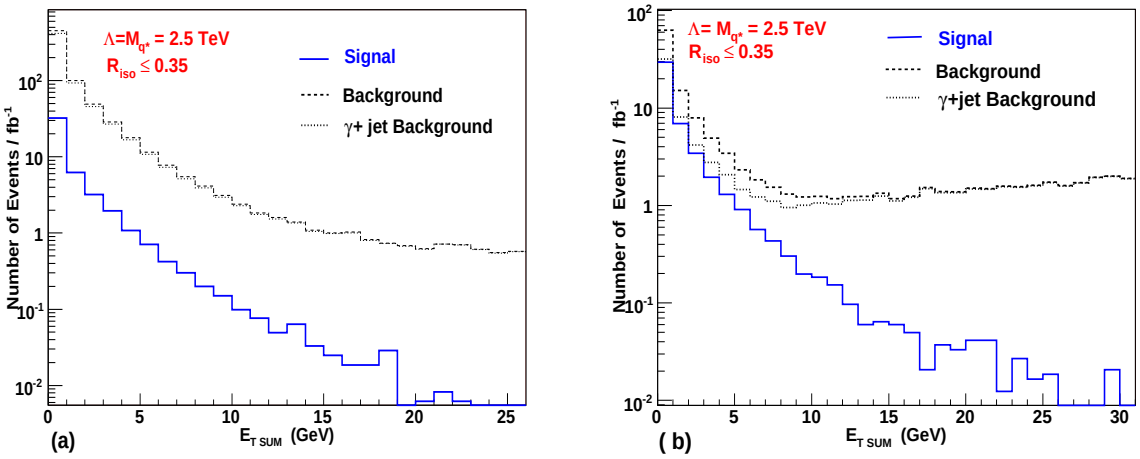

Figure 5.17 E_{TSUM} for the signal and the background events around (a) leading and (b) next to leading photons.

5.3.3 Final Selection Cuts and Signal Observation

In Table 5.4, we show various combinations of isolation variables for two different cone sizes. Since we aim to observe an excess of diphoton production over the SM expectation, it is rather important to have a large signal efficiency. We have performed this study for a large number of $\Lambda - M_{q*}$ signal points for which the cross section is slightly larger than $q\bar{q} \rightarrow \gamma\gamma$ production cross section, or in other words those points for which there will be only a small excess over the SM background. We have used a simple approach by selecting a similar isolation criteria for both the analysis due to similarity in phase space and backgrounds. Based on the studies detailed above, the final selection requirements for $q^* \rightarrow \gamma\gamma$ study are as follows:

- $P_T^{\gamma 1} \geq 200$ GeV, $P_T^{\gamma 2} \geq 200$ GeV;
- $|\eta^{\gamma 1,\gamma 2}| < 2.5 \quad \& \quad |\eta^{\gamma 1,\gamma 2}| \notin [1.4442, 1.5666]$;
- $\cos(\theta_{\gamma 1 \gamma 2}) \leq 0.9$;
- $N_{trk} = 0$ for $P_T^{trk} \geq 3.0$ GeV within $R_{iso} \leq 0.35$;
- $E_{TSUM} < 5.0$ GeV within $R_{iso} \leq 0.35$.

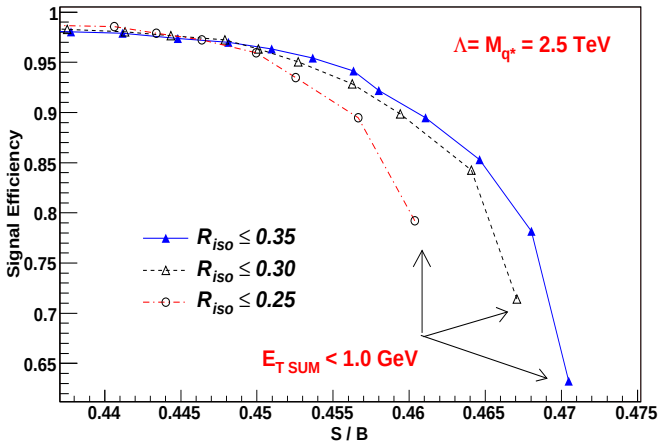

Figure 5.18 Signal efficiency vs. S/B ratio for different cone sizes for different choices of the E_{TSUM} threshold around the second leading photon.

After the application of the fiducial volume and photon P_T criteria, the requirement on angular separation between the photons removes only $\sim 1\%$ events from signal and background.

Table 5.5 shows the number of events surviving for signal, Born, box, $\gamma + jet$ and total background respectively for an integrated luminosity of 1 fb^{-1} after applying the final selection criteria.

Figure 5.19 shows distributions for some of the variables for the generated signal and background events after the selection requirements are imposed. In Fig. 5.19(f), θ^* is the angle between the direction of boost of the diphoton system and each photon in the diphoton rest frame. These distributions clearly show that an excess of events over the background can be observed after the kinematic and isolation requirements.

These distributions are for low mass states which have higher production cross-section and would be easily *observed* if produced at LHC. But for the higher mass states, the data will be statistically limited due to lower cross section. In such cases the statistical tools are must to observe their presence both in $q^* \rightarrow \gamma + jet$ and $q^* \rightarrow \gamma\gamma$ analysis and

R_{iso}	N_{trk}	E_{TSUM}^{max} (GeV)	P_{Tmin}^{trk} (GeV)	S[7] (%)	Born (%)	Box (%)	$\gamma + Jet$ (%)	S[1]/B
0.35	0	4.0	1.5	75.53	75.45	71.86	0.81	0.828
			2.0	80.52	80.40	76.84	0.90	0.824
			3.0	83.33	83.19	79.57	0.96	0.821
		5.0	1.5	77.10	77.05	73.60	0.86	0.824
			2.0	83.15	83.05	79.68	0.98	0.818
			3.0	87.18	87.19	83.79	1.09	0.810
0.30	0	4.0	1.5	81.20	80.99	77.97	0.97	0.817
			2.0	85.73	85.59	82.55	1.07	0.811
			3.0	88.49	88.32	85.44	1.15	0.806
		5.0	1.5	82.25	82.17	79.10	1.01	0.813
			2.0	87.48	87.45	85.45	1.14	0.805
			3.0	91.30	91.24	88.39	1.26	0.798

Table 5.4 Fraction of events surviving for signal and background after applying isolation cuts on both photons (and the P_T^γ & η^γ criteria). Also shown is the S/B ratio.

R_{iso}	N_{trk}	E_{TSUM}^{max} (GeV)	P_{Tmin}^{trk} (GeV)	S[7]	Born	Box	$\gamma + Jet$	Tot.Back.
0.35	0	4.0	1.5	46.32	35.23	1.90	5.67	42.81
			2.0	49.31	37.54	2.03	6.29	45.87
			3.0	51.09	38.85	2.10	6.70	47.66
		5.0	1.5	47.33	35.98	1.94	5.99	43.92
			2.0	50.94	38.78	2.11	6.84	47.73
			3.0	53.54	40.71	2.21	7.56	50.49
0.30	0	4.0	1.5	49.83	37.82	2.06	6.74	46.62
			2.0	52.55	39.96	2.18	7.46	49.62
			3.0	54.35	41.24	2.26	8.00	51.51
		5.0	1.5	50.57	38.35	2.09	7.01	47.46
			2.0	53.67	40.83	2.23	7.93	51.00
			3.0	56.10	42.60	2.34	8.78	53.75

Table 5.5 The number of events surviving for signal and background for $L_{int} = 1\ fb^{-1}$ after applying the final selection criteria. ($Note^7$: Here $\Lambda = 1.0$ TeV and $M_{q*} = 0.5$ TeV and SM diphoton Born production is included.)

will be discussed in the following chapter.

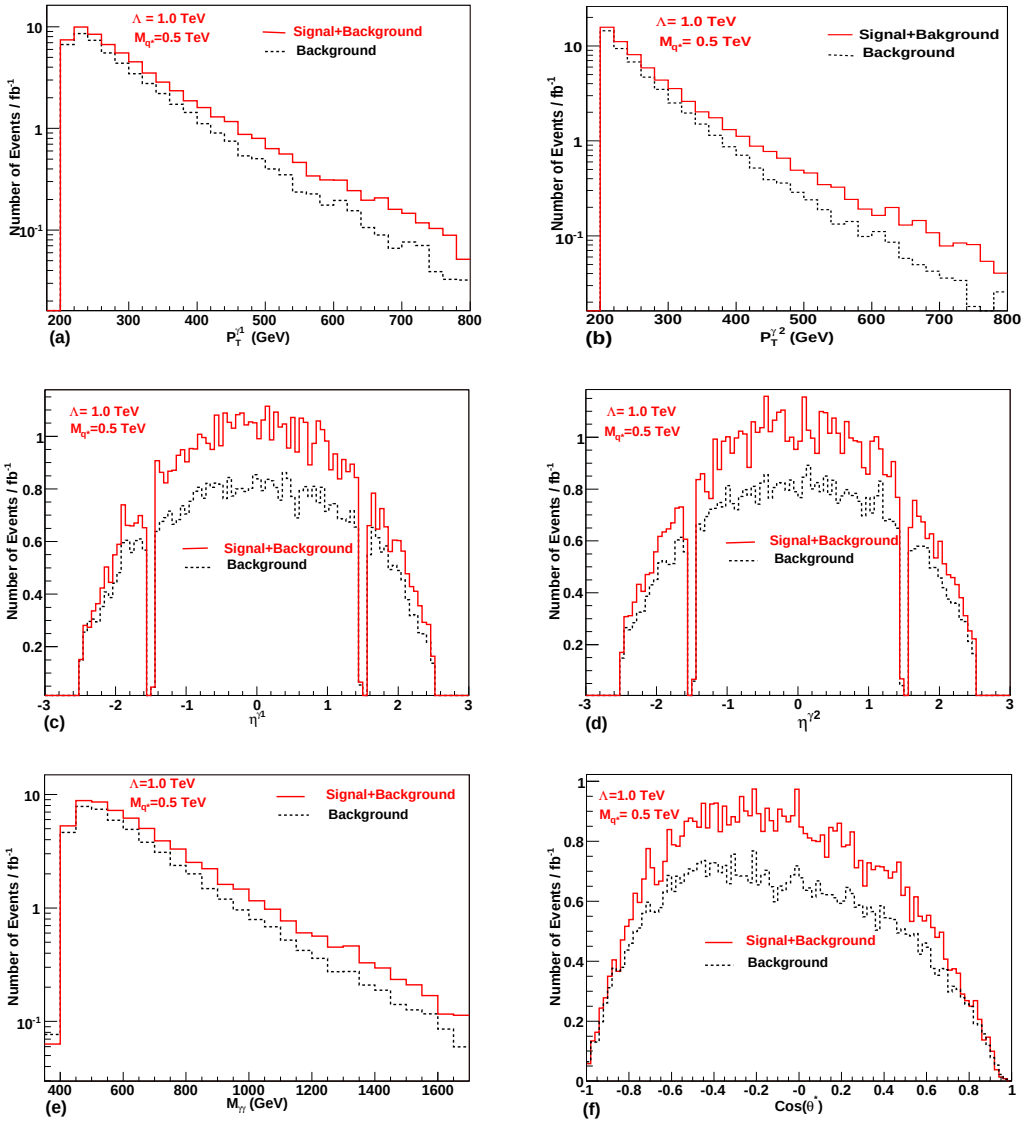

Figure 5.19 Kinematic variables after the selection cuts.(a) $P_T^{\gamma 1}$ distribution,(b) $P_T^{\gamma 2}$ distribution,(c) $\eta^{\gamma 1}$ distribution,(d) $\eta^{\gamma 2}$ distribution,(e) $M_{\gamma\gamma}$ distribution and (d) $\cos\theta^*_{\gamma\gamma}$.

Chapter 6

Significance

"Prediction is difficult, especially the future."

- Niels Bohr.

6.1 Introduction

In the forthcoming high energy physics experiments at the LHC, the main goal is to search for physics beyond the Standard Model(SM) and discover Higgs boson as a confirmation of mass generation mechanism in the SM. The theoretically computed cross section for these new signals are usually overwhelmed by the known SM backgrounds. In most of the cases, statistically, it is not possible to confirm new physics presence in the data. In such cases statistical analysis methods will play an important role in search for small signals over large background in the data. In statistical analysis, the specific numbers are evaluated which express the probability that the result of a given experiment could have occurred purely by chance, could also indicate a margin of error, or they can indicate a confidence level(CL) i.e. if these experiments are repeated, there is a probability of certain percent(ex: 95%, 99%) that our conclusions would be substantiated.

For example, in estimation of the discovery potential, the background cross sections are calculated and for the given integrated luminosity $\int L.dt$, the average number of background events is given by $< N_b >= \sigma_b.\epsilon_b \int L.dt$ where σ_b is the cross-section of background processes and ϵ_b is the selection efficiency. In case new physics leads to a nonzero signal cross section σ_s with the same signature as the background, it results in additional average number of signal events $< N_s >= \sigma_s.\epsilon_s. \int L.dt$ for the same integrated luminosity with selection efficiency ϵ_s. The total average number of events is given by $< N_{ev} >=< N_s > + < N_b >= (\sigma_s.\epsilon_s + \sigma_b.\epsilon_b). \int L.dt$. So, as a result of new physics existence, we expect an excess (or deficient in case of destructive interference) of the average number of events. In a real experiment the probability of realization of n events is described by Poisson distribution [119].

$$f(n, < n >) = \frac{< n >^n}{n} e^{-<n>} \tag{6.1}$$

Here $< n >$ is the average number of events. The Poisson distribution $f(n, < n >)$ is defined as the probability of finding exactly n events in the given interval (e.g, space and time, energy) when the events are produced independently of one another at an average rate of $< n >$ per the given interval. So, to estimate the probability of new physics discovery one has to compare $< n >=< N_b >$ with $< n >=< N_s + N_b >$. In most of high energy physics experiments the "significance" is defined as [120, 121, 122]),

$$S1 = \frac{N_s}{\sqrt{N_b}} \tag{6.2}$$

or

$$S2 = \frac{N_s}{\sqrt{N_b + N_s}} \tag{6.3}$$

A conventional wisdom is that for S1 (S2) ≥ 5 we shall discover the new physics. There are other definitions of significance which has been used [123] when $< N_s >$, $< N_b >$

$\gg$1, e.g.,

$$S12 = \sqrt{< N_b > + < N_s >} - \sqrt{< N_s >} \tag{6.4}$$

and related to S1 and S2 by

$$S12 \approx \frac{S_1 S_2}{S_1 + S_2} \tag{6.5}$$

For $< N_b > \gg < N_s >$, S_{12} is roughly half of S_1 and S_2 [123] which also implies that $S_1 \sim S_2$.

6.2 Statistical Inference and Hypotheses Testing

A statistical inference comprises the use of statistics and random sampling to make inference for some unknown parameters of a dataset. The statistical inference is used for confidence interval estimation and hypotheses testing.

There are mainly two philosophies for statistical inference:

- *Frequentist* **(classical) approach;**
- *Bayesian* **approach;**

In the *Frequentist* approach the inference for an unknown parameter on hypotheses tests, is derived from the distribution of statistics in repeat sampling. While in *Bayesian* approach the inference is based on its posterior distribution, under some model for the data and prior distribution which characterize the unknown parameters to be estimated. The *Bayesian* approach can further be divided into two broad categories of "subjective" Bayes and "objective" Bayes which differ in the choice of different type of priors [124]. Both Bayesian and frequentist methodology have many good points and a few bad ones, but it is futile to attempt to demonstrate that one or the other is superior. They are based on different definitions of probability and they answer different questions. For example in case where decision depends on the value of the parameter, the Bayesian interval is the

most appropriate choice while for reporting the interval with exact coverage, frequentist approach is considered better.

For analysis presented in this thesis, for reporting a discovery/exclusion, we adopt a *frequentist* Monte-Carlo (MC) technique based on a method of hypotheses testing originally due to Neyman and Pearson [99, 125, 126]. If nothing is known a priori about the parameter(for new signal) involved, it is natural to use the data to estimate it. On the other hand, if a theoretical prediction has been made that the parameter should have a certain value, it may be more appropriate to formulate the problem as a test of whether the data are consistent with their values. This is called hypotheses testing and the aim is to determine which one of two competing hypotheses, the so called null hypothesis (H_0) or the alternative hypothesis (H_1) is favored by the data. In the present context, the SM only case (background) constitutes the null hypothesis (H_0) and the presence of new physics (e.g., excited quark contribution to the final state) along with the SM is the alternative hypothesis (H_1). Here H_0 and H_1 will also be referred to as background only (B) and signal plus background (S+B) hypotheses.

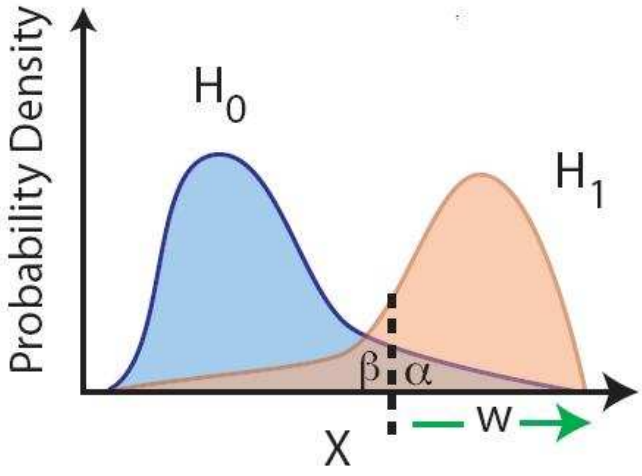

Figure 6.1 A schematic presentation of hypothesis testing and definition of α and β.

In the Neyman-Pearson method one aims to design a test which minimizes the probability β(see Fig. 6.1) of erroneously rejecting an alternative hypothesis (known as *error of second kind*) when it is actually true. Understandably, $1-\beta$ is defined as the power of a test and the most powerful test is the one which maximizes the power for a given value of the probability α(see Fig. 6.1) of rejecting the null hypothesis as false, when it is true instead (also known as *error of first kind*).

According to the Neyman-Pearson lemma [125], the condition for the most powerful test is obtained as a condition on the log likelihood ratio (LLR) or any other *test statistics* of a given data set coming from the null or the alternative hypothesis. Even when the most powerful test does not exist, the *test statistics* (e.g. LLR) can be used for testing between two hypotheses due to its statistically desirable properties [127]. As an example, one accepts or rejects H_0 based on the value of the LLR computed from the data. For this a region, called *critical region*, is defined which is unlikely to come from H_0. If the value of LLR falls in this critical region, H_0 is rejected. Now, α as defined above is clearly the probability of the LLR value falling in the critical region when H_0 is true. Hence, $1-\alpha$ is reported as the significance level of rejecting H_0 (i.e., the SM in our case), or, in other words, this is the discovery confidence level of new alternate hypothesis.

In Fig. 6.1 we illustrate the above description schematically. Here X is the *test statistics* and w defines the "critical region" according to the Neyman-Pearson theorem. If $F_0(X)$ and $F_1(X)$ are the probability density for X associated with H_0 and H_1 hypothesis then α and β are simply given by:

$$\int_{X\in w} F_0(X)dX = \alpha \tag{6.6}$$

$$\int_{X\notin w} F_1(X)dX = \beta \tag{6.7}$$

In the following section using repeated MC trials, we estimate α for discovery and exclusion cases for both the analysis.

6.3 Discovery Significance: $\gamma + Jet$ Search Mode

The confidence levels (CL) are computed by comparing the observed data configuration to the expectations from two hypotheses. In the B hypothesis, only the SM background processes contribute to the accepted event rate, while in the $S+B$ hypothesis the signal from excited quark adds to the background. Each assumed *test-variable*(e.g., P_T, mass etc.) corresponds to a separate $S+B$ hypothesis.

As mentioned in the last section, in order to test the $S+B$ and B hypothesis optimally with the data, a *test statistic* is defined which summaries the results of the experiment with expectations of the $S+B$ and B hypothesis maximally different. One of the optimal choices for *test statistics* is the LLR (log likelihood ratio) of Poisson probabilities which is defined as:

$$Q = \frac{P_{poiss}(data|signal + background)}{P_{poiss}(data|background)} \tag{6.8}$$

where

$$P_{poiss}(data|signal + background) = \prod \frac{(s_i + b_i)^{n_i} e^{-(s_i+b_i)}}{n_i} \tag{6.9}$$

and

$$P_{poiss}(data|background) = \prod \frac{(b_i)^{n_i} e^{-b_i}}{n_i} \tag{6.10}$$

Here the product runs over all bins of the distribution used to discriminate the two hypotheses. The signal estimation depends upon the expected signal cross-section, decay branching ratio, integrated luminosity and the detection efficiency for the signal. The background estimation, b_i, depends on the SM background cross-section, integrated luminosity, and selection efficiencies. The test statistics is more conveniently expressed in

the logarithmic form:

$$-2lnQ = 2\sum s_i - 2\sum n_i \ln(1 + \frac{s_i}{b_i}), \tag{6.11}$$

The multiplicative factor of 2 is introduced to make the statistics behave as χ^2 distributed and is equivalent to a $\Delta\chi^2$ distribution. For a given problem the ratio s_i/b_i should be kept finite either by generating enough MC statistics for signal and background or by rebinning or smoothing. In this procedure an event-weight is assigned to each event. Since in this study we are dealing with MC simulated events, hence the "*data*" n_i in the i^{th} bin of the test variable is generated as a random Poisson fluctuation around the mean value of the i^{th} bin of the theoretical $M_{\gamma-jet}$ histogram. Then the significance level is defined as,

$$\alpha = 1 - CL_B = P(Q \leq Q_{obs}|B), \tag{6.12}$$

i.e., the fraction of experiments in a large ensemble of background only experiments which would produce results more signal-like than the observed data(see Fig. 6.1). By definition, a S+B hypothesis is "confirmed" at the 5σ (3σ) level if α<2.8×10^{-7}(1.35×10^{-3}) [128].

For $q^* \rightarrow \gamma + jet$ final state the most discriminating variable is invariant mass of photon and jet which gives a mass bump over the SM background. Hence we chose M_{q^*} as our *test variable* for this analysis. The other discriminating variable such as P_T of photon and jet are found to be strongly correlated with the invariant mass of the system and are not used. Moreover in other studies it is considered for significance calculation and gives the opportunity for a direct comparison with them [129]. For this study a 3Γ mass window around the M_{q*} is used for the two hypotheses.

In Fig. 6.2, we show the LLR distribution for S+B and B type hypotheses for two

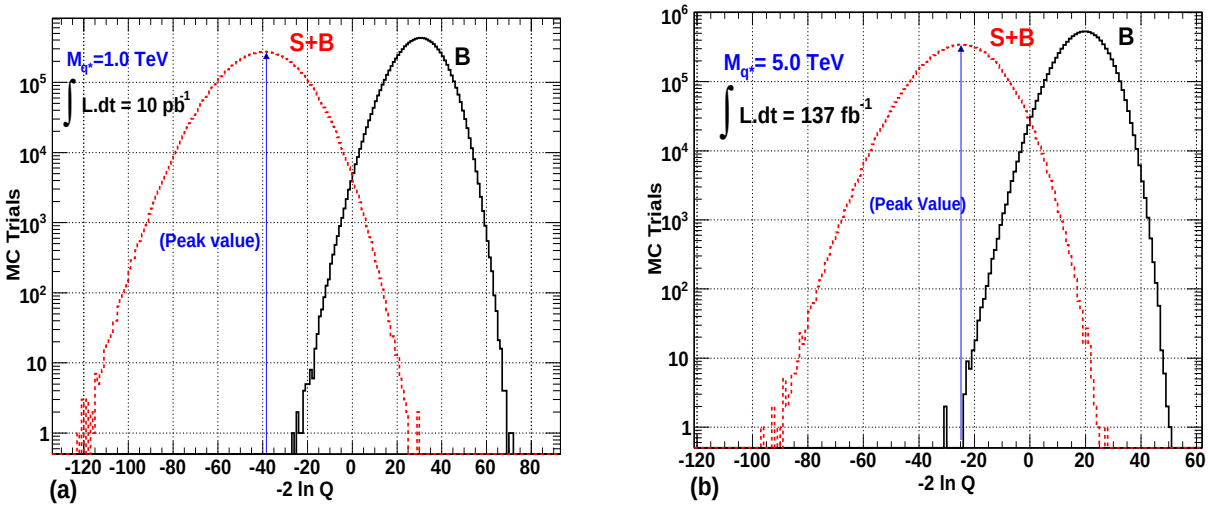

Figure 6.2 Log likelihood ratio distributions for S+B and B type hypotheses for a $5\sigma-$significance for (a) 1.0 TeV (b) 5.0 TeV q^* states.

different mass points namely, 1 TeV and 5 TeV. The luminosities have been chosen so as to yield a 5σ significance for the S+B hypothesis. We have used 10^7 MC trials for these distributions. In this figure, $\alpha = 1 - CL_B$ is the fraction of MC trials of background type hypothesis which falls to the left side of peak value of LLR_{S+B}.

In Fig. 6.3 we show how does the LLR discrimination between two types of hypotheses behave as a function of mass window around the M_{q^*} value. These distributions are evaluated for a stable confidence level of 99% rejection of B type hypothesis and their outcome are equally valid for 5σ- significance of new signal. As visible from the figure, the difference between two hypotheses is more for bins around the center of mass peak and decreases to relatively negligible value at $3\Gamma(q*)$ and beyond this the two hypothesis are not distinct enough to contribute to the significance level. Similar distribution are also shown for M_{q^*} =4 TeV in Fig. 6.4. We found similar results for all signal points despite the fact that they belong to different phase space region. For final selection we have used $\pm 3\Gamma(q*)$ as the mass window around $\gamma - jet$ invariant mass to select signal events. It is to be noted that if $\pm 3\Gamma(q*)$ limit falls in the middle of a bin (with bin width

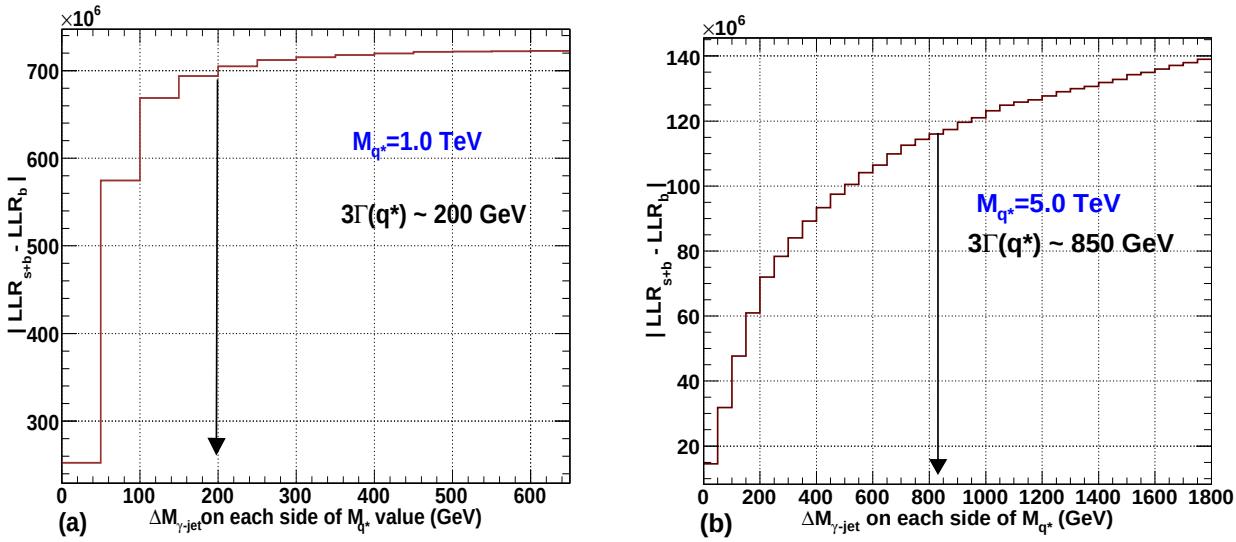

Figure 6.3 Effective LLR contribution as a function of $\Delta M_{\gamma-jet}$ on each side of q^* state of mass (a) 1.0 TeV and (b) 5.0 TeV.

of 50 GeV) then the complete bin has been taken into account. So, the limit of $\pm 3\Gamma(q*)$ is not strict but approximate and this approximation does not effect the significance level.

6.4 Exclusion Limits: $\gamma\gamma$ Search Mode

In this search mode, the q* appears only in the t-channel production of $\gamma\gamma$, hence no resonance peak appears in the diphoton invariant mass distribution. Rather, a discovery needs to be made from an observation of enhanced rate in the diphoton channel as well as differences in the shape of diverse phase space distributions. In this analysis too, we primarily use the information contained in the invariant mass distribution to distinguish between two hypotheses, namely the S+B hypothesis and the B only hypothesis.

Since the signal discovery significance depends on the prominent discriminating variable, here we have evaluated the exclusion limits rather than discovery due to the spread of excess events over the whole mass range. The histograms shown in Fig. 5.19(e)(chapter-5) are used to generate two sets of Gedankenexperiments(i.e., MC trials). To do so, we

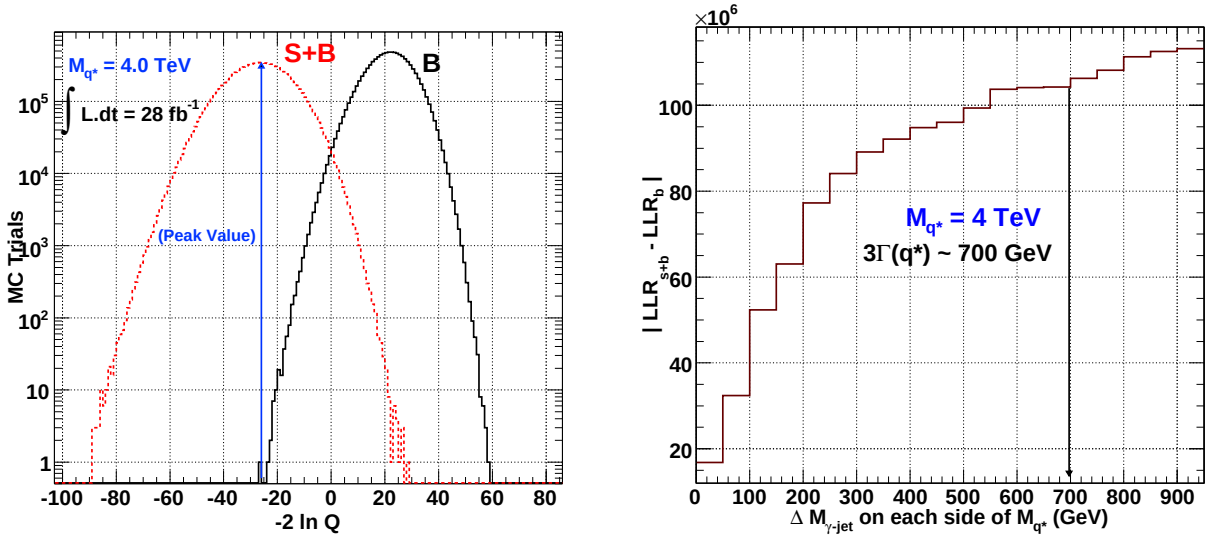

Figure 6.4 Similar distributions as shown in Fig. 6.2, and 6.3 but for a 4 TeV q^* mass state.

assume that the content of each bin in the histograms is Poisson distributed. For every bin, we generate a Poisson random number, taking the original bin content as the mean. These Poisson fluctuated random numbers now represent the bin contents of a histogram which we call the outcome of a single Gedankenexperiment. One million such Gedankenexperiments are generated from the S+B histogram (and, similarly, from the B histogram). From each of these experiments we calculated our test statistic, namely

$$\chi^2_{S+B} = \sum_{i=1}^{n_{bins}} \frac{(d_i - (S+B)_i)^2}{(\sqrt{(S+B)_i})^2} \tag{6.13}$$

and similarly for χ^2_B. Here, d_i is the number of events in the i^{th} bin of the $M_{\gamma\gamma}$ distribution as generated in a particular Gedankenexperiment(in a similar fashion as in $\gamma + jet$ study of q^*) and $(S+B)_i$ is the number of events in the original histogram of $M_{\gamma\gamma}$ obtained from PYTHIA. The distribution in Fig. 6.5 shows how the χ^2 test statistic will be distributed over many repeated observations of the mass histogram. In Fig. 6.5, the solid histogram shows the expected distribution of χ^2 if the S+B hypothesis is true while the dotted one shows the χ^2 distribution if the S+B hypothesis is not true. The most probable value of

χ^2 if S+B is false, is given by the peak of the χ^2_B distribution. The area, α of the χ^2_{S+B} curve to the right of this value is the probability of seeing a χ^2 value $\geq \chi^2_B$ (peak) if the S+B hypothesis is true. For every point in the (Λ, M_q*) plane satisfying $1 - \alpha \geq 99\%$, the point is rejected at 99% CL. In Fig. 6.6 we show similar distributions for another

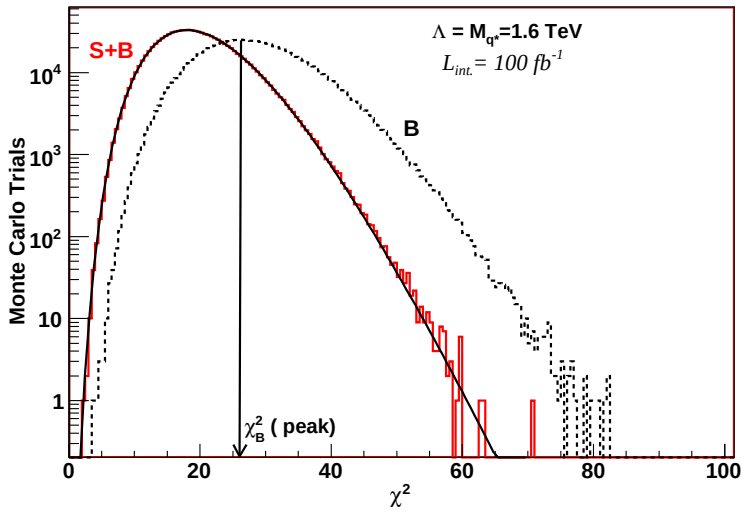

Figure 6.5 χ^2 distribution for $S + B$ and B type hypothesis for a given $\Lambda - M_{q*}$ point with 10^6 MC trials at $100 fb^{-1}$ of integrated luminosity. Here $S + B$ is fitted with χ^2 distribution.

mass state with Λ =2.95 TeV and M_{q*} =0.5 TeV. These distributions are shown for 30, 50, 100 and 200 fb^{-1} of integrated luminosity. The effect of luminosity is quite visible from these distributions. At relatively low luminosity of 30 fb^{-1}, the two hypothesis almost looks identical.

In calculating the χ^2, only bins with large significance are used. These have large bin contents and the latter can be safely assumed to be Gaussian distributed. As a consequence, the χ^2 statistic detailed above is equivalent to a log likelihood statistic for this analysis. Since we have used histograms generated from PYTHIA as our input for the CL extraction there is statistical uncertainty associated with the procedure, i.e., in a repeat of this MC study the position of the χ^2_B peak will fluctuate, resulting in a different

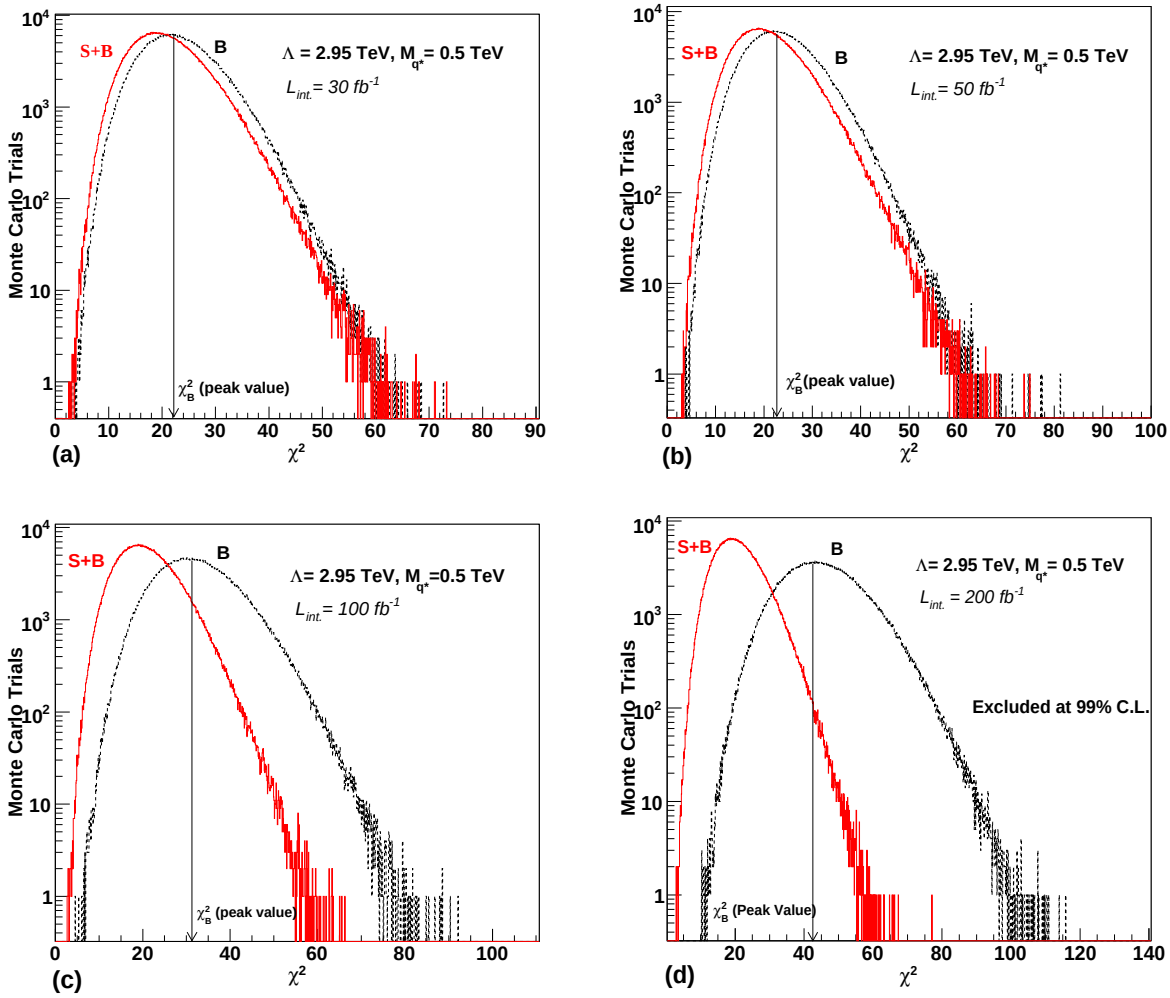

Figure 6.6 The χ^2 distribution for $S+B$ and B hypothesis for $M_{q*} = 0.5$ TeV and $\Lambda = 2.95$ TeV for (a) 30 fb^{-1} (b) 50 fb^{-1}(c) 100 fb^{-1} and (d) 200 fb^{-1} of integrated luminosities. A 99 % CL is achieved at 200 fb^{-1} of integrated luminosity.

value of α. However at $1-\alpha = 99\%$, this fluctuation is estimated to be less than 0.5% on either side of the peak. Here the fact needs to be noted that as $1-\alpha$ decreases the uncertainty associated with exclusion limits also increases with the fluctuation in peak value of χ^2_B due to rapid falling distribution of χ^2_{S+B}. Hence the estimated 99% CL are nearly free from fluctuations and are stable limits.

Chapter 7

Results And Systematics

"My goal is simple. It is complete understanding of the universe, why it as it is and why it exists at all."

- Stephen Hawking.

7.1 Final Results

As described in the previous two chapters, we performed a detailed analysis of isolation and kinematical variables for both search modes and performed the significance/exclusion evaluation using frequentist approach. In this chapter we present our results as discovery and exclusion limits as a function of compositeness scale(Λ) and mass(M_{q^*}) of excited states going into photon plus jet and diphoton modes respectively. The effect of various systematic uncertainties on these results are also presented.

7.1.1 $\gamma + jet$ Final State via q^*: *Possibility of an Early Discovery*

For the $\gamma + jet$ final state, we evaluated our results based on search of a mass bump for the excited quark states over the SM background. We present the results in terms

of total integrated luminosity required for a 5σ-significance as a function of $M_{q*} = \Lambda$. Figures. 7.1(a) and (b) respectively show the integrated luminosity needed to achieve a 5σ and a 3σ significance for the signal as a function of the excited quark mass. These results are reasonably consistent with those obtained using $S/\sqrt{B}$ as test statistic(shown in Table 7.1). In estimating the required luminosity, we have exploited only the mass peak region of the signal over the SM background. For this study we accounted only for those events which fall in a mass window of $\sim \pm 3\Gamma(q*)$ around M_{q^*}. In chapter-6, we have shown that beyond $\pm 3\Gamma(q*)$ the discriminating statistic, namely LLR, looks similar for S+B and B hypotheses and it does not add to the discriminating power beyond this mass window. The results show that in this search mode, a mass state upto $M_{q^*} = 2$ TeV can be discovered in the central region with an integrated luminosity of just $\sim$200 pb^{-1}, equivalent to one year of LHC operation in its initial phase. For higher mass states the required luminosity is shown in Table 7.1.

M_{q*}(TeV)	1.0	2.0	3.0	4.0	5.0	6.0
$\int L.dt$	10 pb^{-1}	350 pb^{-1}	2.8 fb^{-1}	28 fb^{-1}	137 fb^{-1}	1000 fb^{-1}
$S/\sqrt{B}$	6.1	4.2	3.0	4.3	5.0	4.5

Table 7.1 $S/\sqrt{B}$ significance evaluated from the resultant luminosity from a frequentist method using LLR as test statistics.

In Fig. 7.1(a), for the case of standard coupling ($f_i = 1.0$), we demonstrate the effect on the required luminosity by restricting the photon and the jet in the central region of the calorimeter. For 5σ significance upto a mass state of 4.5 TeV, the required luminosity reduces by $\sim 30\%$. Since for $M_{q^*} \gtrsim 5.0$ TeV, the signal events are mostly produced in the central region, the requirement $|\eta^{\gamma,jet}| \leq 1.5$ does not affect the final result significantly. Hence selection of photon and jet in the central region gives better chance of discovery. In

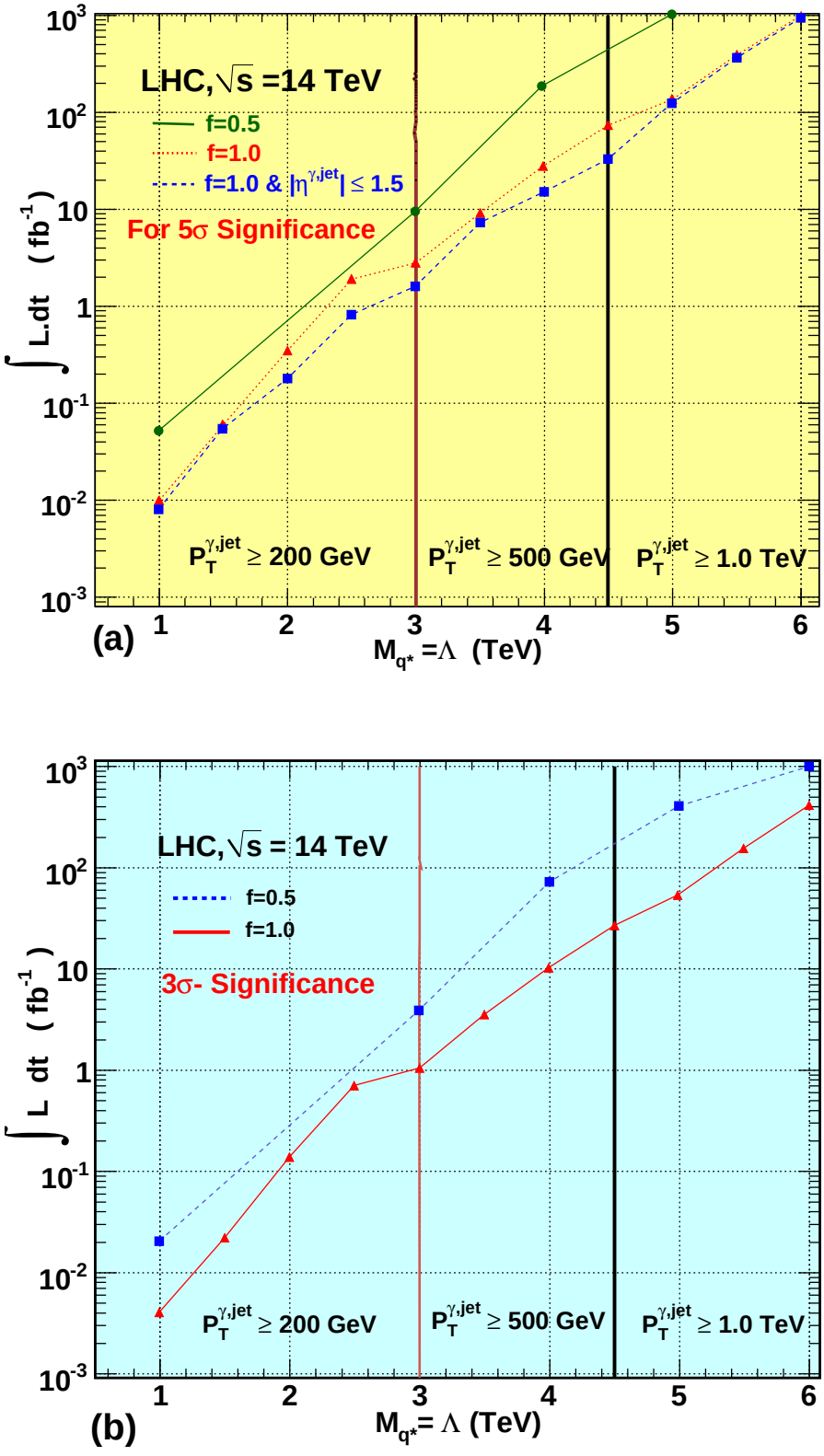

Figure 7.1 Required integrated luminosity as a function of M_{q^*} for (a) 5σ and (b) 3σ significance for two different coupling strengths.

M_{q^*} (TeV)	$\Delta M_{\gamma-j}$ $\pm 3\Gamma(q*)$ (GeV)	$\sigma(S+B)$ (pb)	$\sigma(B)$ (pb)	$\sigma(S^*)^2$ (pb)	Efficiency(S+B) (%)	Efficiency(B) (%)	Efficiency(S*) (%)
1.0	800-1200	9.26	4.92	4.34	1.304	0.699	60.28
1.5	1200-1800	2.034	1.33	0.694	0.288	0.190	46.71
2.0	1600-2400	6.72×10^{-1}	5.10×10^{-1}	1.61×10^{-1}	0.095	0.072	37.23
2.5	2000-3000	2.54×10^{-1}	2.10×10^{-1}	4.41×10^{-2}	0.036	0.029	40.67
3.0	2450-3550	7.85×10^{-2}	6.44×10^{-2}	1.40×10^{-2}	0.011	0.009	75.95
3.5	2900-4150	1.11×10^{-2}	6.93×10^{-3}	4.17×10^{-3}	0.274	0.172	24.70
4.0	3300-4700	4.90×10^{-3}	3.40×10^{-3}	1.50×10^{-3}	0.121	0.084	15.60
4.5	3700-5300	2.20×10^{-3}	1.57×10^{-3}	6.37×10^{-4}	0.054	0.039	11.48
5.0	4150-5850	4.60×10^{-4}	2.47×10^{-4}	2.12×10^{-4}	0.628	0.342	22.49
5.5	4500-6450	2.17×10^{-4}	1.29×10^{-4}	8.81×10^{-5}	0.299	0.179	14.91
6.0	5000-7000	8.39×10^{-5}	5.14×10^{-5}	3.24×10^{-5}	0.115	0.071	7.85

Table 7.2 Cross sections for various M_{q^*} values after imposing all kinematical and isolation cuts (Note: Here S^* represents pure new physics signal evaluated by subtracting B from S+B).

case the coupling of excited quarks to the SM counterparts are reduced to half (f_i =0.5), it can have substantial effect on production cross section and width of q^*. In Fig. 7.1(a) we also show the results with reduced coupling strength.

It is also to be noted that within the model of compositeness presented here, at $\sqrt{s}$ =14 TeV, a 5σ significance can not be achieved for $M_{q^*} \gtrsim 5.5\,\text{TeV}$. While this might seem to run counter to previous work [129] with the same final state, note that, unlike in the earlier efforts, we have used unitarized amplitudes and hence, our cross sections are naturally smaller than used in [129]. The surviving cross section for signal and total background after all kinematical and isolation cuts are shown in Table 7.2 along with the efficiencies. Table 7.3 shows information similar to Table 7.2 but for events restricted to central rapidity($|\eta^{\gamma,jet}| \leq$1.5).

M_{q^*} (TeV)	$\Delta M_{\gamma-j}$ $\pm 3\Gamma(q*)$ (GeV)	$\sigma(S+B)$ (pb)	$\sigma(B)$ (pb)	$\sigma(S^*)^2$ (pb)	Efficiency(S+B) (%)	Efficiency(B) (%)	Efficiency(S*) (%)
1.0	800-1200	4.75	2.14	2.61	0.668	0.304	36.22
1.5	1200-1800	0.87	0.41	0.45	0.123	0.059	30.64
2.0	1600-2400	2.27×10^{-1}	1.10×10^{-1}	1.16×10^{-1}	0.032	0.015	26.82
2.5	2000-3000	6.54×10^{-2}	3.43×10^{-2}	3.11×10^{-2}	0.009	0.004	28.66
3.0	2450-3550	2.21×10^{-2}	1.27×10^{-2}	9.40×10^{-3}	0.003	0.001	50.95
3.5	2900-4150	6.67×10^{-3}	3.20×10^{-3}	3.47×10^{-3}	0.165	0.079	20.55
4.0	3300-4700	2.64×10^{-3}	1.30×10^{-3}	1.34×10^{-3}	0.065	0.032	13.93
4.5	3700-5300	1.01×10^{-3}	4.59×10^{-4}	5.51×10^{-4}	0.025	0.011	9.92
5.0	4150-5850	3.99×10^{-4}	2.00×10^{-4}	1.98×10^{-4}	0.545	0.277	20.98
5.5	4500-6450	1.79×10^{-4}	9.78×10^{-5}	8.15×10^{-5}	0.246	0.135	13.78
6.0	5000-7000	6.51×10^{-5}	3.44×10^{-5}	3.07×10^{-5}	0.089	0.047	7.43

Table 7.3 As in Table 7.2 with additional requirement of centrality ($|\eta^{\gamma,jet}| \leq 1.5$).

7.1.2 $\gamma\gamma$ Final State via q^*: *A High Luminosity Search*

Here, unlike the case of q^* search in $\gamma + jet$ mode where mass bump is obvious, one is dealing with an excess of events over the SM backgrounds for the invariant mass of diphoton. The excess is more obvious for larger value of M_{q^*}. Due to spread of excess of these events over a large kinematical range of invariant mass of the $\gamma\gamma$ system, resultant limits on Λ and M_{q^*} are expected to be weak compared to direct hunt for distinct mass bump and requires higher luminosity for their observation. In Fig. 7.2 we show the $\Lambda - M_{q}*$ parameter space which can be excluded at 99 % CL with 30, 50, 100 and 200 fb^{-1} of integrated luminosity. To calculate the limits, we have used only the invariant mass as the discriminating variable. Since the distribution has a long tail, the analysis has been restricted to $M_{\gamma\gamma} < 1.5$ TeV, so as to have sufficient events for the considered luminosity. The lower limit in $M_{\gamma\gamma}$ was essentially determined by the requirements on P_T^{γ} (as $M_{q^*} \approx 2\ P_T^{\gamma}$). In this search mode our result shows that $\Lambda \leq 2.95$ TeV can be

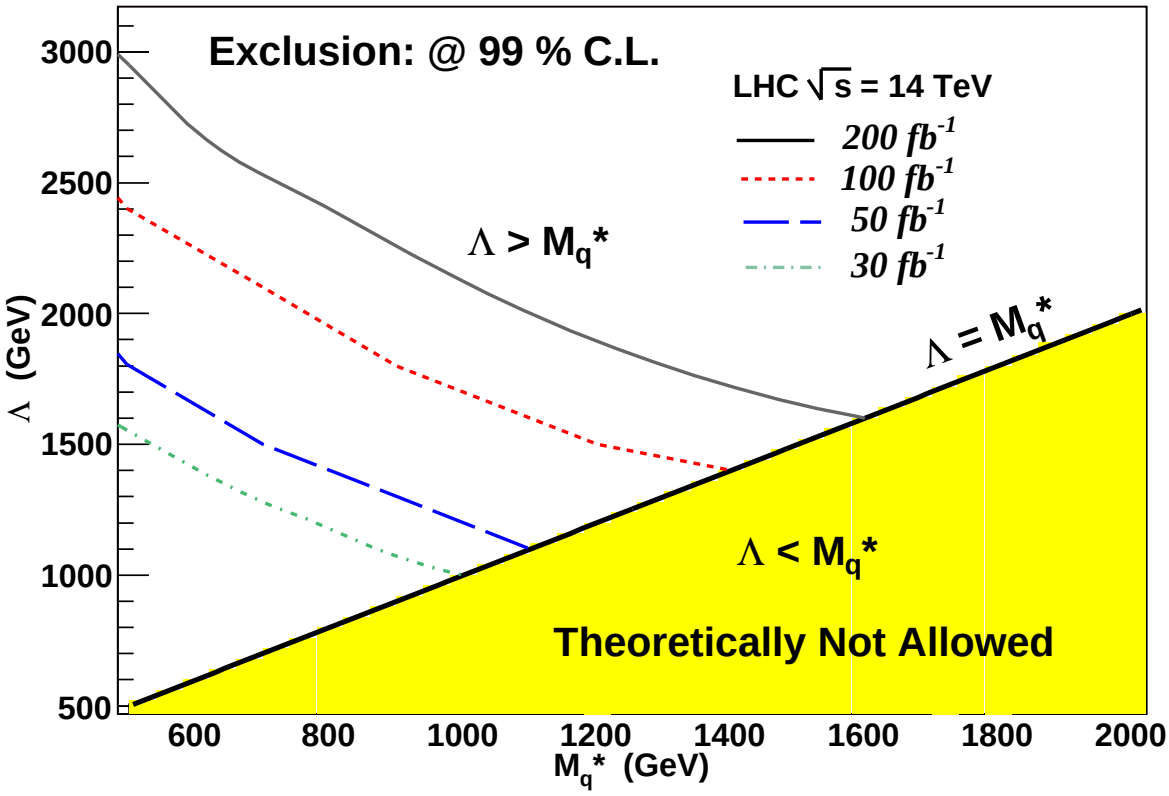

Figure 7.2 Achievable exclusion contours in the $\Lambda - M_q*$ parameter space corresponding to different integrated luminosities at the LHC. The regions below the curves can be ruled out at 99% C.L.

excluded at 99%CL for a mass state of M_{q^*} =0.5 TeV with an integrated luminosity of 200 fb^{-1}. Since we have used the deviation of the invariant mass from the SM prediction as a discriminating variable, we expect that these limits can be improved further by combining other discriminating uncorrelated variables [130].

To estimate the dependence on the choice of kinematical cuts, for few mass points we restricted the fiducial volume for photons from $|\eta| < 2.5$ to $|\eta| < 1.5$. This changes the CL from 98% to 99% CL, which implies that the limits are already very stringent and not much further improvement is expected from tighter cuts. This is quite different compared to the case in $\gamma + jet$ search. Similarly the 98% CL limits obtained with

$P_T^\gamma \geq 200$ GeV changes to 99% CL at $P_T^\gamma \geq 250$ GeV but at the cost of severe loss in signal efficiency.

7.2 Systematic Uncertainties

"Systematic uncertainties" are the bias in the measurement by various sources such as calibration methods, conceptual errors, data acquisition etc. As an example, some bias always remains in the calibration process as no standard is perfect and no calibration is perfect. Similarly our understanding of a new process and its measurement also depends on various conceptual methods such as cross-section estimation, natural width calculation etc. which in turns depends on various parameters and the outcome behaves differently with different inputs. Repeating the measurement cannot be used to reduce them, because these effects will be present in the same way each time, unlike random effects which are different each time and hence will tend to cancel somewhat in averages. Systematic uncertainties can only be reduced through use of controls and calibration runs. Usually in high energy physics experiments different systematic contributions come from detector components; through various assumptions made in theoretical and experimental methods used and due to measurement techniques. Below we have discussed many of them separately for both the analysis. Their effects on results have been estimated.

7.2.1 Systematics for $\gamma + jet$ final state

Since we have performed a detailed analysis including a realistic simulation of various detector effects for the CMS setup, here we present an estimation of systematic uncertainties. For both, the signal and the $\gamma + jet$ background, we concentrate on the dominant process, viz. $qg \rightarrow q\gamma$. For the estimation of uncertainties in the QCD dijet background, all the available processes in PYTHIA have been used. We do not account

for uncertainties in $q\bar{q} \rightarrow \gamma + jet$, $gg \rightarrow \gamma + jet$ and $W/Z(\rightarrow jj) + \gamma$ processes as they contribute only a small fraction of the total background and systematic uncertainties in these can be safely ignored.

- Choice of the Parton Distribution Function(PDF): In the parton picture, hadron consists of partons and these partons undergo a hard collision at large Q^2. The parton distribution functions(PDFs) are evaluated at small momentum fraction x but their x dependency is not predicted except at a small virtual scale Q_0^2. The PDFs($F(x, Q^2)$) at all higher Q^2 are determined by NLO perturbative QCD evolution equations. As described in Appendix-B, the cross-section can be written as convolution of PDF and a hard cross-section for partonic process. To estimate the uncertainty in the cross sections due to the choice of the PDF, the former is recalculated for three additional PDFs, namely CTEQ6L, CTEQ6M [131] and MRST2001 [132]. Using the LHAPDF package [133], the result for each of these are compared to our default choice, namely CTEQ5L [107]. While the resultant cross sections turned out to be higher for CTEQ6M (it should be noted that the CTEQ6M distributions are NLO and hence their use with LO calculations is fraught with danger) and MRST2001 distribution, for CTEQ6L it turned out to be lower for almost all the signal points. As expected, the uncertainty in the cross section increases with M_{q^*}, simply because one starts to sample an ill-explored region in the (x, Q^2) plane. For CTEQ6M and MRST2001, the relative deviation varies between 2.3–13.0 % and 2.6–14.2 % respectively for M_{q^*} from 1 TeV to 6 TeV. For CTEQ6L, the variation was found to be within -4.5 to $+2.25$ %. These numbers are quite consistent with those applicable for the SM $\gamma +$ jet process alone, for which the corresponding numbers are 5.6–11.0% (CTEQ6M) and 6.0-12.0%(MRS2001). Similarly, for the dijet background an uncertainty of 9–16% (CTEQ6M) and 8.7–16.5% (MRST2001) has been estimated.

We have not only used different PDFs but have also evaluated uncertainty due to a given proton PDF by varying the errors on the parameters of the PDF fit itself. This is one of the "brute force method" used for estimating PDF uncertainties. In this method the "fit" to data is not only evaluated with the "best fit" (the global minima of χ^2) but also with different fit parameters. The error on any measurable quantity which depends on PDFs, say P with P_0 estimated with "best fit", is given by:

$$P^{+\Delta P^{+}_{max}}_{-\Delta P^{-}_{max}} \tag{7.1}$$

where P^+ and P^- are calculated as,

$$\Delta P^{+} = \sqrt{\sum_{i=1}^{d} (max[(P_i^+ - P_0), (P_i^- - P_0), 0])^2} \tag{7.2}$$

$$\Delta P^{-} = \sqrt{\sum_{i=1}^{d} (max[(P_i^+ - P_0), (P_i^- - P_0), 0])^2} \tag{7.3}$$

The $P_i^{\pm}$ are evaluated over "d" number of parameters which are varied in both direction compared to the "best fit" case.

For this, we chose CTEQ6L (with NLO α_s and LO fit) and its 40 subset PDFs($2 * d$). The uncertainty was found to be $\sim \pm$ 1% for a 1 TeV q^* state and -8.29% to $+10.93\%$ for a 5 TeV mass state. For QCD di-jet and $\gamma + Jet$ background these numbers were found to be -9.81% to $+13.74\%$ and -8.04% to $+10.54\%$ respectively.

- Scale Variation: The dependence of cross-section on Q^2 comes directly from the running strong coupling constant(α_s) and from the parametrization of PDF. To estimate the dependence of the signal and the background cross-sections on the choice of the factorization scale Q (default value in both the analysis being $\sqrt{\hat{s}}$),

they were recalculated for three other values of the latter viz $Q^2 = P_T^2$, $Q^2 = -\hat{t}$ and $Q^2 = 2\hat{s}$. The first two choices for the scale would have resulted in a higher cross-section compared to $Q^2 = \hat{s}$ while the third one gives lower value. It is found that the deviation increases with M_{q^*} and ranges between 2.1–11.3% for $Q^2 = -\hat{t}$, 10.6–25.0% for $Q^2 = P_T^2$ and is in the $(-3.0\%, -5.0\%)$ range for $Q^2 = 2\hat{s}$. For the QCD di-jet background the maximum positive deviation was found to be ∼39% while for $\gamma + jet$ it was ∼26%. On the other hand with $Q^2 = 2\hat{s}$ these values are lower by $\sim 8\%$ and $\sim 5\%$ respectively compared to $Q^2 = \hat{s}$. Due to α_s involvement at both the veritces, the expected uncertainty is quite large in the QCD dijet case.

- Higher-order effects: For the backgrounds, these have been studied in detail both theoretically and experimentally. For example, $\gamma + jet$ production in the SM has been studied in depth using the NLO parton level Monte Carlo program JETPHOX [94, 134]. Recently, a comparison of these predictions have been done with the Tevatron data[135]. Unfortunately, the P_T^γ-dependent shape of the triple differential cross section($d^3\sigma/dp_T^\gamma dy^\gamma dy^{jet}$) for different pseudorapidity ranges is not explained satisfactorily by the NLO calculation. The reason is not hard to fathom. A comparison with data necessitates the imposition of isolation cuts. On the other hand, the NLO calculations depend crucially on the choice of isolation cuts and infrared safety needs to be taken care of. This has been discussed in detail in Ref.[136]. Modulo such subtleties, an effective and easy way to incorporate higher order effects is to include K-factors. For $\gamma + jet$ production, the K-factor lies in the range 1.0–1.66, depending on the details of jet fragmentation (primarily, to a γ/π^0)[137]. While the K-factor for our case is not known, in the large M_{q^*} limit it is not expected to be too different from the SM case. Close to threshold, the K-factor is normally expected to be even larger. However, given the attendant theoretical complications, we adopt a conservative approach and ignore all K-factors

in this analysis. Moreover in view of large systematic uncertainty from PDF and scale, we can safely assume that these results are not affected much by K-factor.

- Jet Energy Resolution(JER): To incorporate finite detector resolution, the photon and jet four momenta were smeared with energy resolutions as given in chapter-4. For the photon P_T range considered in this analysis, we expect the constant term (C) to be the dominant source of error and it contributes about 0.55% to jet energy resolution. To estimate the effect of the jet energy resolution on this analysis, we redid this analysis smearing the four momenta of the jet with an energy resolution of 100% for the barrel region and 150 % for the endcaps and the forward regions. The effect was studied for two different mass states, viz. 1.0 TeV and 5.0 TeV. It was found that such a large worsening of the jet energy resolution would increase the required luminosity for 5σ significance by about 30% (1%) for 1.0 TeV (5.0 TeV) mass states respectively. However, if we increase the number of MC trials by a factor of 10 (to stablize the peak value of LLR_{S+B}), these numbers were found to be well within 2%.

  It should be noted that the ATLAS detector at the LHC has a better jet energy resolution with a constant term of $\sim$2 % [109] compared to $\sim$5 % for the CMS. On the other hand, the CMS ECAL has a better resolution compared to ATLAS owing to a smaller constant term. However, with the resolving power being dominated by the jet energy resolution, ATLAS should do somewhat better. In other words, our results correspond to a *conservative* choice.

- Uncertainty due to pre-selection: The systematic uncertainty due to pre-selection in the P_T range of this study is estimated to be about $\sim$ 1%.

- Luminosity error: For the CMS experiment, this error is expected to be $\sim$ 10% for an integrated luminosity of 1 fb^{-1} [138] and $\sim$ 3% for an integrated luminosity of 30 fb^{-1} [139].

- Effect of bin width and MC trials: The statistical inference methods are ideally not independent from various input parameters like bin width, number of MC trials etc. Hence, we performed the stability check of the results by varying the bin width of the invariant mass distribution from 50 GeV to 20 GeV for $M_{q^*} = 1.0\,\text{TeV}$ and 2.0 TeV and found that the luminosity required for 5σ significance changes by 20% and 1.1% respectively. It should be noted here that a requirement of extra 20% luminosity for 1 TeV point is not much since the required luminosity itself is quite low. For $M_{q^*} = 5.0\,\text{TeV}$, on the other hand, we varied the bin width from 50 GeV to 100 GeV and found that the required luminosity changes by 2.1%. One of the uncertainties in significance calculation comes from the uncertainty in the position of peak value of LLR_{s+b}, which in turn effectively determines α(defined in previous chapter). Hence to estimate this the number of MC trials was increased by a factor of 10 for significance calculation and found that the required luminosity changes by $\sim$ 20%, 0.8% and 2.1% respectively for the 1.0, 2.0 and 5.0 TeV mass points.

7.2.1.1 Effect of Systematics on Results

In Table 7.4 we show the dominant contributors to the total systematic uncertainty for two different mass points. The combined effect of all systematics on the required luminosity for discovery is also presented. Since the uncertainty in cross section due to choices of PDFs and scales (Q^2) are not independent, we varied them simultaneously to estimate their combined effects. For this purpose various combinations of scale($2\hat{s}$, $\hat{s}$, $-\hat{t}$, P_T^2) and PDF(MRST2001, CTEQ6M, CTEQ6L, CTEQ5L) are used. The maximum deviation w.r.t the default values are shown in Table 7.4.

For estimating the uncertainty arising due to jet energy resolution(JER) we increased the stochastic terms of JER to 100% in the barrel region and 150% in the endcaps, while the constant term (the dominant contributor for this analysis) was changed from 5% to 8 % [140]. After smearing, the required integrated luminosity was estimated

	Process	PDFs and scale uncertainty on cross section max. (min.) %	Luminosity error ±%	Jet Energy Resolution(JER) effect on events in mass window ±%	$\int L.dt$ without systematic (Fig. 7.1(a))	$\int L.dt$ due to JER uncertainty only	$\int L.dt$ with combined max.(min.) systematic
Signal	2 TeV	19.71 (-4.61)	10	-1.74	350 pb^{-1}	390 pb^{-1}	336 (430) pb^{-1}
Background	QCD dijet	58.08 (-8.14)	10	0.55			
	$\gamma + jet$	19.76 (-4.61)	10	0.99			
Signal	5 TeV	35.91 (-10.24)	3	-0.18	137 fb^{-1}	156 fb^{-1}	126 (171) fb^{-1}
Background	QCD dijet	51.32 (-13.33)	3	0.37			
	$\gamma + jet$	37.45 (-9.61)	3	0.18			

Table 7.4 Major contributors to systematic uncertainty for the signal and respective backgrounds and their effect on required integrated luminosity for 5σ discovery.

again. Since the uncertainty due to PDF, scale and luminosity are related with the cross section measurement, a linear addition(a more conservative choice compared to addition in quadrature) of these was applied on top of the uncertainty due to JER to evaluate total combined effect. Our results show that systematic effects are indeed large compared to results from Tevatron and mainly dominated by scale and PDFs choices. Since the two point studied above give similar results even though they belong to two different phase space regions, we expect similar behavior for other mass states analyzed in this work. It is also true that at LHC with limited initial luminosity, the systematics would be large for the discovery of low mass states and improvement is expected with larger statistics in later years.

7.2.2 Systematics for $\gamma\gamma$ final state

In the previous subsection we presented a detailed study of systematics for $q^* \rightarrow \gamma + jet$ and its backgrounds including $\gamma + jet$(SM), which is also the main background for $q^* \rightarrow \gamma\gamma$ search. Hence we present the systematic uncertainties for signal only. These uncertainties will presumably also reflect the uncertainty involved in SM diphoton production.

- Choice of PDF: For estimating this uncertainty, the cross section is re-calculated with other PDFs and the results obtained are compared with those from CTEQ6M [131]. For comparison we used CTEQ5M1, CTEQ5L and MRST2001. A maximum uncertainty of $\sim$7% was found when CTEQ5L was compared to CTEQ6M. For CTEQ5M1 and MRST2001 these values are 2.3% and 3.5% respectively.

- Scale Variation: To estimate this, the factorization scale Q (chosen to be $\sqrt{\hat{s}}$ in our analysis) was varied in the range $Q^2 \in [\hat{s}/2, 2\,\hat{s}]$. Also used was $Q^2 = P_T^2$. In all these variations, the maximum uncertainty was found to be 1.6%.

- Higher-order effects: The SM processes relevant to this study have been studied in the literature at great length. For true diphoton production, the expected $K-$ factors are 1.5 (Born process)[141] and 1.2 (box) [142]. For the $\gamma + jet$ events, these are 1.66 when the quark fragments into a photon [142] and 1.0 when an (almost) isolated π^0 in the hadronic jet fakes a photon [142].

  Since the quantitative details of quark fragmentation into γ/π^0 are imprecisely known, and the present knowledge of fragmentation functions coming largely from data with $x < 0.7$ [143], where x is the ratio of γ/π^0 to jet energy, the uncertainties can be particularly important at large x. Tighter isolation cuts could reduce the fragmentation contribution but at the same time would select events corresponding to higher values of x. A detailed discussion on such uncertainty and the effects of tighter isolation cuts is out of scope of this work and can be found in Ref. [143].

  For new physics contribution, the K-factor is not known though (indeed, the very definition could be ambiguous for a non-renormalizable theory), and hence we have not used any in our analysis. However, in the limit of a very large M_{q^*}, the new physics effect should be describable in terms of an effective operator involving quarks and photons and the K-factor, in this limit, is not expected to be too different from the SM one [144]. However it must be mentioned that there are

calculations available, e.g. ResBos and DIPHOX, which do take into account higher order effects and describe the diphoton data well at Tevatron energies[145]. Some of these calculations like DIPHOX include fragmentation contributions at the NLO level and are sensitive to certain distributions as shown in Ref.[145].

If one assumes the signal K-factor to be indeed similar to the overall background, the net effect is a scaling of eq.(6.13) by a factor of K. This translates to a modification in the separation between the peaks of the two histograms in Fig. 6.5 by a factor of K and is equivalent to an increase in the luminosity by the same factor. To be conservative, we choose to ignore the consequent improvements in the exclusion limits.

- Energy resolution: To study the effect of the detector energy resolution on this analysis, the energy of the photon was smeared with the stochastic term of the CMS electromagnetic calorimeter energy resolution [75]. The effect was found to be negligible.

- Luminosity error: Similar to $\gamma + jet$ analysis, above $30 fb^{-1}$, the uncertainty on the measured integrated luminosity is expected to be $\sim$3%[139].

- Uncertainty from CL evaluation method: We have checked the stability of the limits and found that the 99% CL value suffers only a very small error ($< 0.5\%$) from the uncertainty in the position of the χ^2_B peak as determined from Monte Carlo trials. We have determined the effect of uncertainty in the theoretical cross-section on the CL. To get a conservative estimate we lowered the cross section by 1% and found that 99% CL changes to 98% CL.

7.2.2.1 Estimation of Dijet Background

Due to limitations in computing resources, we did not fully simulate the background from jet-jet events. Although the dijet cross sections are very large, given the low probability

of a jet faking a photon (as described earlier in the text), it is obvious that not too many such events would survive the selection criteria that we have imposed. A parton-level Monte Carlo calculation readily verified this.

Even in the corresponding PYTHIA study, it was again observed that the kinematical and isolation cuts reduce this background drastically. In a sample of 9000 jet-jet events, not a single event survived the final selection requirements. However, with the same survival efficiency as for $\gamma + jet$ events (i.e., $\sim$1 %) and with same kinematical and isolation cuts, we expect to have a jet-jet background of less than 3.7 event for an integrated luminosity of 1 fb^{-1}. Hence one can safely assume that two photon events from jet-jet background will have negligible effect on the final confidence level calculation.

Chapter 8

Summary And Conclusions

"Science never solves a problem without creating ten more."

-George Bernard Shaw.

The puzzle what is so special about the number *"three"*, in which the quark and lepton families exist could possibly be answered if we find that quarks do have substructure. This may also shed some light on some other fundamental questions like the difference in mass amongst the three families and could possibly reveal any new hidden underlying interaction among these constituent of quarks.

Within the SM framework, direct photon production is very well understood and hence provides better handling of the QCD backgrounds for new physics searches. In last few decades, a good theoretical understanding has been developed and any deviation from such observation would be a clear indication of some new physics.

To summarise the work done in this thesis, we have investigated the potential of using the $\gamma + jet$ and $\gamma\gamma$ final states at the LHC for probing possible substructure of quarks. In any model of quark compositeness, excited states occur naturally and these couples to the SM counterparts through a generalized magnetic transition term in an effective Lagrangian. Consequently, the presence of such states would alter the the cross section and could change the shape of kinematical variables which would be visible at

interaction scale in the TeV region. The extent of these changes depends on the mass M_{q^*} of the composite particle, the compositeness scale Λ, and couplings of q^* to photon and gluons.

Using the photon and jet reconstruction algorithm for the CMS detector, we have performed a realistic estimation of the deviation caused by excited quark exchange contribution to the $\gamma + jet$ and $\gamma\gamma$ rate. We have accounted for all major backgrounds to evaluate limits in the $\Lambda - M_q*$ parameter space. Isolation requirements using tracking system and the calorimeters were used to maximize photon purity and to reduce backgrounds. The threshold for these requirements were decided by studying S/B and signal efficiency curves. It has been found that using a larger cone size of 0.35 for isolation studies gives a better rejection of the QCD backgrounds.

For $\gamma + jet$ final state, the excess of events shows up as a mass bump over the SM production for Compton diagram, and as an excess of cross-section for annihilation diagram. For our studies we have estimated the required luminosity for 5σ discovery in 1-6 TeV range for $M_{q^*}(= \Lambda)$. We have performed the analysis by dividing the mass points in three different kinematical range for transverse momentum of photon and jet, viz $P_T^{\gamma,jet} \geq$ 200 GeV , 500 GeV and 1 TeV. The study shows that if we restrict our analysis to central rapidity only, a 3 TeV mass state can be discovered with 5σ significance for $\sim$2 fb^{-1} of data. The discovery potential is very limited for M_q^* =5.5 TeV and beyond. We have also evaluated results for 3σ significance. Various systematic uncertainties have been reported and their effects on results are presented in a simplified manner. It is to be noted that $\Gamma(q^*)$ being typically quite large, a narrow-width approximation does not hold and the full matrix element needs to be incorporated. The other issue is connected to the non-renormalizable nature of the effective Lagrangian. Since a naive use of a "chromomagnetic" dipole moment vertex leads to a cross section constant or even growing with the center of mass energy, the amplitude needs to be unitarized. This, understandably, leads to a suppression of the cross sections, a fact often ignored in experimental analysis.

But we have taken this effect into account.

For $\gamma\gamma$ search mode the deviation concentrates in the large p_T regime, especially for larger M_{q^*} and can be substantial. For example $\Lambda = M_q*$=1 TeV leads to a $\sim$12% deviation in the cross section (when restricted to an appropriate part of the phase space as defined in chapter-4). While direct searches, as mentioned above, can lead to very strong limits from the non-observation of mass peaks, the search strategy outlined here can prove to be a complementary tool. In particular this mode is sensitive to excited quark masses far above the kinematical limit for pair-production (which mainly proceeds through gauge interaction). We have looked for the signal in the diphoton mass range of 450 GeV to 1.5 TeV. We estimated the possible exclusion contours in $\Lambda - M_{q^*}$ plane at 99% CL for $\int L.dt$ =30, 50, 100 and 200 fb^{-1} scenario. The analysis shows that the possible exclusion limits are very strong and depends only weakly on the choice of the kinematical cuts. For this analysis also we estimated the systematical uncertainties.

In conclusion we believe that if quarks have substructure, the excited state should be observed in $\gamma + jet$ final state at the CMS detector with few fb^{-1} of data in first few years of LHC operation. If such signals are indeed found in the early phase of LHC operation, in later years $\gamma\gamma$ excess over the SM diphoton production could further stamp for their existence.

Appendix A

Co-ordinate and Kinematical Variables

A.1 HEP Colliders

High energy experiments can be divided into two classes, depending on how particles interact:

- Fixed Target Experiment: In this case a beam of particle accelerated to desired energy strikes a stationary target. The center of mass energy comes out to $\sqrt{s} = \sqrt{2Em_p}$ where m_p is the mass of the proton/neucleon in the stationary target and E is the beam energy. Thus in a fixed target experiment $\sqrt{s}$ increases as the square root of the beam energy.

- Colliding Beam Experiment: In this case two beams are accelerated to desired energy and made to collide head-on with each other. The available center-of-mass energy is given by $\sqrt{s} = \sqrt{4E_AE_B}$, where E_A, E_B are the proton beam energy. In this case $\sqrt{s}$ grows linearly with the beam energy.

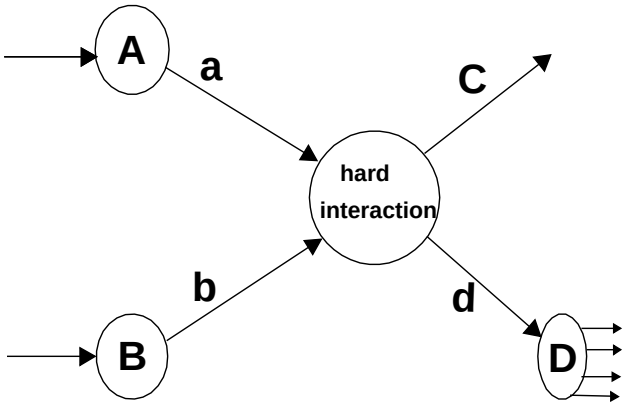

Figure A.1 Schematic presentation of partons and fragmentation in beam collision.

It is obvious that for a new massive particle production, beam collider experiments are better suited than the fixed target experiments.

In collider experiments the co-ordinate system describing physics events as well as the detector are very important from the view point of physics analysis. Various kinematical variables crucial for description of both have been briefly discussed in this section.

Fig A.1 shows a schematic view of hard interaction of two colliding beam particles(e.g. protons in our case), while 'a' and 'b' are the partons that take part in the hard interaction. The final state particles could be photon, or partons which further fragment into colorless hadrons through the process of hadronization and results in a *jet* as shown in the diagram.

The two partons which take part in the hard interaction do not carry the total momentum of the colliding protons. Let us assume that 'a' and 'b' carry fraction x_a and x_b of the total momentum of the colliding protons. Then the four momenta is given as:

$$p_a = E_{beam}\,(x_a; 0, 0, x_a) \tag{A.1}$$

$$p_b = E_{beam}\,(x_b; 0, 0, -x_b) \tag{A.2}$$

Two other variables which are important for event topology and kinematics are :

$$x_T = \frac{2p_T}{\sqrt{s}} \tag{A.3}$$

$$x_F = \frac{2p_z}{\sqrt{s}} \tag{A.4}$$

where x_T and x_F are the momentum fractions of the colliding partons in the transverse and longitudinal directions respectively. With these definitions, the x_T and x_F can acquire values $(0, 1)$ and $(-1, 1)$, respectively. It must also be mentioned that partons inside a particle are always virtual and hence space like.

In a $2 \rightarrow 2$ process, the other two variables needed to describe the kinematics are azimuthal angle ϕ and polar angle θ. The ϕ corresponds to the scattering plane around the beam axis and θ is the polar angle of the outgoing particle C in center of mass frame of hard scattering.

The particle kinematics can also be defined in terms of mandelstam variables [146], $\hat{s}, \hat{t}$ and $\hat{u}$. These variables are *Lorentz* invariant and widely used to define kinematics of multibody final states for a $2 \rightarrow 2$ process.

The invariant mass of the two colliding parton $\hat{s}$ is defined as

$$\hat{s} = (p_a + p_b)^2 = x_a x_b s \tag{A.5}$$

$$\hat{t} = (p_a - p_b)^2 = \frac{-\hat{s}}{2}(1 - \cos\hat{\theta}) \tag{A.6}$$

and

$$\hat{u} = (p_a - p_d)^2 = \frac{-\hat{s}}{2}(1 + \cos\hat{\theta}) \tag{A.7}$$

Other expressions to define mandelstam variables are:

$$\hat{t} = -x_a p_T \sqrt{s} e^{-\eta_a} \tag{A.8}$$

$$\hat{u} = -x_b p_T \sqrt{s} e^{\eta_a} \tag{A.9}$$

If outgoing particles have masses M_C and M_d then the following relation is true.

$$\hat{s} + \hat{t} + \hat{u} = M_C^2 + M_d^2 \tag{A.10}$$

In the case of massless outgoing particles the mandelstam variables satisfy the relation $\hat{s} + \hat{t} + \hat{u} = 0$. In addition to the common cartesian and spherical coordinates, the most commonly used detector coordinate system is in which the polar angle θ is replaced by the pseudo-rapidity η, defined as:

$$\eta = -\ln\left(\tan\frac{\theta}{2}\right) \tag{A.11}$$

the pseudo-rapidity is derived from the rapidity y:

$$y = \frac{1}{2}\ln\left(\frac{E + p_l}{E - p_l}\right) \tag{A.12}$$

in the limit $\frac{m}{E} \to 0$.

The main advantage of using η is that the difference in η between two particles is invariant under *Lorentz boost* along the z-axis. So the distribution as a function of η is invariant for any boost along the z direction. An important application of this property

for particles produced purely by QCD interactions is that distribution for many physics variables as a function of η is flat.

The central region refers to the detector volume with $|\eta| < 1.5$, where a particle travelling will pass through nearly all of the important detector systems. The forward region comprises $5 > |\eta| > 3$, which is very close to the beam axis.

In a real case scenario, the measured η of the outgoing particle is not the same as evaluated in the parton-parton scattering. This is because of the fact that the collision does not always take place at $z = 0$. To measure η in detector, θ is measured with respect to the interaction point. Similarly the momentum transfer in every event is not same and hence the 4-vector are related to the measured η and p_T in detector by the following relationship:

$$p_C = p_T(\cosh(\eta), 1, 0, \sinh(\eta)) \tag{A.13}$$

Appendix B

The Parton Model

In 1967, deep-inelastic electron-nucleon scattering experiments at SLAC [147, 148] showed that the structure functions of the nucleon exhibited approximate "scaling" behavior. The scaling phenomenon can be interpreted if the scattering nucleon contains pointlike particles [149, 150]. This assumption is known as the *Bjorken scaling hypothesis*. In terms of physics, Feynman proposed the parton model [151] which viewed the nucleons as consisting of structureless constituents that are nearly free from each other and each carries a fraction of nucleon's energy. In the later years pointlike constituents were identified as quarks and gluons. These partons cannot exist in isolation and can appear only in colorless bound states known as hadrons. The parton model proved to be quite successful and well established by later developments in perturbative QCD and increasingly sophisticated higher order calculations. The knowledge of QCD and parton model has been used to lay out the fundamental description of the experimental data and to facilitate comparisons between data and recent theoretical calculations. In this model, the initial and final state partons that participate in the hard scattering are assumed to be collinear with the corresponding initial state hadrons and as mentioned in Appendix-A they carry a fraction of energy of the colliding protons. Here the basic assumption is that the collision occurs in two independent stages as shown in Fig B.1. First, two partons,

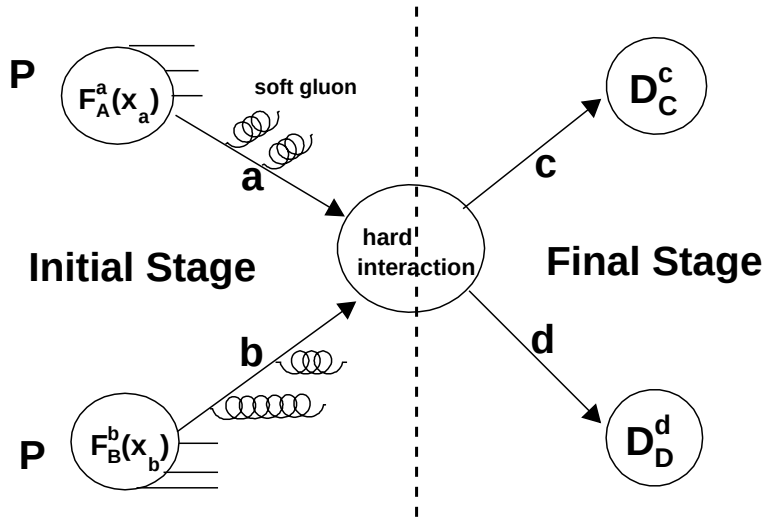

Figure B.1 A schematic view of pp collision. In the initial stage partons 'a' and 'b' carry momentum fraction according to the PDF functions $F_A^a(x_a, Q^2)$ and $F_B^b(x_b, Q^2)$. They radiate soft gluons before collision. The partons c and d, emerging in the final stage after the collision recombine with rest of partons and fragment into hadrons according to the fragmentation functions $D_C^c(z_c)$ and $D_D^d(z_d)$.

one from each hadron, are scattered, the hard collision time being $T = \hbar/\mu$, where μ is the energy transfer during the scattering. The second part comprises of production of outgoing partons and their fragmentation.

The probability that the parton 'a' carries a fraction of momentum of its parent hadron 'A' within the range x_a and $x_a + dx_a$ is given by the probability density function $F_A^a(x_a, Q^2)$, called PDF. At present these PDF functions are fit to a large set of experimental data especially coming from deep inelastic and $p\bar{p}$ collision.

The separation of initial stage (parton distribution function), parton-level hard scattering and final stage(fragmentation) is made possible by the QCD factorization theorem [152, 153]. According to this, the hadronic-level, inclusive production cross section can be written down as convolution of partonic cross section with PDFs and fragmentation functions as shown in equation B.1 (refer also to Fig B.1), where C is the final state particle. One focusses on for inclusive measurements then

$$\sum_{abcd} \int dx_a dx_b dz_c F_A^a(x_a, Q^2) F_B^b(x_b, Q^2) D_C^c(z_c) \frac{\hat{s}}{z_c \pi} \frac{d\sigma}{d\hat{t}}(ab \to cd). \tag{B.1}$$

In this equation, the hadron scattering cross section have been factorized into the parton-level hard scattering part and the distribution functions of partons within the hadrons. If one considers the inclusive cross section for a specific final state particle, one also includes its fragmentation function $D_C^c(z_c)$, the probability for obtaining a particle C from a parton c with momentum fraction between z_c and $z_c + dz_c$. Here Q is the momentum transferred in the hard scattering.

The parton-level hard scattering cross section $\frac{d\sigma}{d\hat{t}}$ is in general an incoherent sum of all participating subprocesses, each of which is convoluted or weighted with the corresponding parton distribution function. The relative merit of direct photon processes is twofold - they generally include fewer contributing processes and the event structure is not obscured by the presence of the extra fragmentation processes.

Bibliography

[1] N. Bohr, Philosophical Magazine, 26, 1 (1913); Philosophical Magazine, 27, 488 (1913); W. Heisenberg, Z. Phys. 77, 1 (1932).

[2] J. Chadwick, Nature, 129, 312 (1932).

[3] P. A. M. Dirac, Proc. R. Soc., London A114, 243 (1927).

[4] E. Fermi, Z. Phys. **88**, 161 (1934).

[5] Y. Yukawa, Proc. Phys. Math. Soc., Japan, 17, 48 (1935).

[6] R.P. Feynman, Phys. Rev. **76**, p.749,769 (1949); "QED: *The Strange Theory of Light and Matter*", Princeton University Press, Princeton, New Jersey, 1985. R. P. Feynman, "*Space-time Approach to Non-Relativistic Quantum Mechanics*", Rev. Mod. Phys. **20**, 367-387 (1948). R.P. Feynman, "*A Relativisitic Cut-Off for Classical Electrodynamics*", Phys. Rev. **74**, 939-946 (1948).

[7] S. Tomonaga, J. R. Oppenheimer, "*On Infine Field Reactions in Quantum Field Theory*", Phys. Rev. **74**, 224-225 (1948).

[8] J. Schwinger, "*On Quantum Electrodynamics and the Magnetic Moment of the Electron*", Phys. Rev. **73**, 416-417 (1948). J. Schwinger, "*Quantum Electrodynamics I. A Covariant Formulation*", Phys. Rev. **74** 1439-1461 (1948).

[9] F. J. Dyson, "*The Radiation Theories of Tomonaga, Schwinger, and Feynman*", Phys. Rev. **75**, 486-502 (1949).

[10] Murray Gell-Mann, Phys Lett 8, 214 (1964); G. Zweig, CERN Report No. 8182/TH401 (1964).

[11] J. J. Aubert *et al.*, Phys. Rev. Lett. **33**, 1404 (1974).

[12] J. E. Augustin *et al.*, Phys. Rev. Lett. **33**, 1406 (1974).

[13] S. W. Herb *et al.*, Phys. Rev. Lett. **39**, 252 (1977).

[14] M. L. Perl *et al.*, Phys. Rev. Lett. **35**, 1489 (1975);

[15] S. Abachi *et al.*, DØ Collaboration, "*Observation of Top Quark*", Phys. Rev. Lett. **74** 2632 (1995).

[16] F. Abe *et al.*, CDF Collaboration,"*Observation of Top Quark Production in $p\bar{p}$ Collisions with the Collider Detector at Fermilab*", Phys. Rev. Lett. **74**, 2626 (1995).

[17] S.L. Glashow, Nucl. Phys. **22**, 579 (1961); A. Salam and J. C. Ward, Phys. Lett. **13**, 168 (1964); S. Weinberg, Phys. Lett. **19**, 1264 (1967).

[18] A. Salam, "*Elementary Particle Theory*", Nobel Symposium, edited by N. Svartholm (Almquist and Wiksells, Stockholm, 1969) p.367.

[19] G. Arnison *et al.*, UA1 Collaboration, "*Experimental observation of isolated large transverse energy electrons with associated missing energy at $\sqrt{s}$ =540 GeV*", Phys. Lett. **B 122**, 103-116(1983). M. Banner *et al.*, UA2 Collaboration, "*Observation of single isolated electron of high transverse momentum in events with missing transverse energy at the CERN $\bar{p}-p$ collider*", Phys. Lett. **B 122**, 476-485(1983).

[20] G. Arnison *et al.*, UA1 Collaboration, "*Experimental observation of lepton pairs of invariant mass around 95 GeV at the CERN SPS collider*", Phys. Rev. Lett. **B 126**, 398-410 (1983). G. Arnison *et al.*, UA1 Collaboration, "*Further evidence for charged intermediate vector bosons at the SPS collider*", Phys. Lett. **B 129**, 273 (1983). P. Bagnaia *et el.*, UA2 Collaboration, "*Evidence for $Z^0 \rightarrow e^+e^-$ at the CERN $\bar{p}-p$ collider*", Phys. Lett. **B 129**, 130-140 (1983).

[21] The LEP Collaboration and LEP Electroweak Working Group, as reported by J. Mnich at the International Europhysics Conference, Tampere, Finland (July 1999).

[22] Chris Quigg, "*Guage Theories of the Strong, Weak, and Electromagnetic Interaction*", Addison-Wesley (1983).

[23] Gordon L.Kane, *Modern Elementary Particles physics*, Addison-Wesley(1993).

[24] Y. Fukuda *et al.*, Super-Kamiokande Collaboration, "*Evidence for Oscillation of Atmospheric Neutrinos*", Phys. Rev. Lett. **81**, 1562-1567 (1998). S. Fukuda *et al.*, Super-Kamiokande Collaboration, "*Solar ^8B and hep Neutrino Measurement from 1258 Days of Super-Kamiokande Data*", Phys. Rev. Lett. **86**, 5651-5655 (2001). S. Fukuda *et al.*, Super-Kamiokande Collaboration, "*Constraints on Neutrino Oscillation Using 1258 Days of Super-Kamiokande Solar Neutrino Data*", Phys. Rev. Lett. **86**, 5656-5660 (2001).

[25] Q. R. Ahmad *et al.*, SNO Collaboration "*Measurement of the Rate of $\nu_e + d \rightarrow p + p + e^-$ Interactions Produced by 8B Solar Neutrinos at the Sudbury Neutrino Observatory*", Phys. Rev. Lett. **87**, 071301 (2001). Q. R. Ahmad *et al.*, SNO Collaboration, "*Direct Evidence for Neutrino Flavor Transformation from Neutral-Current Interactions in the Sudbury Neutrino Observatory*", Phys. Rev. Lett. **89**, 011301 (2002). Q. R. Ahmad *et al.*, SNO Collaboration, "*Measurement of Day and Night*

Neutrino Energy Spectra at SNO and Constraints on Neutrino Mixing Parameters", Phys. Rev. Lett. **89**, 011302 (2002).

[26] T. Araki *et al.*, KamLAND Collaboration, "*Measurement of Neutrino Oscillation with KamLAND: Evidence of Spectral Distortion*", Phys. Rev. Lett. **94** 081801 (2005).

[27] D. G. Michael *et al.*, MINOS Collaboration, "*Observation of Muon Neutrino Disappearance with the MINOS Detectors and the NuMI Neutrino Beam*", Phys. Rev. Lett. **97**, 191801 (2006).

[28] M. Peskin, D. Schroeder, "*An Introduction to Quantum Field Theory*", Westview Pres (1995).

[29] V. Fock, Zeit. f. Physik, **39** (1927) 226.

[30] H. Weyl, Zeit. f. Physik, **56** (1929) 330.

[31] D.J. Gross, F. Wilczek, "*Ultravoilet Behavior of Non-Abelian Gauge Theories*", Phys. Rev. Lett. **30**, 1343-1346 (1973). H. D. Politzer, "*Reliable Perturbative Results for Strong Interactions*", Phys. Rev. Lett. **30**, 1346-1349 (1973). D.J. Gross, F. Wilczek, "*Asymptotically Free Gauge Theories. 1*", Phys. Rev. **D 8**, 3633-3652 (1973). D.J. Gross, F. Wilczek, "*Asymptotically Free Gauge Theories. 2*",Phys. Rev. **D 9**, 980-993 (1974). H. D. Politzer, "*Asymptotically Freedom: An Approach to Strong Interactions*", Phys. Rep. **14**, 123456 (1974) 129-180.

[32] S. Kluth, "*Review of α_s Measurements*", arXive:hep-ex[0609020 v1], Results were presented at ICHEP-06, 2006.

[33] ALEPH, DELPHI, L3, and OPAL Collaborations and LEP Working Group for Higgs Bososn Searches, Phys. Lett. **B 565**, 61 (2003).

[34] The ALEPH, CDF , DØ, DELPHI, L3, OPAL, SLD Collaboration, the LEP Electroweak Working Group, the Tevatron Electroweak Working Group, and the SLD electroweak and heavy flavor groups, arXiv:0811.4682[hep-ex]2008.

[35] B.W.Lee, C. Quigg and H.B. Thacker, Phys. Rev. Lett. **38** (1977) 883.

[36] Gaku Konisi, Hidenori Miyata, Takesi Saito, Kazuyasu Shegemoto, "*A Composite Model of the Higgs Boson*, OU-HET, 13 March, 1976; Michael J. Dugan, Howard Georgi, David B. Kaplan "*Anatomy of a Composite Higgs Model*", Nucl. Phys. **B254**, 299, 1985; Kaustubh Agashe, Roberto Contino, Alex Pomarol, "*The Minimal composite Higgs model*", Nucl. Phys. **B719**, 165-187, 2005.

[37] CDF and DØ Collaboration,"*Combination of CDF and DØ Results on the Mass of the Top Quark*", FERMILAB-TM-2427-E, DØ Note 5899, March 2009.

[38] V.M. Abazov *et al.*, DØ Collaboration,"*Measurement of an isolated photon Cross Section in $p\bar{p}$ collisions at $\sqrt{s}$ = 1.96 TeV*", FERMILAB-PUB-05/523-E, arXiv:0511054v2[hep-ex].

[39] V.M. Abazov *et al.*, DØ Collaboration,"*Measurement of the differential cross section for the production of an isolated photon with associated jet in $p\bar{p}$ collisions at $\sqrt{s}$ = 1.96 TeV*", FERMILAB-PUB-08/081-E, Phys. Lett. **B 666**, 435 (2008).

[40] T. Binoth, J.P. Guillet, E. Pilon, M. Werlen, Eur. Phys. J. **C 16**:311-330 (2000); An overview can be found in DIPHOX, arXiv:hep-ph/9911340.

[41] CMS Technical Design Report-CERN/LHCC 2006-001, ATLAS Technical Design Report-15, CERN/LHCC 99-15(two main studies from CMS - S. Kunori et al., M. Pieri *et al.*).

[42] J. Breitweg *et al.*, ZEUS Collaboration, "*A search for Excited Fermions in e^+p collision at HERA*", Z. Phys. **C 76** (1997) 631.

[43] Bernardo Tome, "*Search for Excited Fermions*", Proceedings of Science **313** (HEP-2005).

[44] C. Adloff *et al.*, H1 Collaboration, "*A Search for Excited Fermions at HERA*", DESY-00-102 (2000).

[45] C. Adloff *et al.*, H1 Collaboration, "*Search for Excited Neutrinos at HERA*", DESY-01-145 (2001).

[46] P. Achard *et al.*, L3 Collaboration, Phys. Lett. **B 568** (2003) 23.

[47] J. Abdallah *et al.*, DELPHI Collaboration, Eur. Phys. J. **C 46** (2006) 277.

[48] F.D. Aaron *et al.*, H1 Collaboration, "*Search for Excited Electrons in ep Collisions at HERA*", arXiv:0805.4530v1[hep-ex], 2008.

[49] G. Köpp, D. Schaile, M. Spira, P.M. Zerwas, Z. Phys. **C 65** (1995) 545.

[50] Reviews by T. Kinoshita and D.R. Yennie, H.U. Martyn, and R. van Dyck Jr. in "*Quantum Electrodynamics*", ed. T. Kinoshita, World Scientific(1990).

[51] F. Abe *et. al.*, CDF Collaboration, Phys. Rev. Lett. **79**(1997) 2192; B. Abbott *et. al.*, DØ Collaboration, Phys. Rev. Lett. **82** (1999) 4769.

[52] F.E. Low, Phys. Rev. Lett. **14**, 238 (1965).

[53] G. Abbiendi *et al.*, OPAL Collaboration, Phys. Lett. **B 549** (2002) 32.

[54] J. Abdallah *et al.*, DELPHI Collaboration, Eur. Phys. J. **C 37** 2004, 405.

[55] I.A. Bertram, DØ Collaboration, Report No. Fermilab-Conf-96/389-E, (1996).

[56] F. Abe *et al.*, CDF Collaboration, Phys. Rev. Lett. **72**, 3004 (1994).

[57] F. Abe *et al.*, CDF Collaboration, Phys. Rev. **D 74**, 3538 (1995).

[58] T. Affolder *et el.*, Phys. Rev. Lett. **87**, 231803 (2001).

[59] B. Abbott *et el.*, Phys. Rev. **D 62**, 031101 (2000).

[60] DØ Collaboration, "*First Measurement of Dijet Angular Distributions in the TeV Regime and Searches for Quark Compositeness and Extra Dimensions*", DØ Note 5733-CONF.

[61] CDF Collaboration, "*Search for Quark Substructure in the angular distribution of dijets produced in $p\bar{p}$ collisions at $\sqrt{s} = 1.9$ TeV*", CDF/ANAL/JET/PUB/9609.

[62] Marco Cardaci *et al.*, *"CMS Search Plans and Sensitivity to New Physics using Dijet"*, CMS NOTE-2008/019.

[63] Samir Ferrag on behalf of ATLAS and CMS Collaboration, "*Search for Compositeness at LHC*", Journal of Physics: Conference Series 110 (2008) 072010.

[64] Dimitri Bourilkov, *"Compositeness Search with Dimuons in CMS"*, CMS NOTE-2006/085.

[65] ATLAS Collaboration, *"Detector and Physics Performance Technical Design Report: Volume-II"*, ATLAS TDR-15, CERN/LHCC 99-15.

[66] Ben Lillie, Jing Shu and Tim M.P. Tait, "*Top compositeness at the Tevatron and LHC*", JHEP04 (2008) 087.

[67] T.G.Rizzo, Phys. Rev. **D 52**, 1064 (1995).

[68] P. Hasenfratz and J. Nager, Z. Phys. **C 37**, 477 (1988).

[69] Leon M. Lederman and Dick Teresi, "*The God Particle: If the Universe Is the Answer, What is the Question?*", Dell Publishing, 1993.

[70] Souvik Das for the CMS Collaboration,"*The Status and performance of the CMS pixel detector* ", CMS Conference Report-2009/058.

[71] CMS Collaboration, "*CMS: The Tracker Project Technical Design Report*", CERN/LHCC 98-6.

[72] CMS Collaboration, "*Addendum to the CMS Tracker TDR*", CERN/LHCC 2000-16.

[73] CMS Collaboration, "*CMS: Physics Technical Design Report Volume I, Detector Performance and Software*", CERN/LHCC 2006-001.

[74] S. Beauceron, P. Bloch, "*Study of ECAL Endcap Energy Resolution using 2007 Test Beam Data*", CMS DN 2009/002.

[75] CMS Collaboration, "*CMS ECAL Technical Design Report*", CERN/LHCC 97-33.

[76] CMS Collaboration, "*CMS HCAL Technical Design Report*", CERN/LHCC 97-31.

[77] G. Baiatian *et al.*, "*Design, Performance, and Calibration of CMS Hadron-Barrel Calorimeter Wedges"*, CMS HCAL Collaboration, CMS Note 2006/138.

[78] G. Baiatian *et al.*, "*Design, Performance, and Calibration of CMS Forward Calorimeter Wedges "*, CMS Note 2006/044.

[79] S. V. Chenkov, "*Jet algorithms: A mini review*", hep-ph/0211298.

[80] G.P. Salam and G. Soyez, "*A practical seedless infrared-safe cone jet algorithm*", JHEP05 (2007) 086.

[81] G.C. Blazey *et. al.*, "*Run II jet physics: Proceedings of the Run II QCD and Weak Boson Physics Workshop*", hep-ex:005012(2000).

[82] Jesus Puerta Pelayo on behalf of CMS Collaboration, "*CMS Muon System Performance*, CMS Conference Report-2009/152.

[83] CMS Collaboration, "*CMS: The Trigger and Data Acquisition Project, Volume- I: The Level-1 Trigger Technical Design Report"*, CERN/LHCC 2000-38.

[84] CMS Collaboration, "*CMS: The Muon Project Technical Design Report"*, CERN/LHCC 97-32.

[85] CMS Collaboration, "*CMS: The Trigger and Data Acquisition Project, Volume-II: Data Acquisition and High-Level Trigger Technical Design Report"*, CERN/LHCC 2002-26.

[86] T. Virdee *et al.*, "*CMS High Level Trigger*", CERN-LHCC-2007-021, Geneva, 2007.

[87] $https://twiki.cern.ch/twiki/bin/view/CMS/TriggerMenuDescription1E31Devel.$

[88] T. Sjostrand *et al.*, "*High-energy-physics event generation with PYTHIA6.1*", Computer Physics Communications **135**, 238 (2001) and PYTHIA home page, $http://www.thep.lu.se/torbjorn/pythiaaux/present.html$. J. P. Guillaud, PYTHIA miniguide, CMS Note 2000/070.

[89] HERWIG manual, $http://hepwww.rl.ac.uk/theory/seymour/herwig/hw65manual.html$.

[90] ISAJET manual, $http://www.phy.bnl.gov/isajet/isajet.ps$.

[91] M.L. Mangano *et. al.*,"*ALPGEN, a generator for hard multiparton processes in hadronic collisions*", Journal of High Energy Phys. **307**, 001 (2003).

[92] MadGraph Manual, *"MadEvent: a multipurpose event generator powered by Madgraph" http : //cp3wks05.fynu.ucl.ac.be/Manual/Manual − March − 2007.pdf.*

[93] *http : //cmsdoc.cern.ch/PRS/gnetools/www/geners/collection/colleciton.html.*

[94] *http : //wwwlapp.in2p3.fr/lapth/PHOXFAMILY/main.html.*

[95] *http : //cmsdoc.cern.ch/cmsoo/projects/CMKIN/.*

[96] Lynn Garren, stdHep 5.01, Monte Carlo Standardization at FNAL, PM0092, June 10, 2002.

[97] J. Alwall *et al.*, "*A Standard Format for Les Houches Event File*", arXiv:0609017v1[hep-ph] 2006.

[98] *http : //projects.hepforge.org/lhapdf/*

[99] M. Pieri *et al.*, CMS Note-2006/112.

[100] CMS Collaboration, Report No. CERN/LHCC 2006-001, 2006.

[101] FAMOS ("Fast Monte Carlo Simulation"),
http : //cmsdoc.cern.ch/cmsoo/projects/FAMOS.

[102] CMS TriDAS Project Data Acquisition and High-Level Trigger Technical Design Report CERN/LHCC 2002-26 CMS TDR 6.2.

[103] S. Catani, Y.L. Dokshitzer, M. H. Seymour, B. R. Webber, "*Longitudinally Invariant K_T" Clustering Algorithms for Hadron Hadron Collisions*", Nucl. Phys. **B 406** (1993) 187.

[104] J.M. Butterworth, J. P. Couchman, B. E. Cox, and B. M. Waugh, "*KtJet: A C++ implementation of the K(T) clustering algorithm*", Comput. Phys. Commun. **153** (2003) 35 [hep-ph/0210022].

[105] S.D. Ellis and D.E. Soper, "*Successive combination jet algorithm for hadron collisions*", Phys. Rev. **D 48** (1993) 3160 [hep-ph/9305266].

[106] G. Arnison *et al.*, "*Hadronic Jet Production at the CERN Proton-Antiproton Collider*", Phys. Lett. **132** (1983) 214.

[107] H. L. Lai *et al.,* CTEQ Collaboration, Eur. Phys. J. **C 12**, 375 (2000).

[108] P. Schieferdcker *et al.*, "*Performance of Jet Algorithms in CMS*", CMS Analysis Note-2008/001.

[109] ATLAS Collaboration, "*Detector and Physics Performance Technical Design Report*", CERN/LHCC 99-14.

[110] R. Barlow, "*Statistics: a guide to the use of statistical methods in the physical sciences*", John Wiley & Sons ltd., West Sussex (1989).

[111] P. Gupta *et al.*, Eur. Phys. J. **C 53**, 49-58 (2008).

[112] K. O. Mikaelian, M. A. Samuel and D. Sahdev, "*The Magnetic Moment Of Weak Bosons Produced In P P And P Anti-P Collisions*", Phys. Rev. Lett. **43**, 746 (1979).

[113] M.A. Samuel and T. Abraha, [arXiv:hep-ph/970633v1], U. Baur, S. Errede and G. Landsberg, Phys. Rev. **D 50** (1994) 1917, V.M. Abazov *et al.*, "*First Study of the radiation-amplitude zero in $W\gamma$ production and limit on $WW\gamma$ couplings at $\sqrt{s}$ =1.96 TeV*", [arXiv:hep-ex/0803.0030v2].

[114] L. Fano (On behalf of CMS collaboration), CMS Conference Report-2006/083.

[115] F. James, MINUIT - Function Minimization and Error Analysis, CERN Program Library Long Writeup **D 506**, 1998.

[116] *http : //root.cern.ch/drupal/content/users − guide.*

[117] E. L. Berger, X. f. Guo and J. w. Qiu, "*Isolated Prompt Photon Production in Hadronic Final States of e + e − Annihilation"*,Phys. Rev. **D 54**, 5470 (1996).

[118] S. Catani, M. Fontannaz and E. Pilon, "*Factorization and soft-gluon divergences in isolated-photon cross sections"*, Phys. Rev. **D 58**, 094025 (1998).

[119] N. L. Johnson, S. Kotz, Distributions Statistics - Discrete Distributions, Wiley, New York, 1969.

[120] S. I. Bityukov and N. V. Krasnikov, "*The Search for New Physics by the Measurement of the Four-jet Cross Section at the LHC and Tevatron*", Modern Physics Letter A **12** (1997) 2011, also hep-ph/9705338.

[121] S. Abdullin, "*Search for SUSY at LHC: Discovery and Inclusive Studies*", Presented at International Europhysics Conference on High Physics, Jerusalem, Israel, August 19-26, 1997, CMS Conference Report 97/019 November 1997.

[122] S.I. Bityukov and N.V.Krasnikov, "*The Search for Sleptons and Flavor Leptons Number Violation at LHC (CMS)*", Preprint IFVE 97-67, Protvino, 1997, arXiv:9712358[hep-ph].

[123] H. Baer, M. Bisset, C. Kao and X. Tata, "*Observability of $\gamma\gamma$ decays of Higgs bosons from supersymmetry at hadron supercolliders*", Phys. Rev. **D 46**, 1992, p.1067.

[124] Berger, J.O. (1999) "*Statistical Decision Theory and Bayesian Analysis*". Second Edition. Springer Verglas, New York. ISBN 0-387-96098-8 and also ISBN 3-540-96098-8.

[125] Jerzy Neyman, Egon Pearson,"*On the Problem of the Most Efficient Tests of Statistical Hypotheses*"- Philosophical Transactions of the Royal Society of London - Series A - Vol 231 (1933) pp. 289-337.

[126] ALEPH Collaboration, DELPHI Collaboration, L3 Collaboration, OPAL Collaboration and The LEP Working Group for Higgs Boson Searches, Phys. Lett. **B 565** (2003) 61.

[127] Maurice G. Kendall, Alan Stuart, The Advanced Theory of Statistics, Vol. 2, "*Inference and Relationships*", Hafner Publishing Company, New York, 1961.

[128] A. L. Read, "*Presentation of Search Results: The CL_s Technique*", J. Phys.G: Nucl. Part. Phys. **28**, 2693-2704 (2002).

[129] O. Cakir, R. Mehdiyev,"*Excited quark production at the CERN LHC*", Phys. Rev. **D 60**, 034004 (1999).

[130] G. Abbiendi *et al.*, OPAL Collaboration, Eur. Phys. J. **C 26**, 479 (2003).

[131] J. Pumplin, D. R. Stump, J. Huston, H. L. Lai, P. Nadolsky and W. K. Tung, JHEP **0207** (2002) 012 [arXiv:hep-ph/0201195].

[132] A.D. Martin, R.G. Roberts, W.J. Stirling and R.S. Thorne, Eur. Phys. J. **C 23** (2002) 73.

[133] P. Bartialini, R. Cheirici and A. De Roeck, "*Guidelines for the Estimation of Theoretical Uncertainties at the LHC*", CMS Note -2005/115, (2005).

[134] P. Aurenche, M. Fontannaz, J. P. Guillet, E. Pilon, and M. Werlen, Phys. Rev. **D 73**, 094007 (2006).

[135] V. M. Abazov *et al.*, DØ Collaboration, arXiv:0804.1107v2[hep-ex] 2008.

[136] S. Catani, M. Fontannaz, J. P. Guillet and E. Pilon, JHEP05 (2002) 0820.

[137] Z. Bern, L. Dixon, C. Schmidt, Phys. Rev. **D 66**, 074018 (2002).

[138] CMS Collaboration, "*CMS Physics Technical Design Report Vol-II*", Jour. of Phys. G **34** (2007) 995-1580.

[139] S. Abdullin *et al.*, CMS Note-2006/122.

[140] Thesis by Efe Yazgan,"*Search for a standard model Higgs Boson in CMS via vector Boson fusion in the $H \rightarrow WW \rightarrow l\nu l\nu$ channel and optimization of energy reconstruction in CMS using test beam data.*" June 2007, CERN Report No. CERN-THESIS 2007-052, 2007.

[141] T. Binoth *et al.*, QCD/SM Working Group, Les Houches, 2001.

[142] Z. Bern, L. Dixon, C. Schmidt, Phys. Rev. **D 66**, 074018 (2002).

[143] T. Binoth, J. Ph. Guillet, E. Pilon and M. Werlen, Eur. Phys. J. direct **C4**:7 (2002) [arXiv:hep-ph/0203064v2].

[144] D. Choudhury, S. Majhi and V. Ravindran, J. High Energy Phys. **01** (2006) 027.

[145] D. Acosta *et al.*, CDF Collaboration, Phys. Rev. Lett. **95**, 022003 (2005).

[146] S. Mandelstam, "*Determination of the Pion-Nucleon Scattering Amplitude from Dispersion Relations and Unitarity*", Phys. Rev. **112** (1958) 1344.

[147] E. D. Bloom, D. H. Coward, H. DeStaebler, J. Drees, G. Miller, L. W. Mo, and R. E. Taylor, "*High-Energy Inelastic e-p Scattering at 6 and 10*", Phys. Rev. Lett. **23**, 930 (1969).

[148] J. I. Friedman and H. W. Kendall, *Deep Inelastic Electron Scattering*, Ann. Rev. Nucl. Sci. **22**, 203 (1972).

[149] J. D. Bjorken, Phys. Rep. **179**, 1547 (1969).

[150] R. P. Feynman, Phys. Rev. Lett. **23**, 1415 (1969).

[151] R. P. Feynman, Photon-Hadron Interactions, Benjamin, 1972.

[152] CTEQ Collaboration, *Handbook of Perturbative QCD*, Fermilab–Pub–93/094, 1993.

[153] J.C. Collins, D.E. Soper, *The Theorems of Perturabative QCD*, Ann. Rev. Nucl. Part. Sci. **37**, 383 (1983).